UNIVERSITY OF OSLO
Department of Physics

Identification and tracking of extreme electron densities by EISCAT Svalbard radar and SuperDARN

Master thesis

Vigdis Lonar Barth

May 29, 2009

UNIS
The University Centre in Svalbard

UNIVERSITAS OSLOENSIS
MDCCCXI

Abstract

The aim of this master thesis is to track the source of extreme electron densities observed in the polar cap above Svalbard. The data base is the long duration runs performed by EISCAT Svalbard Radar (ESR) in February 2001 and October 2002. The October data consists of 27 days with 24 hours continuous observations at a stable activity level, while the data from February consists of 20 days. From these two data sets, the ionospheric activity is analyzed, and the intake of high plasma density material from the subauroral ionosphere to the polar cap is studied.

Extreme electron densities larger than $10^{12}m^{-3}$ and periods of extreme density values (onset time and duration) are listed. The extreme densities are found to occur in a more or less regular pattern around magnetic noon. Their duration is thus more variable, ranging from less than two minutes to over 120 minutes where the brief events are the most frequent. Solar wind data from the ACE (Advanced Composition Explorer) satellite, and SuperDARN (Super Dual Auroral Radar Network) convection maps are used to obtain a connection between the interplanetary magnetic field (IMF) and the occurrence of the extreme densities. From ACE we get information about the IMF and the speed of the solar wind. The extreme densities show no direct dependence on the IMF, but the movement across the polar cap is dependant on the direction of the IMF B_y component. The SuperDARN convection maps provide us with information about the coverage of radar data in the polar cap. From these convection data, we have developed a tracing method with the intention to track the extreme density events back to their potential origin. The result show that the extreme densities are produced by solar EUV ionization, and that they enter the polar cap from a sunlit area at low latitudes. The path of the enhanced densities seems to follow the convection stream lines across the polar cap. The motion is stepwise, which indicates pulsed flow possibly due to transient magnetic reconnection going on at the magnetopause. The flow is pulsed both at subauroral latitudes, in the cusp inflow region, and in the polar cap.

Acknowledgment

First of all, I would like to thank my two competent supervisors Jøran Moen and Kjellmar Oksavik for their excellent guidance during these two years. This thesis would not have been the same without their valuable help and constructive feedback. I really appreciate that they have given me an exciting, challenging and informative project to work with. I would also like to thank them for giving me the amazing opportunity to study at UNIS (the University Centre in Svalbard). During this stay, I have been given the possibility to participate in exciting field work at the EISCAT Svalbard radar (ESR) and the Kjell Henriksen Observatory (KHO), which has provided me with motivation and a great interest for my thesis work. I also would like to give a thanks to my co-supervisor Yvonne Rinne for helping me out on my Matlab problems and for answering several questions on the way.
The people who have provided me with the data for this thesis deserve a thanks too. The EISCAT Scientific Association for providing med with two months of continuous data to work with. EISCAT is an international association supported by research organisations in China (CRIRP), Finland (SA), France (CNRS, till end 2006), Germany (DFG), Japan (NIPR and STEL), Norway (NFR), Sweden (VR), and the United Kingdom (STFC). Thanks to the ACE Science Center (ASC) and the ACE MAG and SWEPAM instrument teams for providing solar wind data from the ACE Spacecraft. Thanks also to the John Hopkins University (JHUAPL) for SuperDARN plots and Kjellmar Oksavik for the convection data which he generated with the help from raw SuperDARN data provided by Mike Ruohoniemi at Virginia Polytechnic Institute and State University (Virginia Tech). Thanks to Eleri Pryse for giving me the tomography maps needed, and to Anja Strømme for checking the availability of data from the Sondrestrom radar in Greenland.
I would also like to thank Espen Trondsen, Bjørn Lybekk and the IT support at UNIS for helping me out with my computer problems.
Thanks to all my good friends. When I needed some time off from my study, they were always there for me. My fellow students, both at Svalbard and UiO deserves a huge thanks for all the nice coffee, lunch and dinner breaks. A special thanks to every one that participated in the "08:40 coffee meetings" at UNIS, which made my mornings perfect. Last, but not least I would like to give a huge thanks to my brother Audun, my mum Torgunn and my dad Sverre. Thank you for giving me the motivation needed, the go-ahead spirit on the way, encouragement and economic support when I needed it.

Vigdis Lonar Barth
Oslo, May 2009

Contents

Chapter 1

Introduction

The solar wind interacts with the Earth's magnetosphere and gives rise to space weather phenomena in the Earth's atmosphere. These space weather phenomena give rise to disturbances such as inaccuracy in the received signal or in the worst case, a loss of signal in electronic equipment, radio communications and navigation systems. The communication and navigation systems using radio wave communication in the polar regions can therefore be affected by plasma density enhancements under extreme conditions. This can lead to navigation error which again can lead to severe oil spills, accidents and loss of life in the northern areas. Severe outcome for the man made technology can also occur. In particular, the Global Positioning System (GPS) is affected by this phenomena since it uses constellations of earth-orbiting satellites. In principle, the GPS uses known positions of satellites and their distances from a receiver to determine the location of the receiver. To be able to avoid these incidents, the community needs to know when these space weather phenomena occur [Behnke et al., 1995; Baker, 1998, 2005]. Figure (1.1) shows modern technology that can be affected by space weather, e.g. satellites, astronauts, aircrafts, communication and navigation systems, power lines and pipelines. Radio links are not suffering directly from high plasma densities, but rather from electron density gradients in the ionosphere [Buchau et al., 1985]. The main concern is therefore when radio wave signals hit the contour of a patch or the boundary region of high electron density.
Electron density enhancements have been observed in the polar cap for decades by instruments like ionosondes e.g. [Buchau et al., 1983; Weber et al., 1984], radars e.g. [Lockwood and Carlson Jr., 1992; Valladares et al., 1994, 1996], and ionospheric tomography e.g. [Walker et al., 1999]. Some of these electron density enhancements occur as isolated islands called patches, but not all density enhancements are patches. Some density enhancements are referred to as extreme electron densities, and they are defined as $n_e \geq 10^{12} m^{-3}$ [Moen et al., 2008]. The high density solar EUV plasma and the polar cap patches $E \times B$ drift in an anti-sunward direction with the convection streamlines across the polar cap, and they are thought to originate from a sunlit area at lower latitudes [Weber et al., 1984; Foster and Doupnik, 1984; Buchau et al., 1985].

Svalbard is an ideal place to study the high-latitude ionosphere, due to Svalbards location inside the daytime auroral oval, and thus the cusp/formation

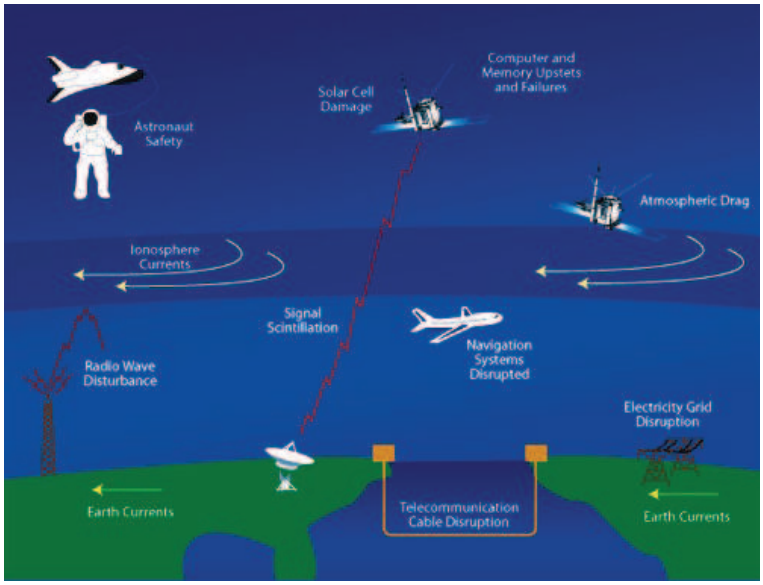

Figure 1.1: The most important aspect of studying extreme high density plasma is associated with HF radio communication links in polar regions. The figure shows modern technology that can be affected by space weather. Figure from `http://sdo.gsfc.nasa.gov/mission/spaceweather.php`.

region, and because of the extensive research infrastructure in the area. The EISCAT Scientific Association is an international organization which operates radars in northern Scandinavia, in addition to the EISCAT Svalbard Radar (ESR) located close to Longyearbyen. The ESR is an incoherent scatter radar, which can monitor the upper atmosphere using the incoherent scatter technique. The ESR consists of one 42m antenna which is fixed along the magnetic field, and one fully steerable 32m antenna. With long duration experiments the time-dependent ionosphere can be studied continuously and trends and characteristics of the upper atmosphere can be identified. Discrete F-region electron density enhancements greater than $10^{12}m^{-3}$ have been observed by the ESR during two long duration campaigns in February 2001 and October 2002. This is an excellent data base for studying extreme densities, since there was a maximum in solar activity in 2001. SuperDARN is a network of coherent high frequency (HF) radars that is distributed all over the northern- and southern hemispheres. Based on raw SuperDARN data, the electron density enhancements can be traced backwards in time over a period of a few hours, and the location of the origin can be determined. The plasma enhancements can also be followed forward in time. This thesis is the first attempt to identify the source of the extreme densities seen with the ESR. Due to the limited time available for a master thesis project, attention is focused on dayside data only.

The intention of this thesis is summarized below:

1. Check whether there is an IMF control on the intake of high density plasma patch material.

2. Search for other factors that control the intake of extreme plasma densities.

3. Locate the possible source region of extreme densities by tracing the observed events backward in time.

This thesis thus focus on detecting extreme densities in the polar cap and tracing them backward in time to find their possible origin. Various factors of intake of extreme plasma densities will also be investigated, e.g. is there an IMF control of the intake of high density plasma patch material? Other relevant issues investigated are: Can we be able to predict and thus forecast under which conditions the extreme densities will occur? What is the occurrence rate of the extreme density events and what is their typical duration? What is the path of enhanced electron densities across the polar cap? At which location is the densities produced?

An introduction to relevant space physics theory is given in chapter 2. Chapter 3 presents the various instruments and datasets used. Chapter 4 gives an explanation of the technique behind the method used. Observations and results are to be found in chapter 5, followed by a discussion in chapter 6. A brief summary and conclusion are found in chapter 7, together with suggestions and ideas for future work.

Chapter 2

Background

An introduction to relevant space physics terminology used in this thesis is given below, starting with a description of the Sun and its solar cycle. The solar wind, the interplanetary magnetic field and the Earth's magnetic field is thereafter described. Next follows a description of the magnetosphere and the boundary layers, the ionosphere, and the magnetic reconnection process. An introduction to polar cap patches, and the tongue of ionization is further described, before the convection in the high-latitude ionosphere is explained in the end of the chapter. For further introduction to space physics, see for instance the book "Introduction to space physics" by Kivelson and Russel [1995] and papers cited in this chapter.

2.1 The Sun and the solar cycle

The sun is centered in the middle of our solar system. It has a mass of about 2×10^{30} kg and a radius of 696 000 km. The Sun is composed of hydrogen (90%), helium (10%) and a small amount of carbon (C), nitrogen (N) and oxygen (O) [Priest, 1995]. Due to the high temperature, the matter is in the form of gas and plasma, and therefore the Sun does not rotate like a rigid body. At the Sun's surface, the period of rotation varies with latitude from 25 days at the equator to about 35 days at the poles.

Figure 2.1 shows the different layers and the exterior of the Sun. The innermost layer, the Core, is where all of the Sun's energy is produced. The energy is released when hydrogen is converted into helium by nuclear fusion. Through fusion, the Sun produces electromagnetic radiation. All of this created energy must travel through the different layers to reach the solar photosphere, where the energy is released into space. A small region known as the chromosphere lies above the photosphere, and this layer is dominated by an electromagnetic spectrum of emission and absorption lines. The corona extends millions of kilometers into space, and is located above the chromosphere. This region creates the solar wind, which is described in the next section. The Sun has a magnetic field which can be very strong and vary over time from place to place. Due to the difference in rotation, the magnetic field lines become twisted together over time [Chapman and Bartels, 1940].

In 1610, Galileo Galilei made the first European observations of Sunspots. A

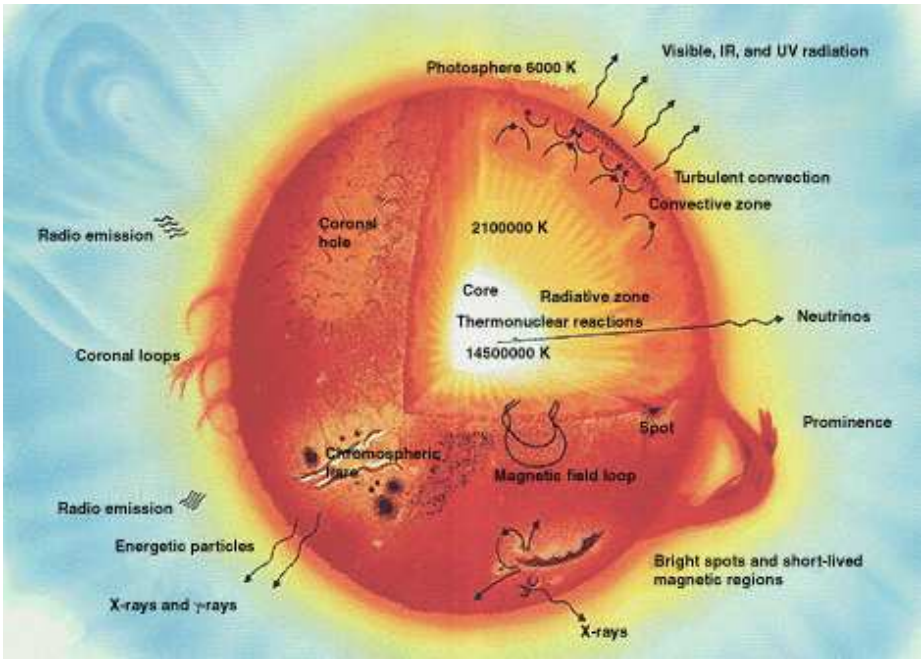

Figure 2.1: The layers of the Sun; the Core, radiative zone, convective zone, photosphere, chromosphere and corona. Figure from `http://imagine.gsfc.nasa.gov/docs/science/know_l2/sun_parts.html`.

sunspot is a region with an intense magnetic activity and they appear as dark areas on the Sun because they have lower temperature than their surroundings. Inside sunspots, which can be tens of thousands of kilometers wide, the magnetic field can be several thousand times the strength of the Earths magnetic field. Sunspots occur where the magnetic field lines emerge from the inside of the Sun to form expanding loops above its surface. The number of sunspots visible on the Sun is not constant, but varies over an 11-year cycle known as the sunspot cycle. When the cycle reaches solar minimum, few or none sunspots are visible. The opposite situation takes place for solar maximum, where there is high sunspot activity. The solar cycle consist of two sunspot cycles, both with 11 years duration. Figure (2.2) shows how the sunspot cycle varies from the year 1750 until present.
The sunspots can occur alone, but they usually occur in groups. A typical group consists of two main spots, and about 10 spots in total. There are two main spots in a group and they have opposite polarity, where one is the magnetic south pole and the other is the magnetic north pole. The polarity shifts when a new sunspot cycle starts. For further reading about other solar features like solar flares, coronal holes, prominences and helmet streamers, see Priest [1995].

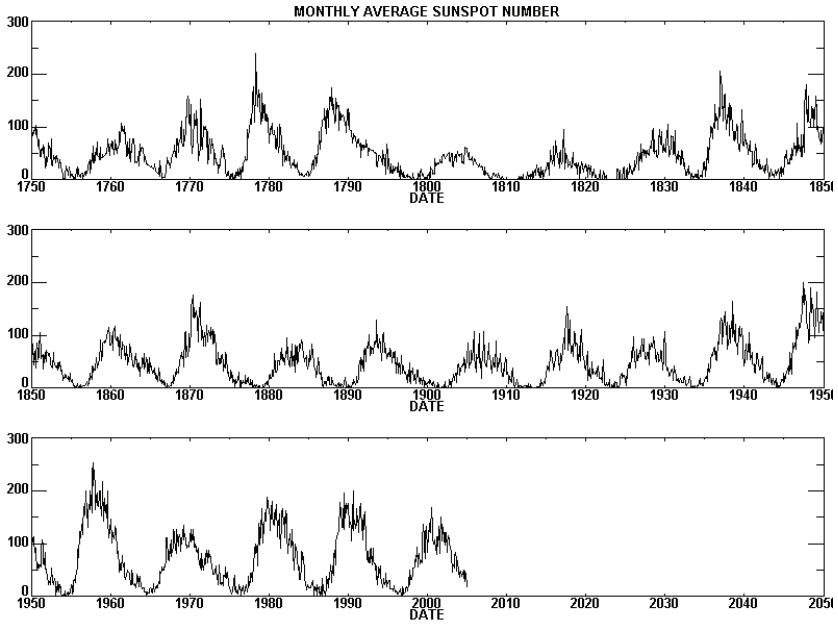

Figure 2.2: The yearly variations in the number of sunspots from 1750 until present. Figure from `http://abyss.uoregon.edu/~js/ast121/lectures/lec23.html`.

2.2 The solar wind and the interplanetary magnetic field

In addition to radiation in the electromagnetic spectrum, the Sun also emits a low density stream of highly conducting particles known as the solar wind. The solar wind originates in the solar corona where a huge difference in the gas pressure between the corona, and interstellar space makes the plasma travel outward, even though there is a restraining influence of solar gravity [Axford et al., 1963]. From the corona, the solar wind propagates throughout the solar system at about 420 $\frac{km}{s}$, see figure (2.3), but this is a rather variable number since both density, velocity, temperature and magnetic field properties vary throughout the solar cycle. Normally the solar wind velocity varies between 250 and 800 km/s and the density varies between 10^6 and $2 \cdot 10^7$ m^{-3} [Ness et al., 1971; Lepping et al., 2003]. The magnetic field strength varies between 1nT and 15nT and is on average 5.5nT [Lepping et al., 2003]. The solar wind consists mostly of ionized hydrogen (or of protons and electrons in nearly equal numbers) and a small admixture of ionized helium and yet fewer ions of heavier elements [Hundhausen, 1995].

The Interplanetary Magnetic Field (IMF) is a weak magnetic field embedded in this plasma. It is carried by the magnetic field lines coming from the Sun, and dragged out by the solar wind. The solar wind extends over a huge distance and therefore has important effects on the interaction with the Earth e.g [Axford et al., 1963]. The high electrical conductivity of the plasma prevents

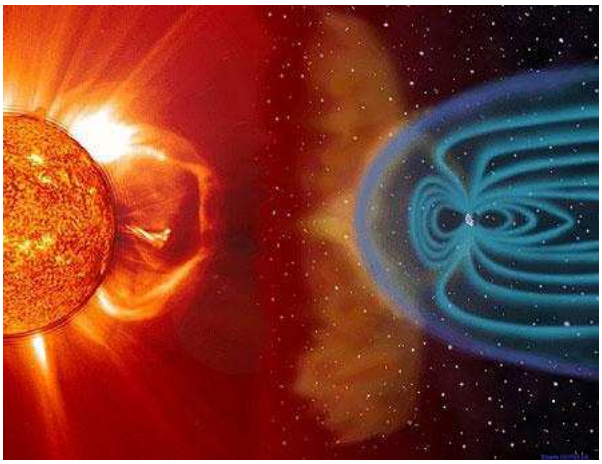

Figure 2.3: The solar wind coming from the sun to the left, traveling towards the earth to the right. Figure from `http://www.sunearthplan.net/3/interplanetary-space`.

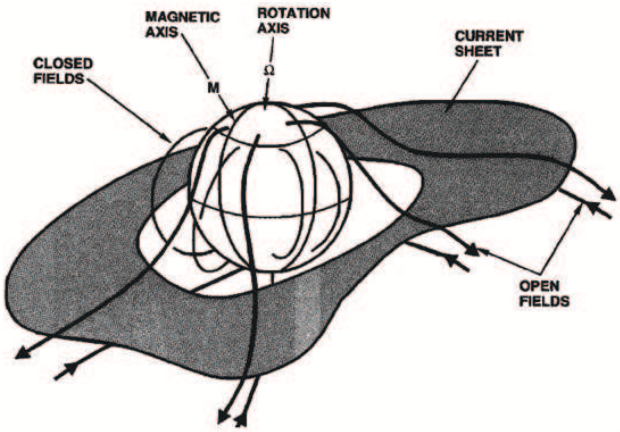

Figure 2.4: The "ballerina skirt" model which separates the Sun's extended field lines. The Sun is the sphere in the middle of the figure, north is in the top and south is in the bottom of the figure. The shaded area is the current sheet which separates fields from the north and south solar magnetic poles which are open, that is only one end attached to the Sun. The magnetic axis of the solar fields are labeled M, and it is shown tilted with respect to the Sun's rotation axis labeled Ω. The closed field lines have both their ends sticked to the Sun, and are shown in the figure at mid-latitudes to low-latitudes. These field lines are inside the current sheet. The field lines above and below the current sheet make the spiral structure of the solar wind. Figure from Smith [2001].

motion across the magnetic field lines, and these lines are therefore said to be "frozen into" the solar wind and forces the plasma to act collectively as a magnetic hydrodynamic fluid. In other words, as long as the "frozen in" condition is valid, the plasma will stick to the magnetic field lines, read more about this in section (2.4.2),

The region that separates the fields of different polarities in the interplanetary medium is called the heliospheric current sheet (HCS). This is due to the fact that in any particular region, the interplanetary magnetic field will map either to the upper solar-hemisphere or the lower solar-hemisphere which have a different field polarity [Lepping et al., 2003]. Figure (2.4) shows the "ballerina skirt" model of the heliospheric current sheet (HCS). Here the inward field is from the lower hemisphere and the outward field is from the upper hemisphere, but this polarity scheme changes according to the solar cycle. Due to the offset between the Sun's rotation axis and its magnetic axis, the current sheet looks like a ballerina skirt.

The need for various coordinate systems is due to the fact that different physical processes are better understood and easier to calculate in various reference systems. Magnetic field, electric field, electric currents, position, velocity, etc are vectors which usually are represented numerically by x, y and z components depending on the coordinate system used [Russell, 1971]. The solar wind data used in this thesis is given in Geocentric Solar Magnetosheric System coordinates (GSM). Here, the x-axis points from the Earth to the Sun, the y-axis is defined to be perpendicular to the earth's magnetic dipole, directed towards dusk (east) so that the x-z plane contains the dipole axis. Finally, the positive z-axis is chosen to be in the same sense as the northern magnetic pole [Russell, 1971; Hapgood, 1992]. For further reading, see Russell [2001].

2.3 The Earth's magnetic field

The Earth is protected from the solar wind by its magnetic field. Close to the earth's surface, the magnetic field is approximately a magnetic dipole field, with one pole near the geographic north pole and one near the geographic south pole, see figure (2.3) and (2.5). The Earth's magnetic north pole is in the southern hemisphere. The dipole axis is tilted nearly 11.5° away from the earth's rotation axis [Lepping et al., 2003], thus the geographic and magnetic poles are not at the same location. In the northern hemisphere the geomagnetic pole is located at $79.74°N$ and $71.78°W$, while the magnetic pole is located at $83.21°N$ and $118.32°W$ and moves about 40km a year (values from 2005). A decrease in the field strength of the Earth's magnetic field has also been observed over the past 100 years. At the moment, the field strength at the magnetic poles is approximately 60 000 nT. The motion of molten metals, like iron and nickel in the Earth's core, generates our planet's magnetic field. This movement generates currents and magnetic fields that produce the Earth's magnetism. Since these are not steady flows, the magnetic field changes over time and the poles change their position. Studies of the Earth's magnetic field show that the poles have reversed their orientation at irregular intervals of hundreds of thousands of years, with north becoming south and vice versa [Glatzmaier and Roberts, 1995].

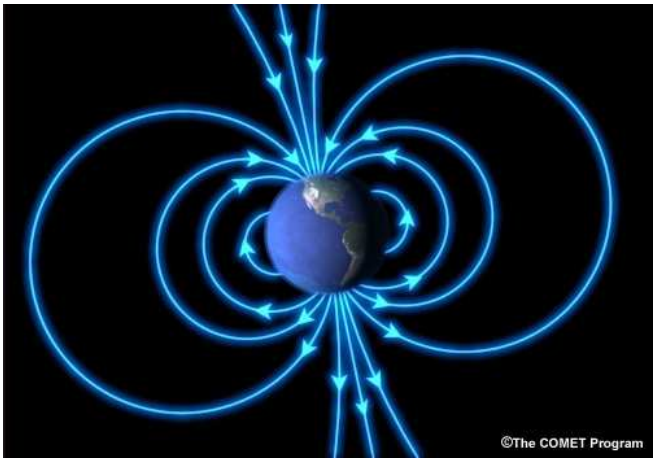

Figure 2.5: Near the Earth, the magnetic field is approximately a magnetic dipole field. Figure from `http://www.meted.ucar.edu/hao/aurora/txt/x_m_1_0.php`.

Further away from the Earth, the solar wind strongly influences the magnetic field, and it shapes the terrestrial field into the magnetosphere. The solar wind changes from supersonic to subsonic as it passes through the bowshock and therefore compresses the magnetic field on the dayside while dragging the field out into a comet-like tail on the earth's night side, as discussed in the next section.

The magnetic field distinguishes between regions of open and closed magnetic field lines. The open magnetic field lines are connected to the Earth at one side only, and coupled to the interplanetary magnetic field on the other side. The closed magnetic field lines are connected to the Earth in both ends, see figure (2.5). The polar cap is defined as the region of the Earth with open magnetic field lines, and the auroral oval is located near the polar cap boundary (the open-closed magnetic boundary) see figure (2.11). The equatorward region of the auroral oval consists of closed magnetic field lines.

2.4 Plasma behavior

There exists two equivalent approaches for describing the behavior of space plasma, either considering the plasma as a collection of single charged particles or seeing the collection of particles as a single fluid, called magneto hydrodynamics (MHD). Since plasma consists of electrically conducting particles, the plasma will respond to both magnetic and electric fields which are present.

2.4.1 Single particle motion

Given an electric field $\vec{E}$ and a magnetic field $\vec{B}$ which both act on a particle with charge q and velocity v, the particle will experience a force known as the

Lorentz-force in the equation of motion

$$F_L = m\frac{\partial \vec{v}}{\partial t} = q(\vec{E} + \vec{v} \times \vec{B}) \tag{2.1}$$

The particles behave different whether there is a magnetic field, an electric field or both present. If an uniform magnetic field is assumed, the particle gyrates in a circular orbit around a magnetic field line, as can be shown from equation 2.1. The gyro frequency and gyro (Larmor) radius is given by the following equations

$$\omega_c = \frac{|q| \cdot B}{m} \tag{2.2}$$

$$r_L = \frac{\nu_\perp}{\omega_c} = \frac{m\nu_\perp}{qB} \tag{2.3}$$

where m is the particle mass, ν is the velocity of the particle perpendicular to

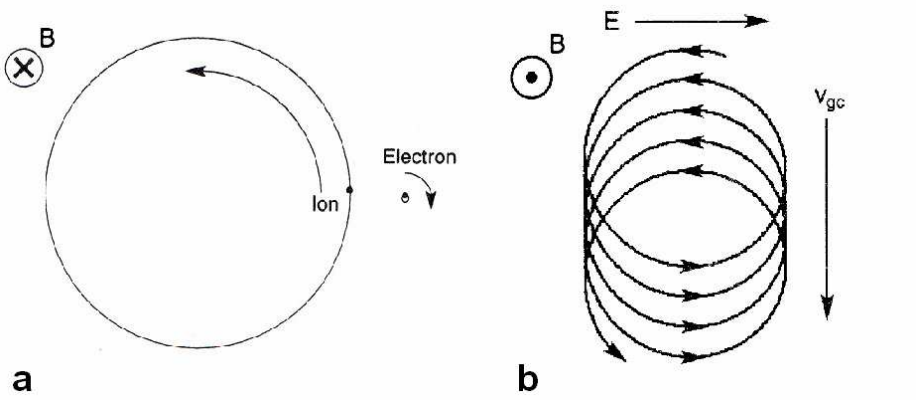

Figure 2.6: a) Motion of electrons and ions when a magnetic field is present. The direction of gyration is opposite for electrons and ions, where the ions have a larger gyro orbit. The magnetic field is directed into the page. b) $E \times B$ drift when both an electric and a magnetic field is present. The magnetic field is directed out of the page. Figure from Goldston and Rutherford [1995].

the magnetic field, q is the charge and B is the magnetic field strength. Positive and negative charges will gyrate in different directions, as illustrated in fig (2.6). Also, different masses will gyrate with different radius. The point in the middle of the orbit is called the guiding center.

Adding an uniform electric field E perpendicular to the magnetic field will give us a new equation of motion and a new drift of the particle called the $E \times B$ drift.

$$m\vec{v} = q(\vec{E} + \vec{v} \times \vec{B}) \tag{2.4}$$

From this it can be shown that the particle guiding center drifts perpendicular to both the magnetic and electric field, see figure (2.6), given by:

$$\vec{v} = \frac{\vec{E} \times \vec{B}}{B^2} \tag{2.5}$$

A gravitational field can be added which will make the motion more complicated. A gradient or a curvature in the magnetic field will also influence the particle motion.

2.4.2 Magneto hydrodynamics (MHD)

The magneto hydrodynamics (MHD) theory treats the particles as a collection of particles viewed as a single electrically conducting fluid moving in an electromagnetic field. When calculating the dynamics of a plasma, a special case of MHD is used, namely ideal MHD. The conductivity is here assumed to be infinite and is valid for space plasma with high temperature and where the resistivity is small. In this case, the magnetic field is frozen into the plasma.

Faradays law is given by

$$(\frac{\partial \vec{B}}{\partial t} = -\nabla \times \vec{E}) \tag{2.6}$$

Ampères law is given by

$$(\nabla \times \vec{B} = \mu_0(\vec{J} + \epsilon_0 \frac{\partial \vec{E}}{\partial t})) \tag{2.7}$$

The term proportional to the electric field, can be discarded when using the following argument:

$$|\vec{\nabla} \times \vec{B}| \approx \frac{B}{L}$$

$$\mu_0\epsilon_0|\frac{\partial \vec{E}}{\partial t}| \approx \mu_0\epsilon_0\frac{E}{\tau} = \frac{E}{c^2\tau}$$

where L and τ are the characteristic MHD length and time scales, respectively. $c = \frac{1}{(\mu_0\epsilon_0)^{\frac{1}{2}}}$ is the velocity of light. Since there are long distances with slow changes and non relativistic flow, which is required in MHD, the inequality

$$\frac{\mu_0\epsilon_0|\frac{\partial \vec{E}}{\partial t}|}{|\vec{\nabla} \times \vec{B}|} \approx \frac{E}{Bc}\frac{L}{c\tau} \approx \frac{\nu}{c}\frac{L}{c\tau} \ll 1 \tag{2.8}$$

is satisfied and the second term of eq. (2.7) can be dropped. Hence Ampères law in the ideal MHD limit is reduced to:

$$(\nabla \times \vec{B}) = \mu_0\vec{J} \tag{2.9}$$

The Ohm's law in MHD gives

$$\vec{J} = \sigma(\vec{E} + \vec{\nu} \times \vec{B}) \tag{2.10}$$

$\vec{J}$ is the current density, σ is the conductivity, $\vec{E}$ is the electric field, $\vec{\nu}$ is the plasma velocity and $\vec{B}$ is the magnetic field. $(\vec{E} + \vec{\nu} \times \vec{B})$ is the effective electric field seen by a fluid element moving with velocity ν across a magnetic field B. If the conductivity is assumed to be infinite, $(\vec{E} + \vec{\nu} \times \vec{B})$ must be zero.
The plasma drift velocity is given by

$$\nu_E = \frac{\vec{E} \times \vec{B}}{B^2} \tag{2.11}$$

as long as ideal MHD is valid.

The Reynolds number is given by $R_m = \mu_0 \sigma \nu L$, where L is the characteristic length, μ_0 is the magnetic permeability, σ is the conductivity and ν is the characteristic plasma velocity. It is a dimensionless number that gives the ratio between the convection term and the diffusion term. If $R_m > 1$, the convection of the field with the plasma dominates, and the plasma can be regarded as frozen to the field lines, hence the infinite conductivity is valid. In this case, the IMF remains connected to the solar wind plasma, and the Earth's magnetic field is coupled to the magnetospheric plasma, where the magnetopause acts as the boundary between the two.

Taking the curl on both sides of Ohm's law gives

$$\frac{1}{\sigma} \nabla \times \vec{J} = \nabla \times \vec{E} + \nabla \times (\vec{\nu} \times \vec{B}) \tag{2.12}$$

The electric field will be constant in time, since ideal MHD is assumed. Applying the modified Ampères law (eq. (2.9)) and Faradays law (eq. (2.6) into equation (2.12), we get

$$\frac{1}{\sigma \mu_0} \nabla \times (\nabla \times \vec{B}) = -\frac{\partial \vec{B}}{\partial t} + \nabla \times (\vec{\nu} \times \vec{B}) \tag{2.13}$$

Using the vector identity $\nabla \times \nabla \times \vec{B} = \nabla(\nabla \cdot \vec{B}) - \nabla^2 \vec{B}$ and Gauss law which says that B is divergenceless ($\nabla \cdot \vec{B} = 0$), equation (2.13) becomes

$$\frac{\partial \vec{B}}{\partial t} = \nabla \times (\vec{\nu} \times \vec{B}) + \frac{\nabla^2 \vec{B}}{\sigma \mu_0} \tag{2.14}$$

The convection of the magnetic field with the plasma is described by the first term on the right side, while the second term on the right side describes the diffusion of the field across the plasma. For more theory about plasma behavior, see Goldston and Rutherford [1995] or Kivelson and Russel [1995].

2.5 Magnetosphere

The magnetosphere, see figure (2.7), prevents most particles in solar wind from reaching the Earth. The factors that control the magnetosphere is the solar wind ram pressure ρV^2, the strength and direction of the IMF, and energetic particles originating from the Sun [Lepping et al., 2003].
The form of the boundary which separates the geomagnetic field and the solar wind magnetic field, can be derived from the pressure balance across the boundary. In the magnetosheath (described below), the solar wind has a pressure given by the following formula:

$$p_{sw} = N m_p v^2 \tag{2.15}$$

where N is the particle density in the solar wind, m_p is the proton mass and v is the velocity of the solar wind. The corresponding pressure in the magnetosphere

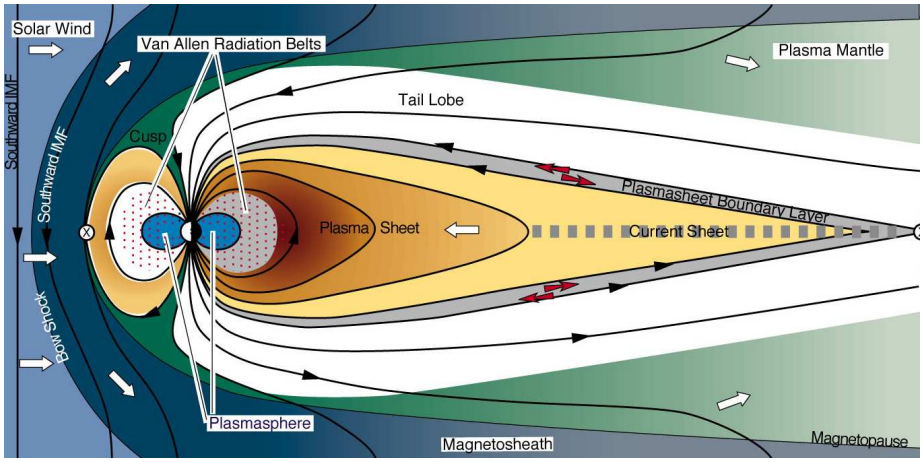

Figure 2.7: The magnetosphere with its particle regions. The direction of the Sun is to the left. The solar wind, with its embedded interplanetary magnetic field (IMF), meets the Earth's magnetopause. Here, the direction of the IMF is southward, i.e $B_z < 0$, and connects to the Earth's magnetic field lines at the X-line, which is indicated by a X inside a circle. The X-line is described in section (2.7). Plasma from the solar wind enters through the cusp, and is trapped in the plasma sheets. Eventually, the plasma is either precipitating to the Earth, or lost down the magnetotail. Figure from `http://space.rice.edu/IMAGE/livefrom/sunearth.html`.

which pushes the solar wind back is mainly a magnetic pressure. This pressure is given by [Mead and Beard, 1964]:

$$p_B = \frac{B^2}{2\mu_0} \tag{2.16}$$

where B is the magnetic field and μ_0 is the permeability of vacuum. A boundary region between the Earth's magnetic field and the solar wind is formed when a force balance exists between them. This region is called the magnetopause and it has a thin, but finite thickness of ~ 1 km [Hargreaves, 1992]. When the solar wind pressure increases, the magnetopause is pushed towards the earth where the geomagnetic field is stronger and its current is strengthened. The magnetosphere is then compressed and will exert an outward force to balance the new magnetic pressure. On the side facing the Sun the magnetosphere is thus shaped like a hemisphere, while it is drawn out on the nightside, see figure 2.7. The dayside magnetosphere is compressed to 10-12 R_E, while the magnetotail stretches out several hundred R_E. As a result of this deformation, there exist open field lines that are only connected to the earth on one side and to the IMF on the other side due to magnetic reconnection, see section (2.7). A shock front is formed 2 or 3 R_E upstream of the magnetopause. The region between this shock front and the magnetopause is called the magnetosheath and here the plasma is turbulent. Dayside reconnection opens the magnetic field lines at the magnetopause, causing shocked subsonic solar wind plasma to enter the magnetosphere, producing the dayside cusp and plasma mantle. The open field lines are next dragged into the magnetotail where they produce a low density

mixed plasma in the magnetotail lobes. During magnetotail reconnection, the plasma is compressed and form the plasma sheet which consists of hot particles. The energetic particles start to drift around the Earth due to the increase in particle energies in the plasma sheet as the field lines approach the Earth. Ions drift to the west and electrons to the east, forming the outer radiation belt and extending the plasma sheet to the dayside magnetosphere. The inner radiation belt is produced by cosmic rays and lies inside the plasmasphere. The plasmasphere rotates with the Earth's atmosphere, and does not take part in the large-scale magnetospheric convection. Reconnection is described in more detail in section (2.7).

2.5.1 Boundary layers

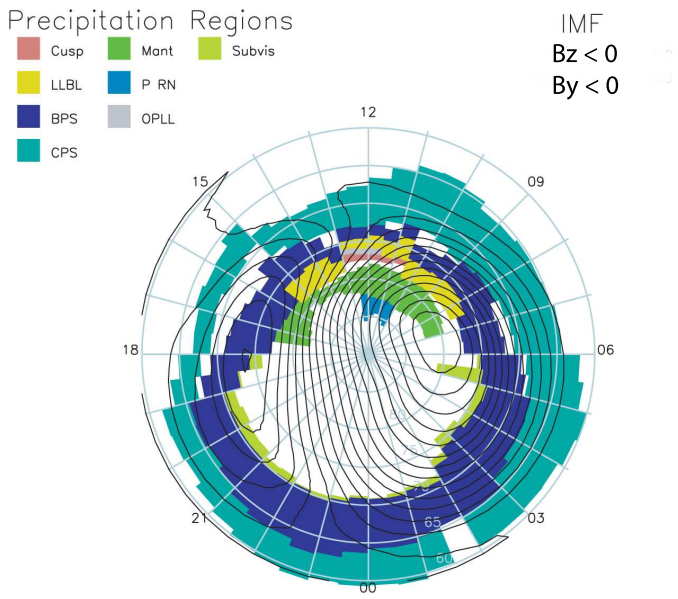

Figure 2.8: Precipitation regions in the ionosphere for negative IMF B_y and IMF B_z. In addition the inertial convection streamlines are superimposed. Modified from Newell et al. [2004].

The study of Newell and Meng [1992] presented the first probability maps for precipitation of plasma coming from the cusp, the low latitude boundary layer, the mantle, the boundary plasma sheet or the central plasma sheet into the ionosphere. Figure (2.8) shows a plot of one of their later results given in magnetic latitude (MLAT) and magnetic local time (MLT) coordinates, see chapter (3). Magnetic noon is at the top. The different precipitation regions are shown for IMF B_z and IMF B_y negative. The cusp in figure(2.7) here corresponds to the pink colored area. The plasma mantle is shown as the bright green area poleward of the cusp. The central plasma sheet and the plasmasheet boundary layer corresponds to the light blue and dark blue shaded areas, respectively. The white areas mean lack of significant precipitation. The polar

cap will have a polar rain signal which varies in intensity at all times, but in this case only polar rain above $\sim 0.1\frac{ergs}{cm^2}s$ is plotted, see Newell et al. [2004]. A short description of the various precipitation regions of interest is given below.

Cusp The cusp can be viewed as a direct entry layer for the solar wind plasma, and it contains lower energy magnetosheath plasma. It stretches out about 3h in magnetic local time to either side of noon, [Maynard et al., 1997]. The cusp energy and density are approximately the same as the frontside magnetosheath plasma. Ions have energies around 1keV, while electrons have their electron temperature typically between 30 eV and 100eV [Newell and Meng, 1992].

Low latitude boundary layer (LLBL) This boundary layer consists of a mix of both magnetosheath and magnetospheric plasma. Ion energies vary between some hundred eV up to 3keV, and electron energies vary between 100eV and 600eV. The electron temperature is typically 70 eV to 200 eV, and thus slightly higher than the cusp electron temperature. The bulk flow velocities are lower than the cusp, and the flux peak is about 10 times lower than the cusp [Newell and Meng, 1992]. The density varies from $0.5cm^{-3}$ to about $10cm^{-3}$, while the flow velocities vary from about 100 km/s to magnetosheath values. The temperatures can be anything from 100 to 1000-2000 eV [Newell et al., 1991b]. The LLBL can be located on open or closed field lines, but more commonly on partially open or partially closed field lines. The frontside of the magnetopause is typically open [Newell et al., 2004].

High-latitude boundary layer (HLBL) This region is also known as the plasma mantle. The mantle consist of de-energized magnetosheath plasma with ion energies below 1keV and electron energies near the polar rain level of a few hundred eV. The temperature is around 100 eV, with densities around a few times $10^{-2}cm^{-3}$ to $10^{-1}cm^{-3}$ and the typical flow velocities are 100-200 km/s [Newell et al., 1991a] and [Newell et al., 1991b]. The HLBL is located on open magnetic field lines [Newell et al., 2004].

Polar rain is found all over the polar cap, and it consists of electrons up to a few hundred eV [Winningham and Heikkila, 1974]. The polar rain is in the high latitude polar cap and coupled to open magnetic field lines [Newell et al., 2004].

2.6 Ionosphere

The upper region of the Earth's atmosphere is called the ionosphere. This conducting layer is therefore coupled to the neutral atmosphere at low altitudes and the magnetosphere at high altitudes. A significant, but small amount of the neutral atoms is ionized. As a result of this ionization we get a plasma, which is free electrons and ions [Brekke, 1997].

2.6.1 Sources of ionization

The ionosphere is created through ionization of neutral atoms and molecules of the atmosphere, and thus can be viewed as a variable shell of ionization

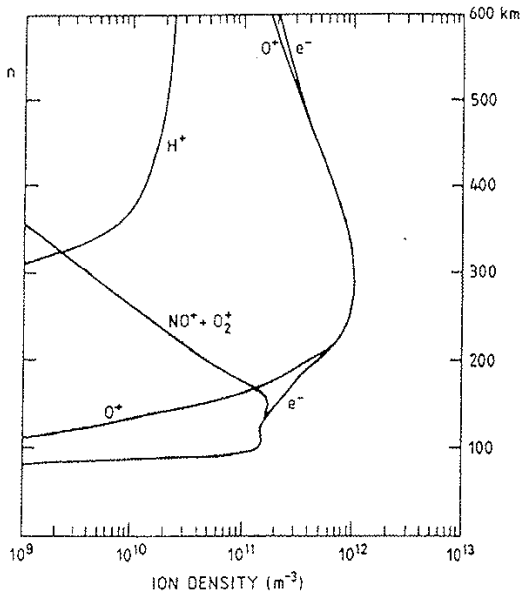

Figure 2.9: The ionosphere between 100 and 600 km showing the altitude profiles of the most common ion species. Figure from Brekke [1997].

(plasma) surrounding the Earth. Various molecular constituents dominate the ion composition for different regions in the neutral atmosphere. H^+ for instance dominates the region above 600 km, while O^+ can dominate up to 600 km, see figure (2.9). To be able to ionize the neutral atoms and molecules in the atmosphere, an energy source is needed. At middle and low latitudes the level of ionization is controlled by solar radiation which means extreme ultraviolet (EUV) radiation, UV rays and x-rays, while precipitation of energetic particles is the dominant source at high latitudes [Hargreaves, 1992].

Photoionization

The altitude profile of the rate of ion production Q must be calculated to model an ionosphere produced in a neutral atmosphere. The altitude profile will have a peak at some altitude, due to the dependency on neutral density and the incoming solar radiation intensity. The neutral density decreases with height, while the solar radiation intensity increases with height. An analytical approach to ionosphere modeling is known as the "Chapman theory", [Chapman and Bartels, 1940]. This theory describes the ion production as a function of height for the case where details of photon absorption are hidden in a radiation-absorption cross section σ, and where ion production depends only on the amount of radiative energy absorbed. The Chapman production function is given by:

$$Q = Q_m exp[1 - y - exp(-y)] \tag{2.17}$$

where Q is the rate of ion production (electrons per square meter per second), Q_m is the ion production at maximum, $y = \frac{h-h_m}{H_n}$, where h is the altitude, h_m is the altitude for the maximum of production and H_n is the scale height.

This function assumes a flat earth where the solar zenith angle χ is fixed. In reality, this angle varies with position on the surface of the Earth. If the local production rate is referred to the production maximum at the subsolar point Q_{mo} and at a height h_{mo}, the equation becomes:

$$Q = Q_{mo} exp[1 - z - sec\chi exp(-z)] \tag{2.18}$$

$$h = h_{mo} + ln(sec\chi) \tag{2.19}$$

$$Q_m = Q_{mo} cos\chi \tag{2.20}$$

where z is an altitude coefficient given by $z = \frac{h - h_{mo}}{H_n}$. Thus, the altitude of the maximum production rate increases with solar zenith angle, and the rate of ionization decreases with increasing latitude. [Luhmann, 1995]

Impact ionization

The dominant source of atmosphere ionization is mainly solar photons, but occasionally energetic precipitating particles are more dominant. By energetic particles, energies $\geq 1keV$ are considered. The particle energy flux is reduced with decreasing altitude as the density in the atmosphere increases. The particles gradually loose energy from collisions as they travel. One way to estimate the effects of energetic particle impact is to use an empirically determined function called the "range-energy relation", $R(\xi_0)$. This relation gives the depth of penetration in a particular medium as a function of the incident-particle energy (ξ_0). The range is typically expressed in units of grams per square centimeter.

$$x = \int_0^{\eta} n_n(s) ds \tag{2.21}$$

Equation (2.21) gives the relationship between the distance x and the matter density n_n along the path of the particle s. The point of interest along s is η. The vertical incidence x is related to the altitude h by the following formula:

$$x = \int_{\eta}^{\infty} n_n(h) dh \tag{2.22}$$

The stopping altitude also needs to be calculated and this is done by finding η in equation (2.22) for which $x = R(\xi_0)$. The range-energy relation gives the depth to which the particle penetrates, but the altitude distribution of the energy loss cannot be found through this relation [Luhmann, 1995].

Loss processes

When the ion production rate is known, the ion or loss rate (L) must be determined. There exists an equilibrium between production and loss of ionization, and hence electrons and ions tend to recombine. The rate of change of electron density is expressed by a continuity equation

$$\frac{\partial N}{\partial t} = Q - L - div(N\vec{v}) \tag{2.23}$$

where Q is the production rate, L is the recombination loss rate, $\vec{v}$ is their mean drift velocity and $div(N\vec{v})$ is the loss of electrons by motion [Hargreaves, 1992].

The most important recombination mechanisms which can take place for electrons are ([Luhmann, 1995]):

- Radiative recombination ($e + X^+ \rightarrow X + h\nu$). This type of recombination is rather slow and is not significant in the E and F regions [Hargreaves, 1992]
- Dissociative recombination ($e + XY^+ \rightarrow X + Y$) is significantly faster.
- Attachment ($e + Z \rightarrow Z^-$)

The recombination rate is given by:

$$L = \alpha n_e n_i$$

where α is the recombination coefficient determined by empirical and theoretical methods, n_e is the electron density and n_i is the ion density. Below approximately 200 km there are primarily short-lived molecular ions which tend to recombine rapidly with thermal electrons. Molecular ions will therefore dominate the E-region, while atomic ions tend to dominate the F region [Luhmann, 1995]. The electron density decreases at night due to the absence of solar radiation.

Through the ionosphere, the electron density varies with the time of day,

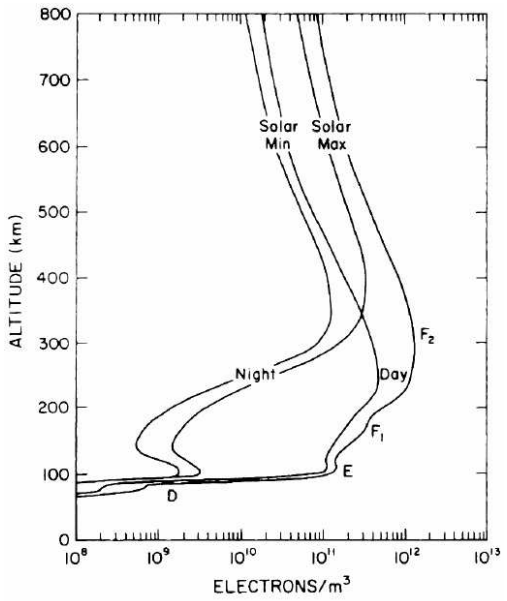

Figure 2.10: Electron density profiles as a function of height for solar maximum and minimum conditions at daytime and night-time. The different ionospheric layers are labeled. Figure from Brekke [1997].

season, solar cycle and the level of magnetospheric or solar wind disturbance [Brekke, 1997]. Figure (2.10) shows the various layers (described below), the electron density profiles as a function of height for solar maximum and minimum.

Ionospheric layers

The ionosphere is divided into D, E and F layers, however, there isn't a clear distinction between these layers. Below, the various layers are described briefly.

D layer The D layer extends from 60 and 90 km. This region has a smaller electron density than the other layers, and it varies a lot [Brekke, 1997]. The pressure is high and various ionization sources contribute to the ion production [Hargreaves, 1992]. This layer can contain negative ions.

E layer This was the first detected layer, and it is located between 90 and 150 km. The name is due to reflection of electric fields. The electron peak of this layer is around 110km in daytime, and the dominating ions are mainly O_2^+ and NO^+. The degree of ionization increases above this region. The E-region is dominated by collisions where Hall and Pedersen currents are significant [Brekke, 1997].

F layer O^+ ions formed by solar irradiance dominate the F-region above $\sim 150km$. This region is further divided into two separate layers, F1 and F2 due to a second peak of electron density that occasionally appears. The F2 region has the largest electron concentration. [Hargreaves, 1992; Luhmann, 1995].

2.6.2 Hall and Pedersen currents and Joule heating

Above 200km, collisions between neutral particles and ions/electrons are not very frequent. Electrons and ions will therefore move together in the presence of an electric field $\vec{E}$ and are frozen to magnetic field lines $\vec{B}$. The flow direction is perpendicular to both $\vec{E}$ and $\vec{B}$, with a velocity given by equation (2.24). Subscript e refers to electrons and i refers to ions.

$$\vec{v}_e = \vec{v}_i = \frac{(\vec{E} \times \vec{B})}{B^2} \tag{2.24}$$

This equation is valid above 200km, and it doesn't apply to the E-region where the collisions with neutral particles occur frequently. Under 140km, an average ion will not be able to complete a gyrocycle before it collides with a neutral particle (n). The motion will be resumed under the influence of an $\vec{E}$-field, and it will begin a new gyroarc until the next collision occurs.
The ion-neutral collisional frequency is given by ν_{in}. When the gyrofrequency Ω_i is equal to ν_{in} (at about 140 km), the particles will drift at an angle 45° to the $\vec{E} \times \vec{B}$ drift. When $\Omega_i >> \nu_{in}$ below 140km, ions no longer drift with the $\vec{E} \times \vec{B}$ drift. Since $\nu_{in} >> \nu_{en}$, electrons are bound to the geomagnetic-field line more than the ions are. Electrons will therefore drift with the $\vec{E} \times \vec{B}$ drift down to $\sim$ 90km. Ion motion relative to electrons arising from the different effects of neutral collisions hence produces an electric current in the ionosphere given by.

$$j = \sigma E = n_i e(\nu_i - \nu_e) \tag{2.25}$$

where n_i is the concentration of current carriers, i.e the plasma density. Ions will drift relative to the electrons primarily between 90km and 140km. The current perpendicular to $\vec{B}$ and parallel to $\vec{E}$ is called the "Pedersen current".

The current perpendicular to both B and E is called the "Hall current", and finally the component parallel to B is called the "Birkeland" or "field aligned" current. When ions and neutral particles at lower altitudes collide, they will loose some of their kinetic energy in each collision. It releases heat which is called "Joule heating".

2.6.3 Electron temperature

The electron temperature in the ionosphere provides information about precipitation in the magnetospheric boundary layers, the cusp and the low-latitude boundary layer (LLBL). This is due to heating of the electron gas by low-energy magnetosheath precipitation. The study of Wickwar and Kofman [1984] found enhanced electron density and electron temperature which occurred simultaneously in the F-region ionosphere. Watermann et al. [1994] and McCrea et al. [2000] among others reported this to be a rather frequent phenomenon.
Lockwood et al. [1993] showed that electron temperature enhancements sometimes lead to a series of poleward-moving events. In addition to electron heating, electron cooling exist. The cooling rate (C_r) of the electron gas in the ionosphere is often the primary variable determining the quasi steady state electron gas temperature. The electron gas cools by two processes: downward heat conduction, and by collisions with ions. The cooling rate by ion collisions is proportional to the number of electrons times the number of ions. When the plasma is electrically neutral, the ion and electron number are equal, and the cooling rate is proportional to the square of the electron density [Carlson, 1998].

$$C_r \propto n_e n_i = n_e^2 \tag{2.26}$$

The T_e cusp signature can be suppressed by this cooling effect below 400 km [Doe et al., 2001].

2.6.4 Ionospheric signatures

Aurora Borealis (northern lights) and Aurora Australis (southern lights) are the visible signatures of processes driven by the solar wind. Aurora have been observed through centuries and the phenomenon has been explained in various ways. The northern light was often said to be a sign of war, disasters or plagues, and in ancient times most people were afraid of these lights.

Now, modern instruments have revealed that aurora is created by precipitating charged particles which collide with neutral particles in the Earth's ionosphere. During collision, the particles excite and thus emit light. The area of northern lights can be viewed as a belt known as the auroral oval, see figure (2.11). This oval can be regarded as fixed in space with reference to the Sun, and it marks the boundary between open and closed field lines. When the Earth rotates underneath, daily variations in the aurora's location occur. This is why Svalbard is underneath the auroral oval during daytime, while northern Norway is underneath the auroral oval during nighttime, see figure (2.11). The shape and location of the oval varies greatly with solar activity. When the activity on the sun increases, the auroral oval expands towards the equator [Feldstein, 1967], and when the activity is low, the oval contracts poleward. As a result of

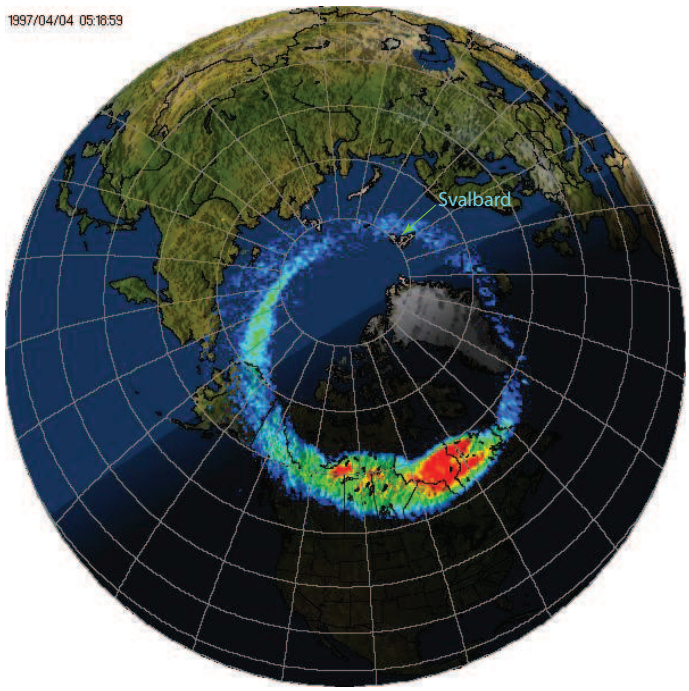

Figure 2.11: Image of the auroral oval in the northern hemispheres taken by the Ultraviolet Imager (UVI) onboard the NASA satellite "Polar" on April 4, 1997 at 0519 UT. The image is to illustrate Svalbards location inside the auroral oval during daytime. Please note that the date of the image has nothing to do with the observations performed in this thesis. Figure modified from `http://sd-www.jhuapl.edu/Aurora/UVI_on_Earth.html`.. The oval is regarded fixed in space relative to the Sun, while the earth rotates underneath. Figure from `http://www.northern-lights.no/`.

this, the ESR will sometimes be located inside and sometimes located outside the polar cusp boundary. The cusp location may vary within the range $\sim$ 70-79 MLAT [Sandholt et al., 1998].

2.7 Magnetic reconnection

Magnetic reconnection can be described as merging of magnetic field lines [Parker, 1957]. In our case it will involve merging of interplanetary magnetic field lines and terrestrial magnetic field lines. Dungey [1961] was the first to suggest that this merging of field lines, when the fields are antiparallel, is responsible for the coupling of solar wind energy into the magnetosphere. This process could transfer magnetic flux from the dayside magnetosphere to the magnetotail in case of southward IMF and from the tail to the dayside magnetosphere when it was northward [Dungey, 1963]. However, it was later pointed out that merging can occur where the two fields are not exactly antiparallel as well, cf. [Cowley, 1976]. The study of Crooker [1979] presented a qualitative model of the sites of magnetic field merging on the magnetopause.
The frozen-in criterion states that if the electrical conductivity of a fluid is large enough, perpendicular motion between the plasma and the magnetic field is impossible, and the plasma is frozen to magnetic field lines. For reconnection to take place, the frozen-in criterion must break down, which means that the Reynold number discussed in section (2.4.2) must be very small compared to unity. Thus, σ must be finite and L must be small, to give $R \ll 1$. Consequently, ideal MHD breaks down and the plasma is no longer frozen to magnetic field lines.
Figure (2.12) shows how the reconnection process occurs in the magnetotail. The magnetic field lines have opposite polarity and convect towards each other in the inflow region. The oppositely directed field lines must have a current sheet between them due to Amperes law ($\nabla \times \vec{B} = \mu_0 \vec{j}$). The current intensifies when the current sheet gets thinner as field lines move closer together. Reconnection occurs when the current sheet no longer can maintain its minimum thickness. The reconnection area is a small diffusion region centered around a magnetic X-line. Outside the diffusion region, the magnetic field lines are still frozen to the plasma. Inside the ion-diffusion region, the ions are no longer attached to the field lines and the ions are able to move freely around, while electrons still remain frozen to their field lines and continue convecting towards the reconnection X-line. When entering the electron diffusion region, the electrons are no longer frozen to the field lines. When the frozen-in criterion breaks down, the opposite directed field lines can merge together and magnetic energy is released to the surroundings [Øieroset et al., 2001]. Magnetic energy is converted to kinetic energy which is sent out through high-speed plasma jets. These jets transfer mass, energy and momentum to the Earth's magnetosphere along magnetic field lines. At middle and low latitudes the ionosphere is contained within a region of closed field lines. At high latitudes the geomagnetic field can reconnect with the interplanetary magnetic field and thus open the ionosphere to the driving force of the solar wind. As soon as the newly reconnected field lines leave the diffusion region, they once again become frozen to the plasma.

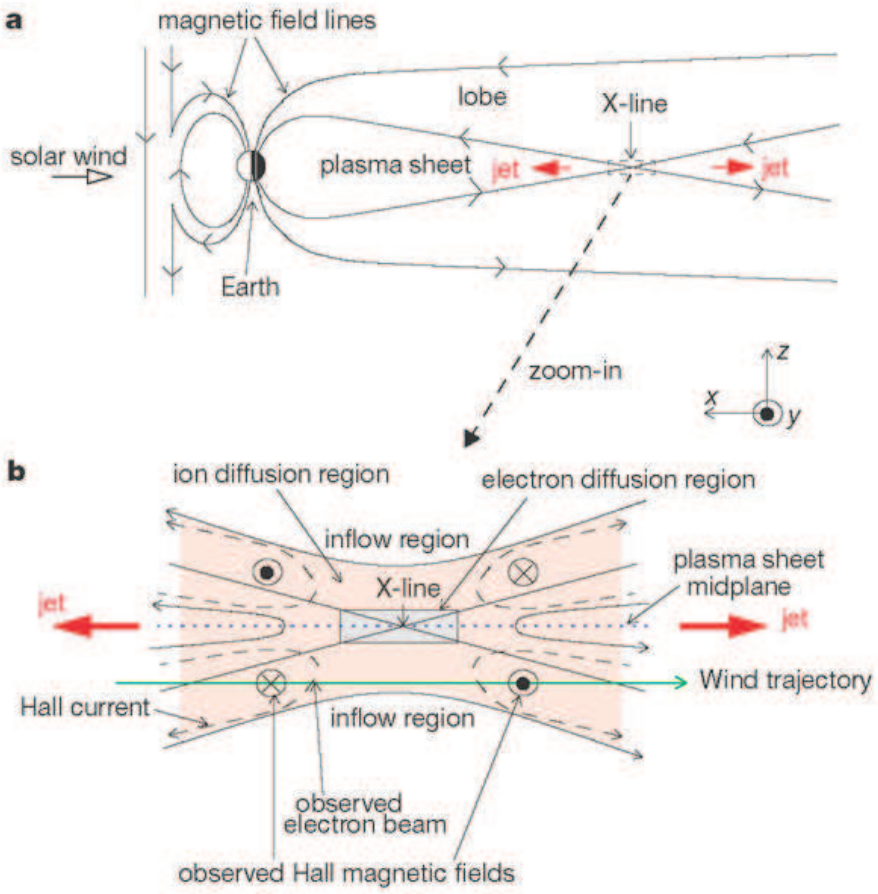

Figure 2.12: a) Illustration of the magnetosphere, showing dayside magnetopause and nightside reconnection. In the magnetotail, oppositely directed field lines convect towards the low-latitude plasma sheet, touch each other and reconnect at an X-line. b) The magnetic reconnection in the magnetotail blowed up. The figure illustrates the X-line where the field lines reconnect. The shaded red area indicates the ion diffusion region and the grey square in the middle indicates the electron diffusion region. Incoming field lines are labeled A and B, while the reconnected magnetic field lines are labeled A' and B'. Red arrows named "jet" indicate the fast plasma outflow from the reconnection region. In the ion diffusion region, a system of Hall currents are created by the separation between ions and electrons at the ion scale, which again induces an out-of-plane magnetic field pattern. The WIND spacecraft observed this as it traveled from the earthward to the tailward side of the X-line. The trajectory is indicated by a green line. WIND also detected electron motion near the boundary between lobe and plasma sheet. The coordinate system is defined such that x points towards the Sun, z is normal to the current sheet and y is directed out of the plane. Figure from Øieroset et al. [2001].

2.7.1 The Dungey cycle

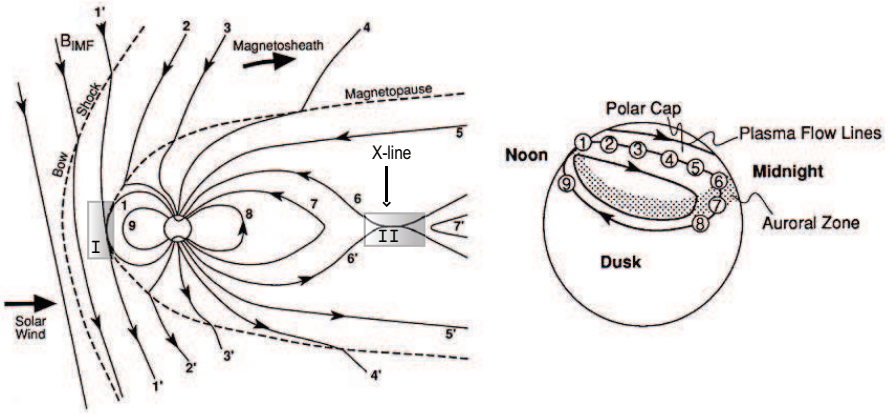

Figure 2.13: Illustration of the Dungey Cycle, showing both the IMF coming from the left, terrestrial field lines, and the reconnected field lines. Regions I and II are the diffusion regions (not to scale), which indicate where reconnection takes place according to the model. The figure to the right shows the feet of the numbered field lines in the northern high-latitude ionosphere and the corresponding high-latitude plasma flows. It also indicates the antisunward flow in the polar cap and the corresponding return flow at lower latitudes. Figure modified from Kivelson and Russel [1995].

The Dungey cycle (1961) is an open magnetosphere model in which the plasma flow is generated principally by reconnection at the magnetopause between the terrestrial magnetic field and the IMF, see figure (2.13). For the case of a southward orientation of the interplanetary magnetic field IMF B_z, i.e IMF B_z negative, reconnection takes place at the subsolar magnetopause near noon. For azimuthal IMF, that is B_y positive or B_y negative, the site of reconnection in the northern hemisphere shifts respectively duskward or dawnward [Cowley and Lockwood, 1992].
Figure (2.13) shows the Earth's magnetosphere and how the plasma flow therein is driven by magnetic reconnection. Field line (1) shows a terrestrial field line which meets an interplanetary field line with negative orientation of the B_z component. The IMF B_y component is not present here. The field line reconnects in region I and is further dragged across the polar cap towards the magnetotail while it stretches out along the tail. At point (6) in the tail the field line reconnects again at a second X-line, and the reconnected field line then returns to the dayside at lower latitudes. Field lines 2-5 are open field lines. The picture inserted to the right in figure (2.13) shows the plasma flow in an antisunward direction through the polar cap and the return flow from point (6) at lower latitudes. The Dungey cycle is described as quasi-steady reconnection which means that the merging of field lines varies only slowly with time in the large-scale continuous process [Dungey, 1961].

2.7.2 Transient reconnection

Transient (pulsed) reconnection is another type of reconnection mechanism that occur at the dayside magnetopause. Evidence for this type of magnetic reconnection was first discovered by [Russel and Elphic, 1978] and Haerendel et al. [1978] independent of each other. Transient magnetic reconnection is called a"pulsating cusp model" because reconnection may take place in a series of discontinuous events. It is presumed to be the main flux transfer mechanism from the magnetosheath to the magnetosphere, i.e. it is named Flux Transfer Events (FTEs) [Russell and Elphic, 1979; Lockwood et al., 1993]. Lockwood et al. [1995] showed that the total contribution of FTEs can be in the range of 50-200 kV. This could be produced by only one large event per repetition period. When the total contribution exceeds $\sim 60kV$ this can imply a number of side-by-side events at different MLTs. Figure (2.14) shows a burst of magnetopause reconnection

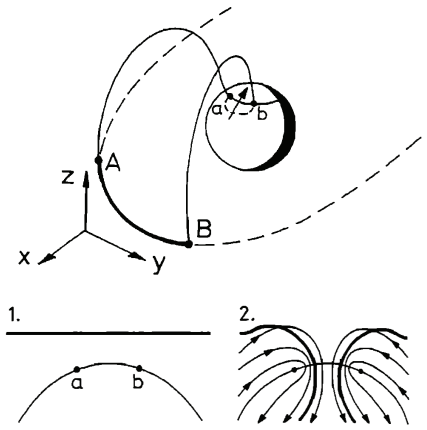

Figure 2.14: The uppermost figure shows a projection of the magnetopause reconnection X-line (AB) to the ionospheric merging gap (ab). The dashed line is the low-latitude magnetopause. The lowest figure shows the dayside ionospheric flow patterns for pulsed reconnection; the first showing between pulses, while the second is during the pulse. The merging gap is fixed in the Earth's frame. Both figures has noon at the top and dawn to the right. The solid line in the first figure shows a line of constant plasma density. Figures from Lockwood and Carlson Jr. [1992].

which applies a voltage along the X-line AB and causes a merging gap ab (the ionospheric projection of the reconnection X-line). On average the repetition period between the bursts is 7 minutes [Lockwood and Carlson Jr., 1992]. The lowest part of (2.14) shows the ionospheric flow pattern. Panel 1 shows no flow between the pulses, while panel 2 shows the full reconnection voltage appearing as flow across the merging gap ab during the reconnection pulses. Polar cap patches, to be described later, is by Lockwood and Carlson Jr. [1992] and others thought to be produced by transient bursts of dayside reconnection.

2.7.3 Interplanetary magnetic field dependency

The northern and southern hemispheres become asymmetric when IMF B_y is dominating. For positive IMF B_y, the force indicated with black arrows in

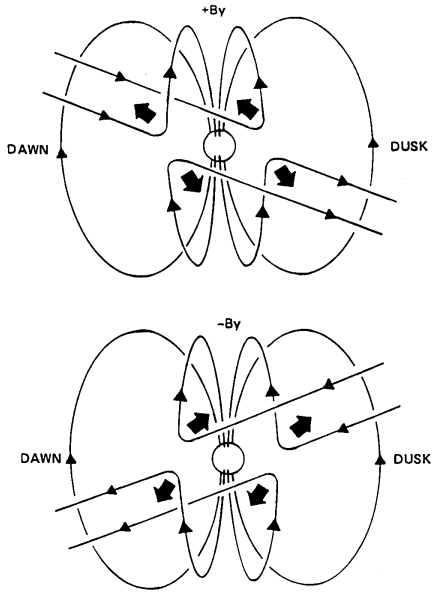

Figure 2.15: Newly reconnected field lines viewed from the Sun for positive (upper panel) and negative (lower panel) IMF B_y components. The large arrows indicate the direction of the forces associated with the magnetic tension which acts on the magnetic field lines. Figure from Gosling et al. [1990].

figure (2.15) upper panel will pull the newly reconnected field lines towards the dawnside of the northern hemisphere and duskside in the southern hemisphere, as the field lines move tailwards with the solar wind. The reverse takes place for negative IMF B_y, see figure (2.15) lower panel.
In the previous subsections, the situation of negative IMF B_z has been described, but reconnection can take place for positive IMF B_z as well as for negative IMF B_z [Gosling et al., 1990]. Dungey [1963] was the first to suggest an opportunity for reconnection to take place for B_z positive, and the first observation of this type of reconnection was found by Maezawa [1976]. The main difference between negative (lobe reconnection) and positive IMF B_z (low-latitude reconnection) is that positive B_z generates open flux, while negative B_z only reconfigure already open flux. Figure (2.16) shows two cases of northward IMF where open field lines are labeled o, closed field lines are labeled c, interplanetary field lines are labeled i, and overdraped lobe field lines are labeled ol. Overdraped lobe field lines are open field lines which are reconfigured by lobe reconnection. The dashed line is the magnetopause (MP) and the marked X's indicate were reconnection takes place. The left panels have the Sun to their left, while the Sun is at the top of the right panels. Convection flow stream lines are marked with arrows. Viscous-driven flow cells are labeled ν, while lobe flow cells are labeled L. The top row shows lobe reconnection between a draped

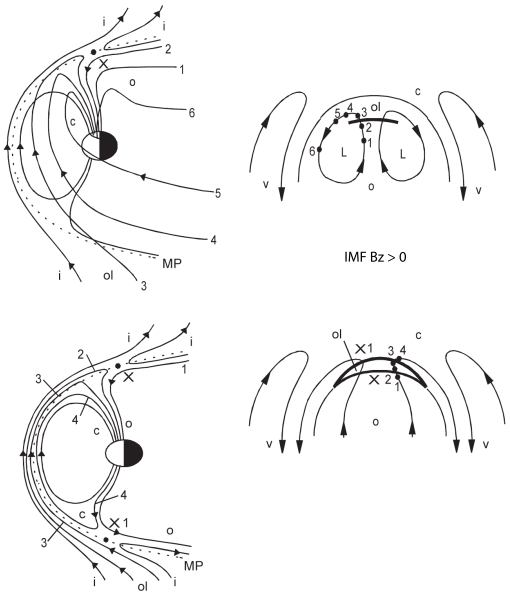

Figure 2.16: Reconnection geometry for two cases of northward IMF. The left panels show the evolution of reconnected field lines in the magnetosphere. The right panels show the flow in the northern hemisphere ionosphere where noon is at the top and IMF $B_y \approx 0$. Figure adapted from Lockwood and Moen [1999].

interplanetary magnetic field line (i) and the "old" open flux of the tail lobe. The bottom row shows the case where the overdraped lobe flux produced by X is itself reconnected at X1 in the other hemisphere to produce a closed field line [Lockwood and Moen, 1999]. For further reading about magnetic field reconnection theory and the interactions between the solar wind and the magnetosphere, see Pudovkin and Semenov [1985].

2.8 Convection

The plasma in the high-latitude ionosphere is kept in motion by processes that couple energy and momentum from the solar wind into the Earth's magnetosphere [Cowley et al., 1991], and that is what is called convection. The large-scale convection pattern is generally complex and time-varying, but for much of the time it has a two-cell pattern which follows an antisunward flow across the polar cap and a sunward return flow at lower latitudes [Cowley and Lockwood, 1992].

The IMF-dependency of the convection was first studied by Heppner [1977] and Heppner and Maynard [1987]. These studies presented qualitative ionospheric convection patterns that were ordered by the IMF clock angle. Heelis and Lowell [1982] made a model to reproduce the high-latitude ionospheric convection pattern by mathematical expressions. However, the model was not capable of producing separate flow cells at the same local time. Later, more quantitative

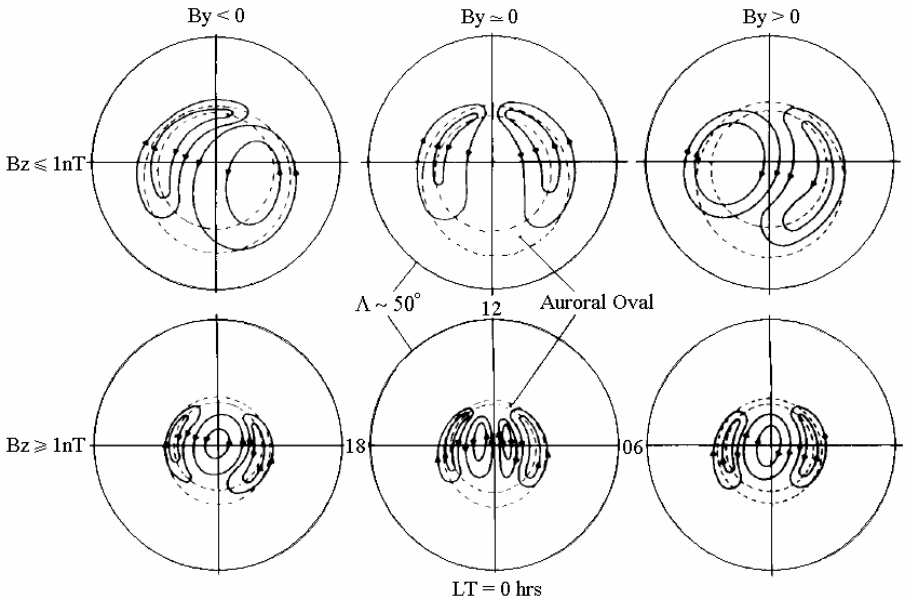

Figure 2.17: Convection patterns of the high-latitude ionosphere in the northern hemisphere for different orientations of the IMF. Figure adapted from Lockwood [1991].

techniques were used to characterize the convection pattern in terms of the IMF orientation.
Figure (2.17) shows the convection patterns in the northern hemisphere in terms of the IMF orientation. The northward IMF B_z component is directed out of the page, while the dawn-to-dusk IMF B_y component is directed from east to west. Magnetic noon is at the top. The spatial extent and the magnitude of the flows are related to the north-south component B_z. For negative IMF B_z (southward), the flow system is larger and stronger than in the case of positive (northward) IMF B_z [Fairfield and Cahill Jr, 1966]. The well-defined two-cell pattern that is dominating for negative IMF B_z is often referred to as "twin cells", while for positive IMF B_z, the convection weakens and the pattern can break apart with one or more additional cells of reversed convection, see figure (2.17). The additional cells appear on the dayside and are called "Lobe cells". They have flow towards the Sun in the polar cap between the cells, while twin cells have antisunward flow in the polar cap between the cells. The IMF B_y component control the dawn-dusk asymmetries which are oppositely directed in the different hemispheres, see figure(2.15). For positive IMF B_y the dusk cell becomes more dominant and rounded, while the dawn cell gets rounded for negative IMF B_y.

The motion of newly reconnected field lines set up an E-field in the high-latitude boundary layer (HLBL), which is mapped down to the ionosphere along the magnetic field lines. The polar cap electric field normally has a value between 50-100kV. The observed convection pattern is set up by the $E \times B$ plasma drift in the high-latitude ionosphere [Siscoe et al., 1991].

The convection pattern is theoretically explained by the Dungey (1961) "open" model of the magnetosphere, where the amount of open flux in the magnetosphere, and the magnitude of the internal flow, is determined by the IMF B_z component. The Svalgaard-Mansurov effect, together with similar effects are related to the sign of IMF B_y. It results from the east-west tension exerted on newly open dayside flux tubes. This leads to asymmetries in the convective flow [Jørgensen et al., 1972; Cowley et al., 1991]. The convection pattern is thus highly dependent on the IMF orientation.
At low latitudes, the ionospheric plasma is co-rotating with the Earth. However, at higher latitudes, the flow depends on:

1 The magnetopause coupling process principally by dayside reconnection (see sections 2.7.1 and 2.7.2).

2 Tail reconnection, e.g. during substorms. The tail process is related to the IMF's pre-history.

The total flow in the magnetosphere-ionosphere system is a sum of these two mechanisms [Cowley and Lockwood, 1992]. Only when the rate of dayside and nightside reconnection is equal, the pattern will be a steady flow.

Occasionally, the convection is affected by auroral substorms [Weimer, 1999]. The convection is also season dependent and exhibits yearly variations due to the solar cycle. The latter is however minor compared to IMF and season. Most of the variability associated with the seasonal effect is found in the dawn cell.

2.9 Patches and the tongue of ionoization (TOI)

There are two types of plasma within the polar cap; the low density background plasma, and the high density solar EUV ionized plasma. The solar produced plasma enters the polar cap through the cusp inflow region from sub-auroral latitudes yielding a tongue of ionization (TOI) [Knudsen, 1974; Foster et al., 2005; Moen et al., 2008]. TOI is regarded as a homogeneous stream of enhanced plasma following the convection streamlines, but it is often divided into a series of patches. Sato [1959] was the first who postulated the existence of the TOI. The study of Foster et al. [2005] showed that the TOI is entrained in the high-latitude convection pattern during disturbed conditions. Now, it is generally accepted that the TOI is driven by the large-scale magnetospheric convection electric field.

The polar F region density structures can be divided into two main types; that is patches and sun-aligned arc structures. A polar cap patch has a density which is 2-10 times larger than the surrounding background electron density [Buchau et al., 1983; Weber et al., 1984; Crowley et al., 2000]. The airglow emission at 630 nm is also enhanced above the background level. The patches extend 100-1000 km horizontally and were first discovered by Weber et al. [1984]. Weber et al. [1984] found that the patches are observed during moderately disturbed geomagnetic conditions ($K_p > 4$).The temperature of the electrons in a patch is low and unstructured, which indicates that auroral electrons do not

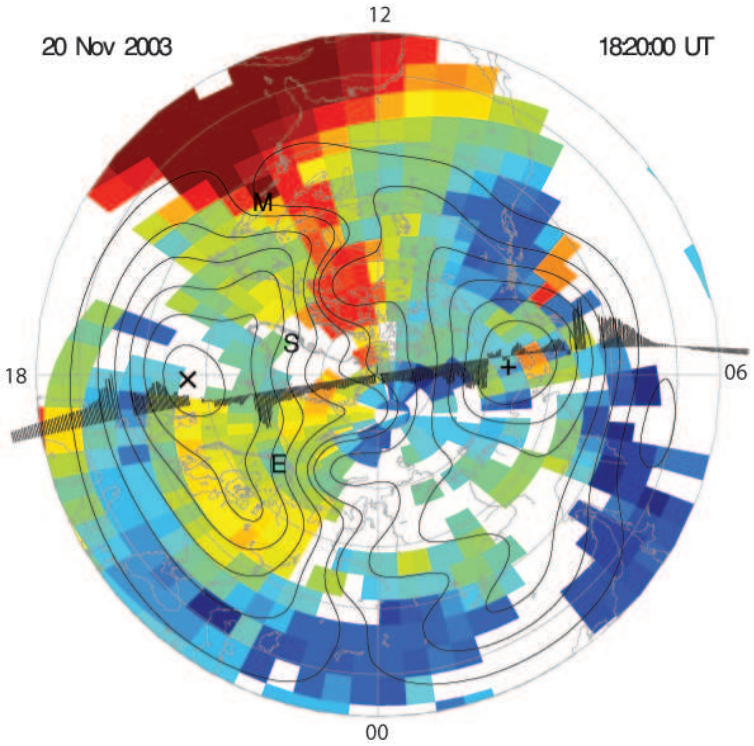

Figure 2.18: Shows a merged TEC-convection map from 20 November 2003. The SED/TOI plume is observed as a continuously tounge (shown in red) coming from a low-latitude source in the post-noon sector, extending through the dayside cusp and further across the polar cap to the midnight sector over the EISCAT Svalbard radar, named E in the figure. M is the Millstone Hill ISR, while S is the Sondrestrom radar. An overflight of the F13 satellite is also shown, where the driftmeter data have been combined with the SuperDARN observations to determine the superimposed convection pattern. It clearly indicates antisunward flow over the polar regions and sunward convection below 60° latitude. Figure adapted from Foster et al. [2005].

precipitate into the patch when it is located inside the polar cap [Rodger et al., 1994a]. Patches drift across the polar cap with speeds between 300 to 1000 m/s. They are observed both in winter and summer and are most prominent at sunspot maximum. Often, but not always, the polar cap patches are observed to occur simultaneously in geomagnetic conjugate regions [Rodger et al., 1994b]. When the patch is observed outside the polar cap, it has already passed through the polar cap and is called a "blob". The blobs are divided into three types named in order of increasing latitude of occurrence; sub-auroral blobs, boundary blobs, and auroral blobs. Boundary blobs are found nearby the equatorward auroral boundary [Crowley, 1996]. Auroral blobs is probably formed by particle precipitation, while the others are formed by transport effects. Weber et al. [1984] found that there could be a relation between patches and nightside "blobs" from the observations performed by the Chatanika radar. Previously the patches were identified using ionosondes (e.g [Buchau et al., 1983; Dandekar and Bullett, 1999]), and all-sky imaging photometers. Now, incoherent scatter radars and HF radars, among other techniques are used as well.

The occurrence of patches is dependent on the orientation and the strength of the IMF [McEwen and Harris, 1996; Hosokawa et al., 2006; Moen et al., 2008]. The polar cap is populated with patches for IMF $B_z < 0$, while it is populated by sun-aligned arcs for IMF $B_z > 0$ [Crowley, 1996]. The patches seems to form when the B_z component of the interplanetary magnetic field is negative [Buchau et al., 1983; Rodger et al., 1994a; McEwen and Harris, 1996], but Oksavik et al. [2006b] have reported a special case where a patch formed in a lobe cell due to particle precipitation for northward IMF. The same study showed that patches may form even poleward of the open closed boundary (OCB).

There are most likely several patch creating mechanisms that form the patches, and the different mechanisms are usually explained by plasma transport, rather than in-situ production. However the most accepted explanation is that patches are formed by the solar EUV ionization at subauroral latitudes, whereby the solar produced plasma follows the global convection pattern, yielding a tongue of ionization (TOI) that drifts into the polar cap [Knudsen, 1974]. Buchau et al. [1985] confirmed this theory when he found electron densities in the patches that were similar to densities observed at subauroral latitudes.

MacDougall and Jayachandran [2007] propose a different type of patch generation mechanism that focused on the return travel from the nightside to the dayside around the dawn convection cell. They suggest that most of the electron enhancement is due to low-energy electron precipitation as the plasma returns from the nightside. They mean that the EUV ionization is involved in the process to mainly increase the average plasma densities. MacDougall and Jayachandran [2007] believe the patchy nature of enhancement is caused by the precipitation which occurs during the return flow, and that flow channels and cusp precipitation in the cusp/cleft region will give rise to additional structuring.

The various mechanisms that form the patches are summarized into three families [Moen et al., 2006]:

Transient reconnection Flux transfer events (FTEs) or transient reconnection is a possible structuring mechanism presented by Lockwood and Carlson Jr. [1992]. This process works in the following way. The open closed boundary (OCB) will leap equatorward to a high-density plasma region. It is followed by a relaxation of that boundary, carrying with it the high density plasma into the polar flow. [Carlson et al., 2006] have successfully tested this mechanism.

Plasma depletion Valladares et al. [1998] present another approach where the electron density depletion between patches may be caused by an enhanced plasma recombination rate. This recombination is due to enhanced ion-frictional or joule heating from rapid plasma drift of short-lived east-west flow channels in the cusp region. Related work to this topic is for instance Valladares et al. [1994, 1996]

Changing convection Anderson et al. [1988]; Sojka et al. [1993, 1994] presented a mechanism which responds to changes in the convection pattern, especially in the IMF B_y component. It expands the polar cap to lower latitudes and brings higher-density plasma into the polar cap. The high-density plasma convects under the influence of the convection pattern from the solar-illuminated dayside throat region into the polar cap. To obtain patches instead of a continuous tongue of ionization, the transport needs to be discontinuous and the convection pattern needs to be time dependent. The IMF regulation will cause alternating intake of high and low density plasma [Anderson et al., 1988; Rodger et al., 1994a]. There also exists explanations regarding more localized convection effects. Rodger et al. [1994a] suggest another possible chopping mechanism, that is short-lived convection jets which is linked to flow-channel events, while Schunk et al. [1994] suggest traveling twin-convection vortices.

A polar cap patch can have significant effects on various radar and radio systems, causing degradation in the form of phase advance, time delay, bending, and errors in Doppler shift for many practical RF VHF systems, including many military systems. It also has an effect on ground-to-satellite communication and other navigation and communication systems [Basu et al., 1990]. There are still a lot of unknown factors, and extensive research is going on to predict the occurrence of these patches and make a space weather forecast [Schunk and Sojka, 1996] and [Basu et al., 2002].

During geomagnetic storms, storm enhanced densities (SED) are observed. SED often appear near the poleward edge of the mid-latitude F region as a distinct region of dense plasma [Foster, 1993], see figure (2.18). This region is produced when solar EUV produced ionospheric plasma at middle and low latitudes is picked up by the storm enhanced convection electric field and flows from lower mid-latitudes and into the sub-auroral and polar regions. The SED is related to the sunward convection, and thus the latitude of the SED decreases with increasing local time and increasing disturbance level [Foster et al., 2005].

The Subauroral Polarization Stream (SAPS) is a collective name for all of the Sub-Auroral Electric Fields [Foster and Burke, 2002]. These strong polarization electric fields develop across the sub-auroral ionosphere during disturbed condi-

tions, e.g [Yeh et al., 1991]. Figure (2.18) shows how the SED/TOI forms over the polar cap. The dayside source of the TOI is the plume of storm enhanced density (SED) which is transported towards noon from subauroral latitudes by the SAPS disturbance electric field. The SAPS electric field lies equatorward of the SuperDARN and convection-model field of view in figure (2.18). The plasma travels with the transpolar flow to the nightside where the auroral F region is enhanced by the SED material.

2.10 Previous attempts to track polar cap patches

Bust and Crowley [2007] used data assimilation and models to track patches in the polar cap, see figure (6.3(a)). The Ionospheric Data Assimilation Three-Dimensional (IDA3D) algorithm was used. IDA3D uses several data sources to obtain a global three-dimensional (3-D) specification of the electron density. In addition, the 2-D trajectory analysis code of Crowley et al. [2000] was used, which utilizes high-latitude convection patterns obtained from another assimilation code named Assimilative Mapping of Ionospheric Electrodynamics (AMIE). Neither AMIE or IDA3D can alone provide complete information on the transport of plasma patches, since AMIE doesn't contain any information about electron densities, and IDA3D lacks information about the convection, but the AMIE technique are thought to be reasonably reliable [Bust and Crowley, 2007]. The convection pattern and trajectories will change when changes in the amount of data occur, but according to Bust and Crowley [2007], this effect is generally small. On the other hand, the AMIE model is built on a rather uncertain convection pattern, which may make the tracing procedure a little uncertain. The error will thus accumulate the more backwards in time the integration is made. One of the results from their study is that the TOI originate from various locations at high latitudes (62-63 degrees geographic latitude). The patches were transported along the edges of the convection pattern, and never reached midlatitudes. Their study proposes that patches produced by transport will have an origin which is determined by the latitudinal extent of significant convection. Since significant convection in the AMIE model does not reach to midlatitudes, the patches cannot originate at these latitudes, except under conditions with high magnetic activity. Bust and Crowley [2007] used an integration period in AMIE of 5 hours, which is approximately the time it takes for a patch to convect across the polar cap from the dayside to Svalbard. They focus their analysis on plasma observed by the ESR, but they also investigated the TOI above Quanaq (Greenland).

Chapter 3

Instruments and data sets

The various instruments and data sets used in this thesis are presented below. A key objective is to study the occurrence rate of extreme densities in the polar cap when the F2-peak is larger than $10^{12}m^{-3}$, and to study the intake of patch material in the polar cap using high latitude measurements. Qiu [2006] investigated the diurnal variability of the F2 region peak based on the same data set from the ESR, thus the data he gathered for his work forms the starting point for this thesis. The time delay from ACE to the ionosphere is calculated using two different approaches.

The time scale used for most of the plots is given in Universal Time (UT). Magnetic Local Time (MLT) is a different time system which also is used. MLT refers to the dipole axis, and the longitude is measured in hours fixed relative to the Sun. The magnetic longitude facing the Sun is MLT 12 hours, which is called "Magnetic noon". "Magnetic midnight" is where MLT is 24 hours. Svalbard's Magnetic noon is 08:40 UT, and 24:00 MLT corresponds to 20:40 UT.

3.1 Radar

Radar stands for Radio Detection And Ranging, and it is the main type of instrument to supply data for this thesis. Generally, a radar transmits a pulse or phase coded radio wave and receives a backscatter echo from the target volume. Spectral properties of the backscatter echo can be used to determine physical properties of the target volume. Depending on the process that gives the backscatter and the size of the target, an appropriate frequency is chosen. For radars the most common frequency bands are:

UHF Ultra high frequency in the range 300-1000 MHz, corresponding to wavelength 0.3-1.0 m.

VHF Very high frequency in the range 30-300 MHz, corresponding to wavelength 1.0-10.0 m.

HF High frequency in the range 3-30 MHz, corresponding to wavelength 10.0-100.0 m.

Two types of radars have been used to gather data for this thesis; the incoherent scatter EISCAT Svalbard radar, and the coherent scatter SuperDARN radars. The terms "coherent" and "incoherent" are distinguished by the "coherence time". Coherence is the stability of the medium, i.e how quickly it changes in relation to how quickly the radar resolves those changes. Since all fluids are partly coherent, there exists a "coherence time" (between zero and infinity) for each situation. Radars detecting the thermal fluctuations of a medium, where the coherence time is relatively short have been called incoherent, while the radars using structures within the medium which vary more slowly are called coherent [Hargreaves, 1992]. The EISCAT Svalbard radar and SuperDARN are described in more detail in the following subsections.

3.1.1 EISCAT (European Incoherent Scatter) Radar

EISCAT is an international research organization currently funded and operated by the EISCAT associate countries Norway, Sweden, Finland, Japan, China, the United Kingdom and Germany. EISCAT operates three incoherent scatter radar systems in Northern Scandinavia. All EISCAT radars use the Incoherent Scatter technique to study the ionosphere. Incoherent scatter radars rely on big antenna

Figure 3.1: EISCAT Svalbard radar. The 42m field-aligned antenna to the left and the steerable 32m antenna to the right. Figure from `http://www.scitech.ac.uk/SciProg/Ast/AstDocs/STP_EISCAT.aspx`.

nas and a powerful transmitter, which sends an electromagnetic wave pulse into the ionosphere. When the wave hits the target volume, in our case large numbers of electrons in the ionospheric plasma, the energy is scattered via Thomson scattering [Thomson, 1906] and [Evans, 1969]. This is because the electrons start to oscillate due to the electric field of the transmitted wave. The oscillating electrons will then start to radiate an electromagnetic wave in all directions. A small part of this energy finds its way back to the radar, which now function as a receiver. A weak backscattered signal is detected, and by combining the signal from multiple pulses at different time delays a complex function called the Autocorrelation Function (ACF) can be estimated [Beynon and Williams,

1978]. These functions can be used to determine the Doppler power spectrum, which in the incoherent scatter case is called a double-peaked ion-line spectrum. It is quite broad and the shape depends on for instance the electron and ion temperatures and the composition of the plasma, see figure (3.2). This figure shows the double-peaked ion-line and the two plasma lines. From the power spectrum, assuming a Maxwellian distribution and by the use of signal processing, the line-of-sight Doppler shift can be measured very accurately. The total

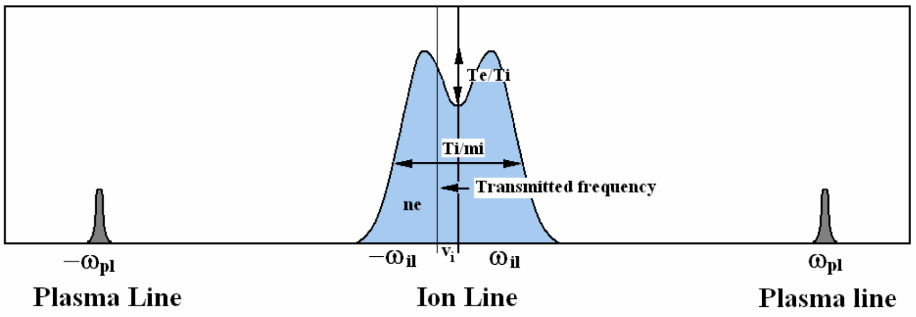

Figure 3.2: A Doppler power spectrum showing the two plasma lines and the double-peaked ion-line. The received power is a function of frequency. The width of the spectrum depends on the relation of the ion temperature to the ion mass ($\frac{T_i}{m_i}$). The relation of $\frac{T_e}{T_i}$ is given by the height of the "shoulders" above the "valley", and thus the "sharpness" of the ion lines depends on this ratio. v_i is the ion drift velocity, and the area of the ion-line power spectrum gives an estimate of the ionospheric electron density, n_e. Figure from Rinne [2006].

returned power depends on the number of electrons. The area of the ion-line power spectrum is proportional to the number of electrons in the backscatter volume and gives an estimate of the ionospheric electron density. The width of the spectrum depends on the ratio of the ion temperature to the ion mass, and the overall Doppler shift of the spectrum corresponds to the bulk motion of the ions. The depth of the "valley" to the height of the "shoulders" correspond to the ratio between the electron temperature and the ion temperature. For more theory about incoherent scatter, see Beynon and Williams [1978].

The system used in this thesis is the EISCAT Svalbard Radar, which is termed the ESR, see figure (3.1). The ESR gives a special opportunity to study the cusp/cleft region of the ionosphere due to Svalbards ideal location relative to the daytime auroral zone [Wannberg et al., 1997]. It is a UHF system with two mono static antennas. The ESR is located near Longyearbyen (Svalbard) at a geographic latitude of 78.15° and a longitude of 16.03°. The 42 m antenna is fixed along the local magnetic field line, and the 32 m parabolic dish antenna is fully steerable. The dish can operate from −270° to 270° in azimuth and from 30° to 150° in elevation. However, for this thesis, only data obtained with the 42m antenna is used. The 42m antenna is aligned at 81.6° elevation and 181.0° azimuth. The transmitter has a central operating frequency of 500 MHz [Wannberg et al., 1997]. For mono static radars, like the ESR, the same antenna both transmits and receives the signal.

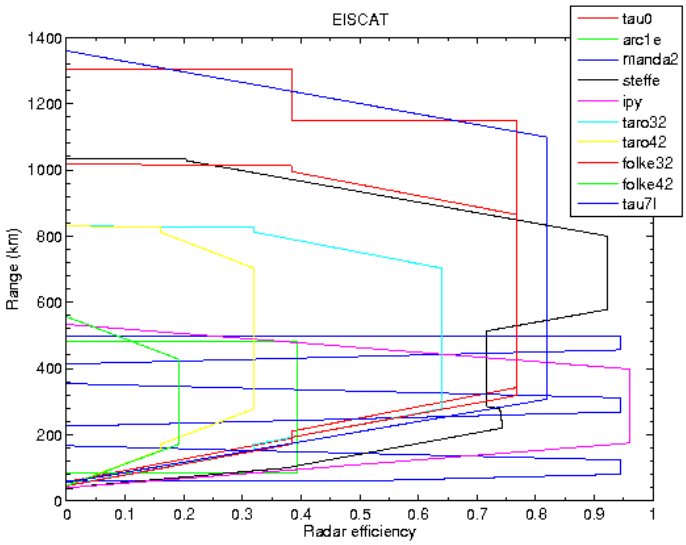

Figure 3.3: Pulse code efficiency as a function of range for various experiments performed by EISCAT. Figure from EISCAT Scientific Association.

There are different types of pulse code experiments to run, depending on which altitude you plan to investigate. For the ESR, the most efficient experiments are shown in figure (3.3). Due to the fact that tau0 covers a large range from approximately 60 to 1300 km, the tau0-experiment was used to collect data for this thesis. It provides superb opportunities to study the F-layer ionosphere over Svalbard. Tau0 uses two alternating pulse codes of $960\mu s$, with a 50 km coded pulse length. The x-axis shows the radar efficiency which is a measure of the available lags at a given range. Radar efficiency 0 means that no lags of the ACF is available, while radar efficiency 1 means that all lags are available at that range. Figure (3.3) shows that tau0 optimizes in the range from $\sim$ 350km up to $\sim$ 1150km.

The data for this thesis is based on measurements from the long data runs in February 2001 and October 2002. The raw data obtained from ESR are stored at the EISCAT headquarter in Kiruna. From there, it is distributed to different institutions around the world. The analyzed data used in this thesis were downloaded from the Rutherford Appleton Laboratory (RAL) in England, which is part of the UK EISCAT support group. The time resolution is 2 minutes, and the spatial resolution is 3km between 90 and 150km altitude, 6km from 150 to 220km, 12km from 220 to 350km and 36km above 350km [Moen et al., 2008]. Figure (3.4) shows a typical summary plot of the ESR data. It shows the altitude profiles of the electron density (N_e), the electron temperature (T_e), the ion temperature (T_i) and the ion velocity (V_i) on 07 February 2001. The data are downloaded from `http://www.eiscat.se/raw/schedule/schedule.cgi` and shows the parameters in 24 hour segments. The data from this day is discussed further

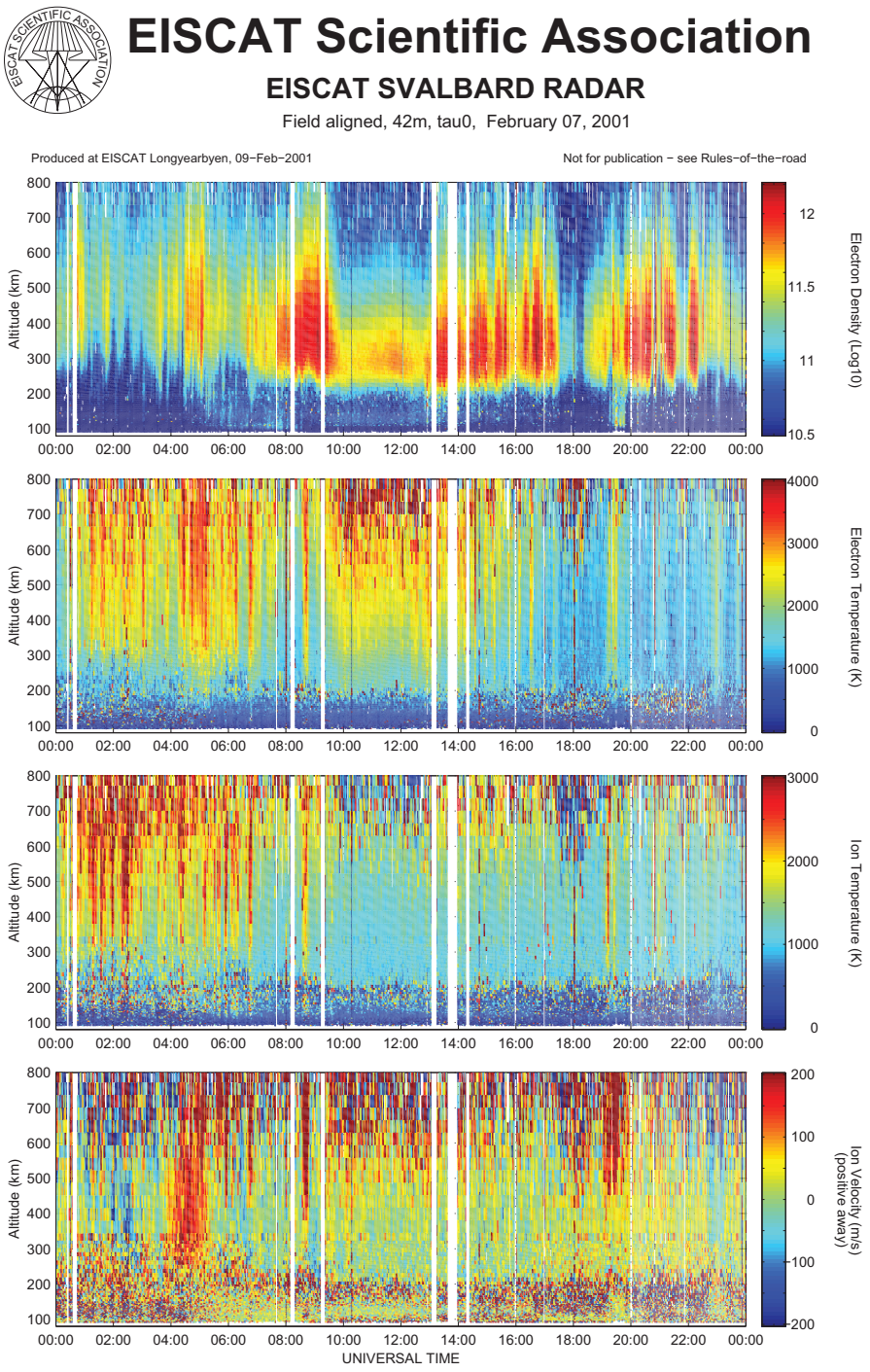

Figure 3.4: Altitude profiles of the electron density distribution (N_E), the electron and ion temperature (T_e, T_i), and the line of sight ion velocity (V_i) on 07 February 2001. The second panel shows a temperature drop during the long duration events. The white area show a data gap due to an airplane interruption which last for approximately 10 minutes. The figure is downloaded from `http://www.eiscat.se/raw/schedule/schedule.cgi`.

in section (4.1).

Some of the data collected by the radar could not be used due to their extreme and unrealistic high values. These values probably come from clutter due to satellite passes, noise or errors in the analysis. The solution to this problem is to ignore data values of the electron density which exceed $5 \cdot 10^{12} m^{-3}$. The height of particular interest is 250-600 km, so the data above and below this height is also ignored. After removing useless days from the two months examined, the October data turned out to consist of 27 days with 24 hours of continuous measurements at a stable activity level, while the data from February consists of 20 days with 24 hours of continuous data. The maximum of the 23 sunspot cycle was reached in 2001, see figure (2.2). Further, the extreme density values were listed according to their duration, see chapter 4.

3.1.2 SuperDARN (Super Dual Auroral Radar Network)

A coherent scatter radar is designed to receive echoes from physical structures within an ionized medium. The most ionospheric electron-density structure is produced by plasma instability processes, [Fejer and Kelley, 1980] and [Fejer and Providakes, 1987]. A short sequence of pulses known as multi pulses is transmitted in the HF band and thereafter the returning echoes are sampled. The coherent scatter radars are sensitive to Bragg scattering from small-scale ionospheric irregularities in the electron density which are aligned along the magnetic field with a spatial Fourier component [Greenwald et al., 1995]. A radar which detects backscatter is sensitive to ionospheric irregularities having a wavelength equal to one-half of the radar wavelength. The irregularities act as tracers of the ionospheric convection, since the irregularities drift with the background plasma motion in the F region [Greenwald et al., 1995; Milan et al., 1998].

Figure (3.6) shows the E and F-regions of the ionosphere. The nearly vertical magnetic field lines at high latitudes lead to non-orthogonal scattering at VHF and higher frequencies. The scattered signals propagate into space and the backscatter signal will return to the radar if the signals are propagating perpendicular to the magnetic field when they encounter regions of ionospheric irregularities [Greenwald et al., 1995]. By observing the drift of small-scale irregularities in the F-region, the convection velocity can be measured [Ruohoniemi et al., 1987]. Backscatter is detected from ionization irregularities in the ionosphere that have been amplified far above the thermal fluctuation level by plasma instability processes. This backscatter provides a Doppler power spectrum after some processing. The parameters that can be derived are the backscatter power, the mean Doppler velocity, and the spectral width.

SuperDARN is a network of high frequency (HF) radars which are distributed in the northern- and southern hemispheres [Greenwald et al., 1995]. In total 18 radars (2007) contributes to this network, where 11 are located in the northern hemisphere, and the rest is situated in the southern hemisphere [Chisham et al., 2007]. Figure 3.5 shows a map of the fields of view of the SuperDARN radars in both hemispheres. The fields of view are mainly oriented toward the geomagnetic pole, with the exceptions of the Iceland radars which are directed more

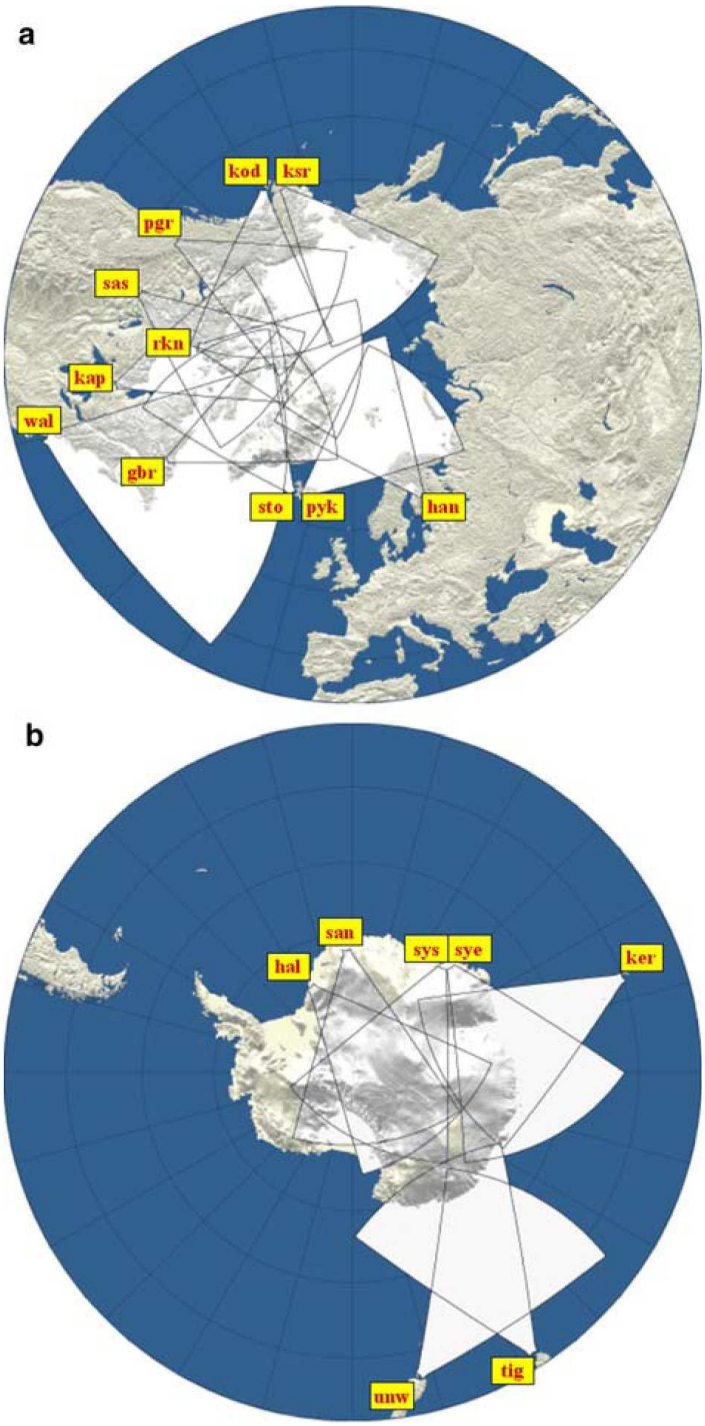

Figure 3.5: Field of view of the SuperDARN radars in the northern hemisphere (a) and the southern hemisphere (b). The three-character code name of each radar is shown close to each radar location. Figure taken from Chisham et al. [2007].

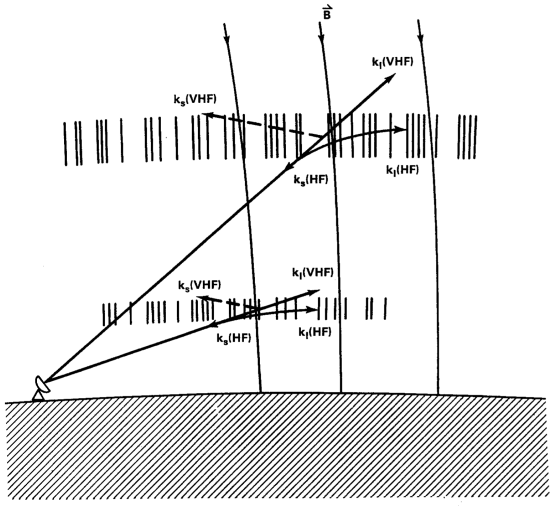

Figure 3.6: VHF and higher frequencies are scattered into space by high-latitude electron density irregularities. As the HF signals enters the ionospheric layers, they are refracted toward the horizontal. Figure taken from Greenwald et al. [1995].

zonal. All radar fields of view overlap with at least one other radar, giving the opportunity to measure ion flow vectors over a large area. The SuperDARN radars operate between 8 and 20 MHz in the HF band, and they usually sweep through scans in azimuth every 1 or 2 minutes. The spatial resolution is typically 50 km $\times$ 100 km [Ruohoniemi et al., 1987]. The SuperDARN radars can transmit pulses from 100μs up to several thousands μs, but a typical pulse length is 300μs which corresponds to 45 km range resolution. Multi pulse transmission sequences of 5 to 9 pulses are typically used. This sequence of pulses are repeated several times for each beam position to give as little noise as possible. A number of beam directions (typically 16) are possible, due to the radar beam being steerable [Chisham et al., 2007; Baker et al., 2007].

The SuperDARN network measures the $\vec{E} \times \vec{B}$ drift of the plasma over large areas of the high-latitude ionosphere under changing IMF conditions. Except for outages due to equipment malfunction or repair work, these radars operate continuously. By transferring data from the radars over Internet links, a real time convection map has been developed. Real-time data from SuperDARN is available at the Johns Hopkins University Applied Physics Laboratory (JHU/APL) SuperDARN website http://superdarn.jhuapl.edu/.he web page contains the real time convection map, and a value for the IMF, that is determined by finding the best match between the measurements and the various patterns of the model. The total polar cap potential variation is also put out on the webpage. The typical delay between the current time and the plot time is 5 minutes [Ruohoniemi and Baker, 1998]. Almost every study about patch formation relies on high-latitude convection to transport ionospheric plasma from the dayside of the polar cap toward the nightside. Thus, supporting data were

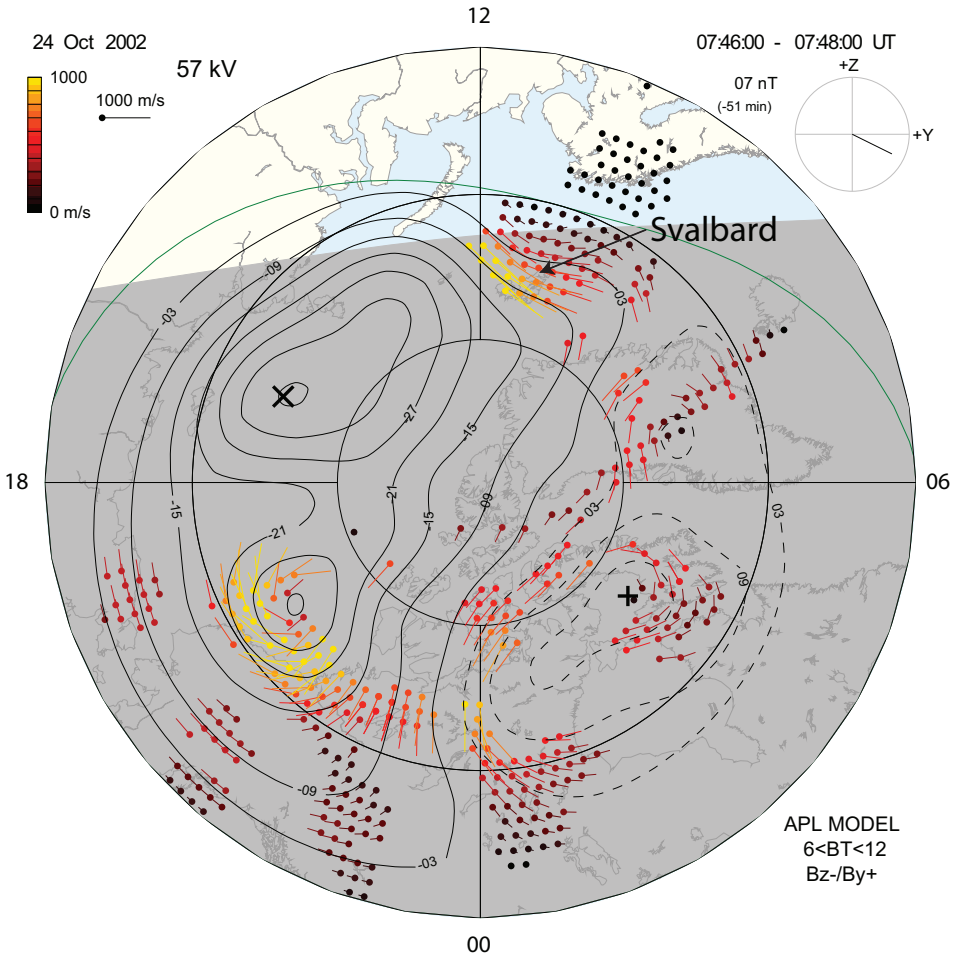

Figure 3.7: SuperDARN convection map between 07:46 UT and 07:48 UT on 24 October 2002. The map is given in a MLT grid with noon on top, morning to the right, midnight on the bottom, and evening to the left. Latitude circles are at 10° intervals, with the magnetic pole in the center and 60° magnetic latitude on the outer circle. The figure shows the potential contours of the convection pattern together with its fitted velocity vectors. The center of the dusk (negative) cell is labeled X, while the center of the dawn (positive) potential cell is indicated by $+$. Some of the dark dots are backscatter, while the velocity vectors are given with color, length and direction. A color bar is shown on the top left to indicate the velocity. The solar terminator is also shown with grey shading. On the top right the IMF is shown. Here IMF B_y is positive, while IMF B_z is negative. Svalbard is indicated on the map.

necessary to locate the possible origin of the patches. SuperDARN data was therefore studied for February 2001 and October 2002 as well. The convection maps downloaded from the webpage were first used to check for HF backscatter radar data. However, these 10-min data were only sufficient to investigate the coverage above Svalbard. SuperDARN data with 2-min time resolution were therefore used in the further analysis. The raw data were provided by Mike Ruohoniemi at Virginia Tech, and the global convection data were compiled by Kjellmar Oksavik using the solar wind lag I requested using the simple approach method, see figure (3.10). One of these convection maps are shown in figure (3.7). It shows the coverage of real SuperDARN data in the northern hemisphere on 24 October 2002 in the period between 07:46 UT and 07:48 UT. The SuperDARN coverage is good in a limited area over and to the south of Svalbard. Svalbards position is indicated with an arrow on the map. The velocity vectors are given in color, length and direction, while the dark dots are backscatter. The solar terminator is shown with grey shading.

3.1.3 SuperDARN data structure

The primary objective of SuperDARN is to provide continuous and global-scale observations of high-latitude ionospheric convection. Ruohoniemi and Baker [1998] developed a new method for deriving large-scale convection maps based on all available SuperDARN Doppler data within a hemisphere. This analysis has been further developed by Shepherd and Ruohoniemi [2000]. First, all Doppler velocity data are median filtered in range, azimuth, and time to remove noise and marginal values. The filtered data are then mapped onto a uniform spatial polar grid of equal area cells. The measurements are then used to determine a solution for the distribution of the electrostatic potential, Φ. The solution is expressed as a series expansion in spherical harmonics,Y_{lm}, (e.g Jackson [1962]):

$$\Phi(\theta,\phi) = \sum_{l=0}^{L} \sum_{m=-M}^{M} A_{lm} Y_{lm}(\theta,\phi) \tag{3.1}$$

where A_{lm} are complex-valued coefficients, L is the order of the expansion, and M is the degree of the expansion. $M \leq L$. The large-scale electric field is related to the electrostatic potential by

$$\vec{E} = -\nabla\Phi \tag{3.2}$$

and this $\vec{E}$ field drives the plasma convection according to:

$$\vec{v} = \frac{\vec{E} \times \vec{B}}{B^2} \tag{3.3}$$

Some selection of fitting criteria is required, including the order of expansion and the low-latitude limit of the convective zone where the electrostatic potential is set to zero. In regions with no data coverage, additional data from a statistical model is used to give the solution. The global convection is often effectively determined by a low-order fitting of the electrostatic potential, provided the measurements are sufficiently widespread [Ruohoniemi and Baker, 1998; Shepherd and Ruohoniemi, 2000].

A Heppner-Maynard (HM) boundary is determined by identifying the latitude at which it crosses magnetic midnight. For a more detailed description, see Greenwald et al. [1995] and Chisham et al. [2007].

3.2 Advanced Composition Explorer (ACE)

For this thesis the Advanced Composition Explorer (ACE) is used to collect data from the solar wind. The ACE satellite was designed and developed by many organizations and individuals under the support of the Explorer Program at the NASA Office of Space Science. On 25 August 1997, the satellite was successfully launched into space from the Kennedy Space Center in Florida.

The spacecraft varies its position, but it is most often located near the L1

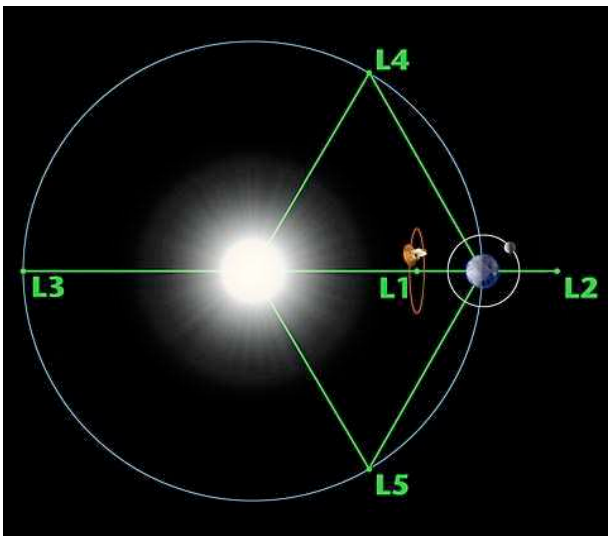

Figure 3.8: The ACE spacecraft is located at the Lagrangian point L1, with the Sun to the left, and the earth to the right, and with the moon rotating around the earth. Figure from `http://www.matessa.org/~mike/l1.html`.

Lagrangian point, which is around $240R_E$ sunward of the Earth, see figure (3.8) [Stone et al., 1998].

The Lagrangian point is named after the Italian-French mathematician Joseph Louis Lagrange who pointed out that in a three body system which is circular and consisting of two massive bodies orbiting around a common center of mass and one body of negligible mass, there are together five stationary solutions. All of these solutions represent positions in space, like the L1 Lagrangian point where ACE is located. In this case, the two massive bodies are respectively the Sun and the Earth. At these Lagrangian points the gravitational fields between the Sun and the Earth are in equilibrium. The third body, the satellite will be stationary when put in any of these positions. The first three positions, named L1, L2, and L3, are only stable solutions in the plane perpendicular to the Sun-Earth line, but when using a halo orbit, like in the case for ACE, the

orbit around these points will be stable as well.

The primary mission of the Advanced Composition Explorer is to measure the composition and abundances of energetic particles coming from the Sun, the heliosphere, and the Galaxy beyond. When orbiting around the L1 Lagrangian point, ACE will also be able to provide a space weather forecast for the Earth approximately one hour in advance.

ACE contains nine instruments, eight of them measuring the plasma and energetic particle composition and one instrument measuring the interplanetary magnetic field (IMF). Only data from two of the nine instruments are used in this thesis; a magnetometer (MAG) which measures interplanetary magnetic field parameters, and a Solar Wind Electron, Proton and Alpha Monitor (SWEPAM) which measures solar wind parameters. A brief description of the two instruments follows.

SWEPAM measures the solar wind electron and ion fluxes as functions of direction and energy. From these data detailed information about the solar wind conditions is available every minute. These data can also be used for space weather monitoring purposes, when real-time solar wind observations continuously are sent to the ground. There are two separate sensors for measuring electrons and ions. The ion sensor measures particle energies between 0.26 KeV and 36 KeV, while the electron sensor measures energies between 1 eV and 1350 eV. Both sensors use electrostatic analyzers, where the fields-of-view are fan-shaped. These analyzers measure the energy per charge of each particle by bending their flight paths through the system. The fields-of-view are swept across all solar wind directions by the spin rotation of the spacecraft. For further information about SWEPAM, see McComas et al. [1998].
MAG consists of a twin vector flux gate magnetometer controlled by a common CPU. The sensors are mounted approximately 4.19 meters from the center of the spacecraft and are put on opposite sides of the spacecraft along the +/-Y axes. The reason for this is to reduce any disturbances from magnetic fields from the spacecraft and its sensors. Six magnetic field vector measurements are returned each second, divided between the two sensors and all three axes (x, y and z) of the magnetic field. For further information about MAG, see Smith et al. [1998].

The lifetime of ACE is expected until 2019, depending on the amount of propellant on board and details of the orbit. For more information about the ACE spacecraft, see Stone et al. [1998].

3.3 The WIND Satellite

The WIND satellite is used to collect data of the solar wind velocity for the special case on 06 February 2001, see section (3.4.1). It was launched by NASA on 1 November 1994. WIND is the first of two spacecrafts in the Global Geospace Science initiative, which is part of the International Solar-Terrestrial Physics (ISTP) Initiative. ISTP is a collaboration between several countries in Europe, Asia, and North America. The aim is to understand the physics of the behavior

of the solar-terrestrial system in order to predict how the Earth's atmosphere will respond to changes in solar wind. The WIND satellite was first supposed to be positioned near the Lagrangian point L1, see section (3.2). However, both ACE and SOHO are located there, so WIND's orbit was later changed to a more complicated orbit. The spacecraft could then perform measurements from different parts of the space around the Earth, with the advantage of a broader coverage of the solar wind. WIND carries nine scientific instruments to continuously monitor the solar wind near Earth. Data from the SWE instrument (The

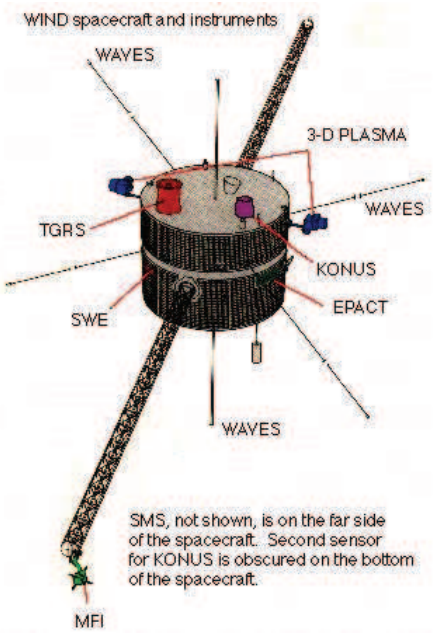

Figure 3.9: The WIND spacecraft with its nine instruments. Figure from `http://www-spof.gsfc.nasa.gov/istp/wind/`.

Solar Wind Experiment) have been used in this thesis. SWE measures ions and electrons in the solar wind. The solar wind velocity, density, temperature and heat flux can be deduced. The aim is to study the solar wind with its fluctuations and the interaction of the solar wind with the magnetospheric system. For more information about the SWE instrument, see Ogilvie et al. [1995]

3.4 Solar wind data

The solar wind data were investigated to see if there were changes and possible repeating patterns in the IMF components during the extreme density events. Level 2 (processed) ACE data were downloaded from
`http://www.srl.caltech.edu/ACE/ASC/level2/index.html` , where merged 64-second IMF and Solar Wind Averages data from the instruments SWEPAM and MAG were used. These data have been converted into the GSM coordinate system. The Wind data is downloaded from
`http://cdaweb.gsfc.nasa.gov/cgi-bin/eval1.cgi` , where the key parame-

ters from the SWE instrument are used.

3.4.1 Calculating the time delay

The calculations of the time delay are described in this section for 24 October 2002. The Matlab program *Solarwind24102002.m* is included in Appendix B, and it performs the calculations described below. It was not possible to use ACE solar wind data for 06 February 2001, since no solar wind speed was available for this day. The WIND satellite was therefore used instead. The programme *Solarwind06022001.m* performs the calculations for this day.

The ACE satellite and the WIND satellite was located approximately at $X_{GSM} = 240R_E$ and $X_{GSM} = 38R_E$, respectively. Due to the distance between the spacecraft and the ionosphere, the measurements need to be time shifted when we want to figure out the solar wind conditions that impacted the magnetosphere-ionosphere system at a given time. The time shift is also needed when we want to insert the right IMF conditions into the SuperDARN map-potential model to produce convection maps. Several models exists for calculating the time delay, for instance the Lockwood method (Lockwood et al. [1989]) and the Shue et al. method (Shue et al. [1998]). Moen et al. [1999] made use of a model which uses the phase plane orientation in proportion to solar wind propagation. This model takes into account the distance from the bowshock to the magnetopause as well.
A key parameter in space physics is the location of the magnetopause. Since it separates the magneospheric plasma from the solar wind, it determines the size of the magnetosphere and the location where the solar wind reconnects with the terrestrial magnetic field. Different models to find the magnetopause location under various solar wind conditions exist. In early models, the location solely depended upon the solar wind dynamic pressure (D_p), but later studies found the IMF orientation to have an influence as well [Shue et al., 1998].

Two different models for calculating the time delay from ACE and WIND to the ionosphere are considered below, but the simple approach method will be used in the further analysis.

The Shue et al. model

The Shue et al. [1998] model can account for both an open and a closed magnetosphere. It is valid for $-18nT < IMFB_z < 15nT$ and solar wind dynamic pressure $0.5nPa < D_p < 8.5nPa$. The distance along the X_{gsm} axis is divided by the radial component of the solar wind speed, ignoring any effects of the bow shock or magnetic structures in the Y_{gsm} direction. For this calculation, structures in the solar wind are assumed to move with the solar wind speed all the way from the spacecraft to the magnetopause. This method ignores the actual size of the magnetosphere and the distance between the magnetopause and the ionosphere. Instead an additional fixed 6 min delay is added in the end of the calculations to take into account the propagation time from the magnetopause to the F-layer ionosphere [Moen et al., 2004]. For more theory, see Shue et al. [1998].

The time shift is calculated using the following formula:

$$\Delta t = \frac{X_{GSM} - r_0}{V_x} \tag{3.4}$$

V_x is the solar wind speed along the sun-earth line, X_{GSM} is the x-component of the satellite position in GSM coordinates, and r_0 is the magnetopause stand-off distance at the subsolar point. The latter is calculated using the empirical model by Shue et al. (1998) and the parameters IMF B_z and the solar wind dynamic pressure D_p:

$$r_0 = [10.22 + 1.29\tanh(0.184(B_z + 8.14))]{D_p}^{-\frac{1}{6.6}}[R_E] \tag{3.5}$$

$$D_p = N_p m_p (V_x)^2 \cdot 10^{21}[nPa] \tag{3.6}$$

As an example, measurements from the dataset on 24 October 2002 are used with the following input parameters:

- $m_p = 1.672621637 \cdot 10^{-27} kg$
- $N_p = 13.048 cm^{-3}$
- $V_x = -446.79 \frac{km}{s}$
- $B_z = -9.023 nT$
- $X_{GSM} = 1.4223 \cdot 10^6 km$

The solar wind pressure is given by equation (3.6), resulting in $D_p \approx 4.36$ nPa. Equation (3.5), gives $r_0 = 8.0101 R_E \approx 51089.52$ km, since $1 R_E = 6378.137$ km. Equation (3.4) then gives a time delay of $\Delta t = 3069.03$ s ≈ 51 minutes.
The total estimated time delay from ACE to the ionosphere is therefore 57 minutes, after the fixed 6 minutes from the magnetopause to the ionosphere have been added.

The simple approach method

The Shue et al. [1998] model doesn't take into account the actual distance from the magnetopause to the ionosphere and the fact that the magnetosphere has a varying size. The simple approach method eliminates the calculation of r_0, and is given by:

$$\Delta t = \frac{X_{GSM}}{V_x} \tag{3.7}$$

By using the same parameters given above, equation (3.7) gives us a time delay of $\Delta t = 3183,37$s ≈ 53 minutes. Figure (3.10) shows that the two models differ by less than 4 minutes. This is a satisfactory result, since there are several uncertain factors in this calculation, like the distance from the magnetopause to the ionosphere, solar wind speed variations, and potential variations in IMF. The difference between the two models is the calculation of the bowshock. The simple approach does not consider that the solar wind slows down after passing the bowshock, and the difference is therefore fairly constant. It should also

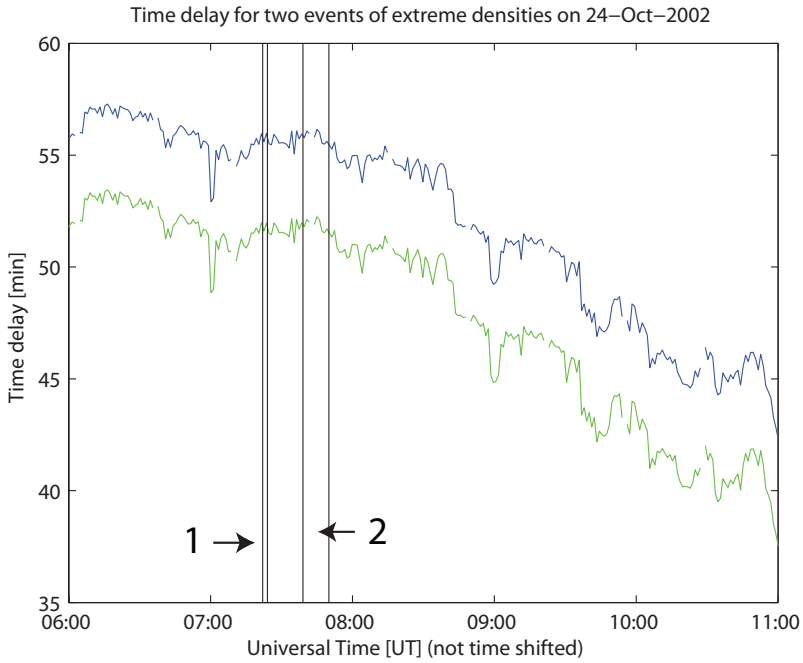

Figure 3.10: Time delay calculated by the Shue et al. method (blue line) and the simple approach method (green line). The two events show approximately the same time delay. The black vertical lines indicate the time of the two events at ACE.

be pointed out that 4-min is acceptable, when the SuperDARN data is only 2-min resolution. In figure (3.10) the delays vary between 40 minutes and 60 minutes from 06:00 UT until 11:00 UT on October 24 2002. The time delay for the Shue et al. method is shown as the blue line, while the simple approach method used in the remainder of this thesis is shown in green. Due to the large fluctuation in the time delays throughout the interval studied, the lags are calculated separately for the events. All events occur before 08:15 UT, so the lag vary between 50 and 60 minutes for the extreme density events. From figure (3.10) we find that event 1 and event 2 have approximately 52 minutes time delay. This is found by taking the average time-delay during each event. The duration of the two events are indicated with black vertical lines, labeled 1 and 2. Figure (3.11) shows the time shifted data from the ACE satellite on 24 October 2002 during the time interval 06:00 UT to 11:00 UT. The IMF components are shown in the three upper panels, and the solar wind velocity and the proton density are displayed in the lower most plots. The time interval of interest in this thesis is the events indicated in figure (5.14).

Special case on 06 February 2001

There exist no solar wind velocity data from the ACE satellite on the 06 February 2001. Additional data from the WIND satellite was therefore needed to calculate the time delay for this particular day. The velocity data from WIND turned out to be rather stable in the time interval of interest, see uppermost panel in figure (3.12). A constant value of the velocity was thus considered good enough to represent the solar wind velocity at ACEs location. The median of the maximum and minimum velocity was therefore used in the time delay calculation, using the simple approach method presented in the previous section. The satellite is located approximately $38R_E$ behind the Earth in the x-direction, and approximately $160R_E$ in the positive y-direction at 07:00 UT on this day. The IMF data from the WIND satellite are thus not used in the calculation because WIND is located far away from the Sun-Earth line, and in that case the calculation of the time delay would need a more extensive method. The median velocity is $Vx = -382,3$ km/s, which gives a lag of 67 minutes with the simple method approach. The time delay when using the maximum velocity of the solar wind is 58 minutes, and 75 minutes when using the minimum velocity of the solar wind. This 8-9 minutes difference from the median value will not make any difference with respect to the polarity of IMF B_y and B_z, so the median value with its 67 minutes delay was used in the calculations. The result of the time shifted ACE data is shown in figure (3.13). The time interval of interest in this thesis is the events indicated in figure (5.3).

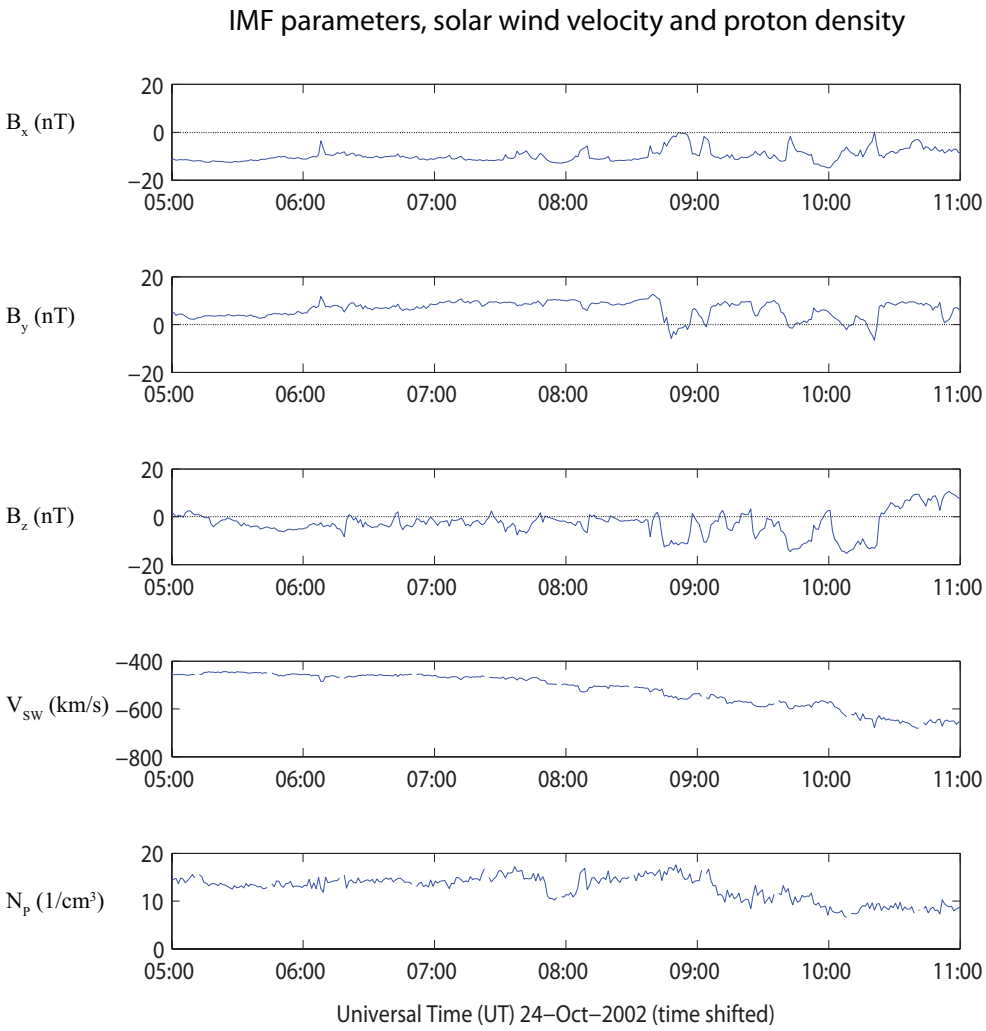

Figure 3.11: The Interplanetary Magnetic field (B_x, B_y and B_z), solar wind velocity (v_{sw}) and proton density (N_p) measured by the ACE satellite at the L1 Lagrange point between 06:00 - 11:00 UT (the data in the figure is time shifted using 52 minutes lag).

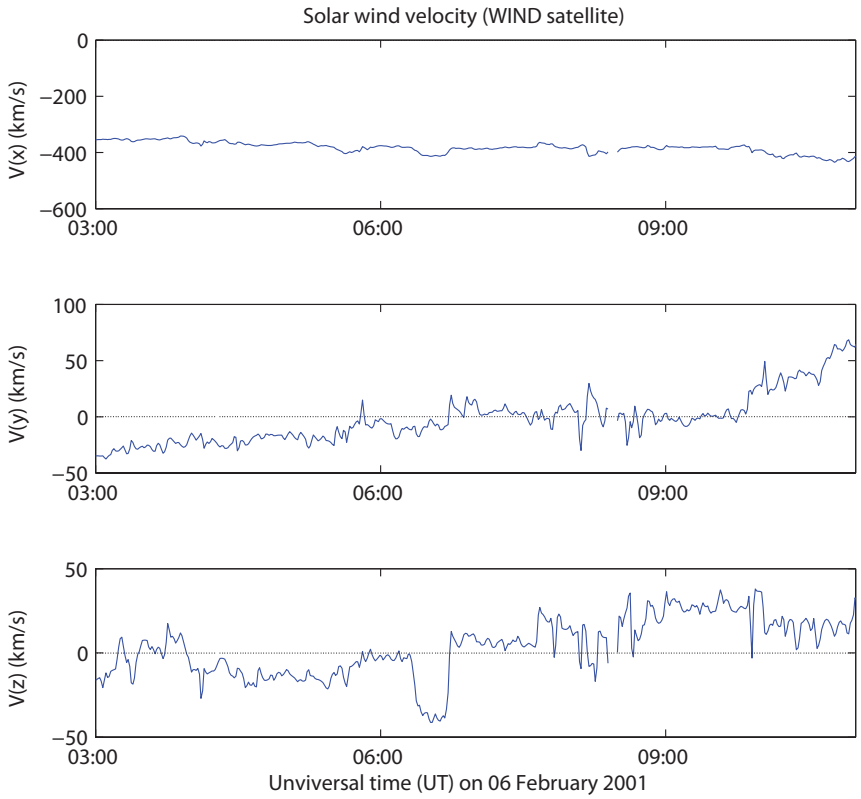

Figure 3.12: The solar wind velocity measured by the WIND spacecraft for 06 February 2001. The uppermost panel shows the velocity component in the x-direction, which indicates a rather stable situation in the time period of interest.

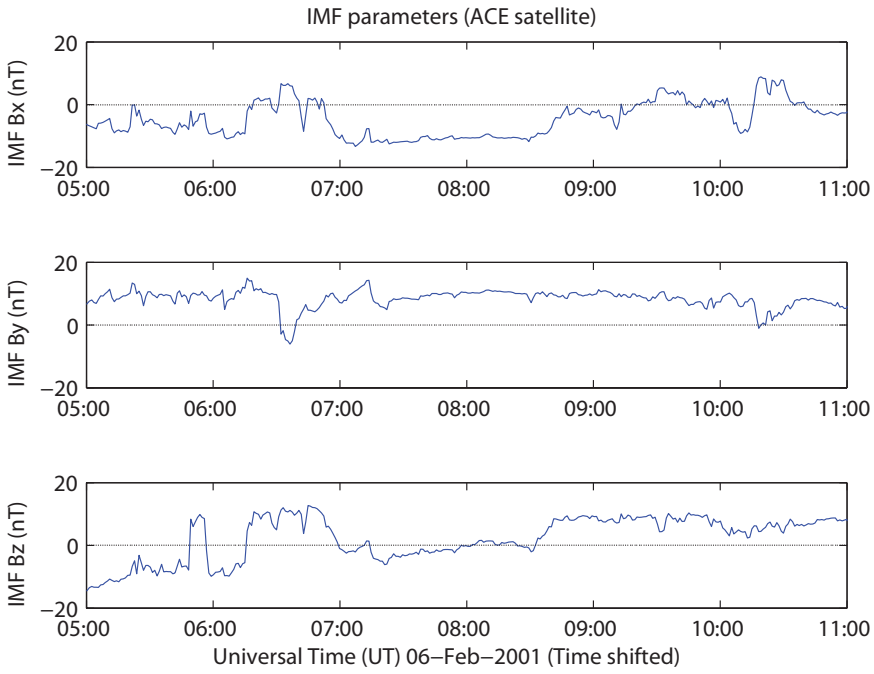

Figure 3.13: The interplanetary magnetic field measured by the ACE spacecraft for 06 February 2001. The uppermost panel shows IMF B_x component, the middle panel shows the IMF B_y component, while the lower most panel shows the IMF B_z component.

Chapter 4

Method and observations

This chapter focuses on the methods used to analyze the data presented in the previous chapter. First, the EISCAT Svalbard Radar (ESR) data is checked for enhanced plasma densities $> 10^{12}m^{-3}$ occurring in the F_2 region above the radar. The altitude range is 250-600 km. Every day in the dataset from 2001 and almost 60% of the days from 2002 contained extreme density events. To provide a sufficient workload six days of good data coverage were chosen, which again was reduced to two days with respect to the most reliable results of the tracing. The reasons for picking out these cases are described below. Possible sources of the density enhancements are further investigated by tracing the high electron densities detected by the ESR backwards in time to their potential source region. A description of the method used to perform this tracing and the geometry behind is given below. The Matlab program codes can be found in appendix B. Short explanations are given as comments within the codes.

4.1 Occurrences of extreme densities

The main objective of this thesis is to address the source of extreme F_2 region electron densities in the polar cap, and electron density data collected by the ESR along the magnetic field was therefore reviewed for values exceeding $10^{12}m^{-3}$. All together this was 20 days from February 2001 and 27 days from October 2002. Due to the findings of Qiu [2006], the period when Svalbard is close to magnetic noon is of particular interest. He showed that extreme density maxima, known as F2 peaks, were found to occur around magnetic noon ($\sim$ 09 UT $\approx$ 12 MLT) and magnetic midnight ($\sim$ 21 UT $\approx$ 24 MLT), see figure (4.1). That result is consistent with the solar wind controlled transport of EUV ionized plasma from day to night across the polar cap [Foster et al., 2005].
Figure (4.1) shows the October 2002 data plotted as 30 minutes averages. The top panel shows how the density ($NeF2_{max}$) varies through a whole day of continuous measurements. It reveals, as mentioned above, two distinct peaks of the average density maxima, one near noon and one near midnight. The variation of plasma density in the F2-region above Svalbard was found to be dominated by transport rather than local production [Qiu, 2006].
The panel in the middle shows the relative distribution of extreme densities that occurred throughout the same day. Qiu [2006] found that the extreme densities

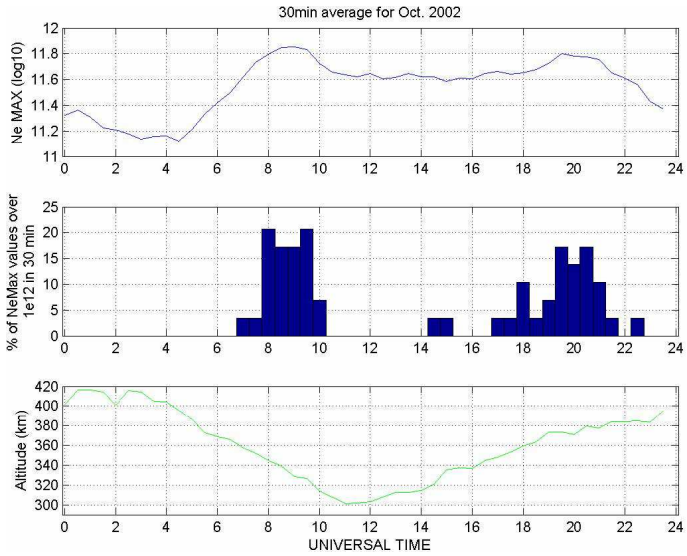

Figure 4.1: Daily behavior of ionospheric parameters $NeF2_{max}$, occurrence of $NeF2_{max}$ greater than $10^{12}m^{-3}$ and $h(_{NeF2_{MAX}})$ based on 30-min averages in October 2002. Figure from Qiu [2006].

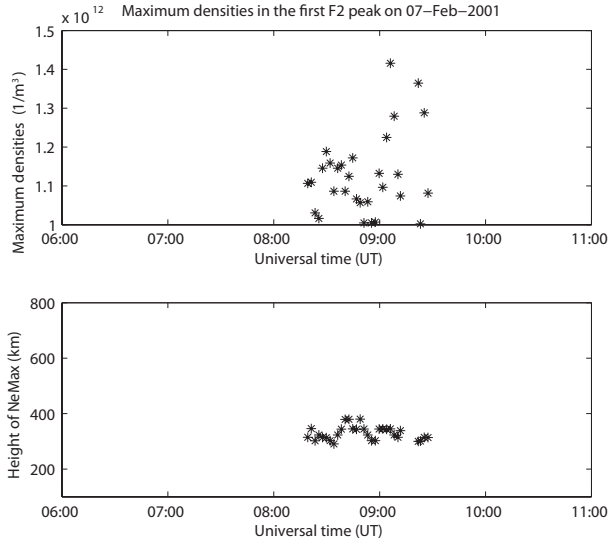

Figure 4.2: Example of extreme electron densities on 07 February 2001. The uppermost figure shows the maximum value of the electron density in the F-region as a function of time. The time of interest is 06:00 UT to 11:00 UT. The lowest figure shows the height of the maximum electron density as a function of time.

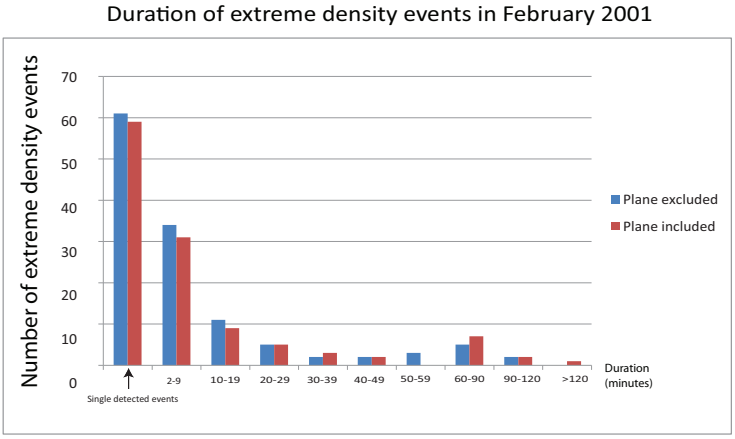

Figure 4.3: Distribution of extreme density events in February 2001. The events are binned according to their duration in minutes. The single detected events represent one detection of an extreme density, i.e one data dump lasting maximum 2 minutes. Events which include airplane interruptions are shown in red, and data where airplane interruptions have been removed from the analysis are shown in blue.

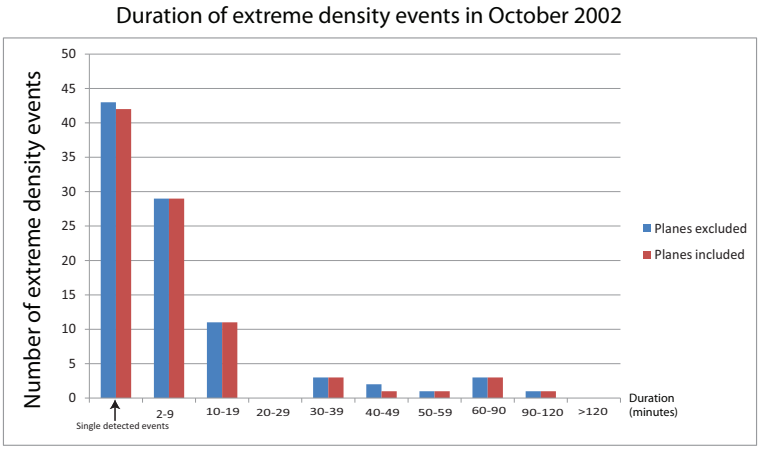

Figure 4.4: Distribution of extreme density events in October 2002. The events are binned according to their duration in minutes. The single detected events represent one detection of an extreme density, i.e one data dump lasting maximum 2 minutes. Events which include airplane interruptions are shown in red, and data where airplane interruptions have been removed from the analysis are shown in blue.

seem to appear at approximately the same time every day.
The bottom panel shows the altitude of the peak density measured in kilometer (km). The typical altitudes of the observed peaks were found to be between ~ 300 and ~ 400 km.
In this thesis the hours between 06:00 UT to 11:00 UT are chosen to be studied in greater detail since the ESR is located near the cusp inflow region during this time interval.

The 2001 and 2002 data contain days with data gaps caused by air traffic which normally last for 10-25 minutes. The gaps occur when the radar is temporary being switched off as an airplane pass over the radar, or there is an airplane in the vicinity off the radar beam. During a data gap, it is impossible to know if the extreme density is still present or if the electron density decreases to below the extreme density limit. The statistical effect of these data gaps can be shown in figure (4.3) and figure (4.4). The red columns show the effect when data gaps due to airplanes are ignored, which means that it is assumed that the extreme densities are continuous through any data gap. The blue columns show the situation where the data gaps have been removed, which means that the high densities are not assumed to be continuous through the datagaps. The consequence is that a continuous event found when data gaps are ignored (red column), is now split up into 2 shorter events (blue column). However, the result is not very different from each other, since the incidents of airplane interruptions are few. Airplane interruptions will only effect the statistics of the long duration extreme density events, and since the short duration events contribute to the largest part of the statistics, these interruptions are not of great significance for the statistics. However, it will effect case studies containing events with such data gaps.

Figure (4.2) show a typical day where extreme densities occur around magnetic noon and the altitude is between ~ 300 and ~ 400 km, consistent with the findings of Qiu [2006]. The first extreme density is detected by the ESR radar at 08:19 UT and the last one is detected at 09:27 UT. A 10-minutes data gap due to airplane traffic occurs between 09:12 UT and 09:22 UT. The altitude profiles from this day is shown in figure (3.4). The electron density is high between approximately 07:30 UT and 10:00 UT. The height range is approximately 250-600 km. During this period, the electron temperature and ion temperature are mostly low, and it is difficult to distinguish between ion upflow and ion downflow in the ion velocity panel. The Matlab programmes *ekstremverdi2001.m* and *ekstremverdi2002.m* organizes the extreme densities according to onset time and duration, see appendix B and section (9.1.1).
All events from the two months are included in figure (4.3) and figure (4.4). In both figures, the number of events is plotted versus the events duration. However, the duration is though rather variable. The days with no detected extreme density around magnetic noon (≈ 4 days from 2002) are not included in this statistics. The very brief events which last for less than two minutes (the single detected events), constitute the largest part of the statistics. They occurred ca 60 times in the data from 2001 and ca 40-45 times in the data from 2002. Approximately 35 events are observed to last for 2-9 minutes in 2001, while 29 events are observed to last for 2-9 minutes in 2002. The number of extreme density events decreases as the duration increases. In 2001 there are approximately

25 events lasting for 10-120 minutes, while approximately 20 events lasting 10-120 minutes in 2002. The majority of events are below 10 minutes duration, which indicates possible segmentation of the TOI and isolated patch structures.

4.2 Selection of case studies

In addition to ESR data, SuperDARN coverage and ACE solar wind data were also used to identify the best suitable cases. The selection criteria were:

1. F_2 density $> 10^{12} m^{-3}$ in the ESR data
2. Best possible coverage of convection flow data from SuperDARN in order to trace the extreme electron densities backward to their source.
3. No airplane interruptions or gaps in the data coverage

The days which satisfy the criteria for ESR and SuperDARN are:

- 06 February 2001
- 07 February 2001
- 08 February 2001
- 19 February 2001
- 20 February 2001
- 24 October 2002

SuperDARN convection maps with 2-minutes time resolution were generated for all six days so they can be systematically studied in more detail during the extreme density events. Figure (**??**) shows an example of good coverage above Svalbard in the SuperDARN convection maps. The black dots indicate very low velocities, which could be ground scatter. These values are thus unreliable for the tracking of the extreme density events. All of the days listed above where attempted traced by the tracing procedure described in the next section. Most of the days showed fairly good tracing results, but the two days that stood out from the rest were:

- 06 February 2001
- 24 October 2002

These two days will be presented as detailed case studies in chapter 5.

4.3 Tracking polar cap extreme electron densities

To visualize and track where the extreme electron densities originated from, a program was made to follow the extreme densities backwards in time. The goal was to track the high plasma densities back to locations where the patch material had formed. The MATLAB programmes developed for this purpose are called *trace20021024.m* and *plot20021024.m*, both included in Appendix B in section (9.1.4) and in section (9.1.5). *trace20021024.m* performs the tracing

procedure, while *plot20021024.m* plots the trajectory of the extreme densities. The geometry and the algorithm behind the programmes are described in detail in section 4.3.1.

4.3.1 Geometry

The coordinate system used in the tracing procedure, is the Altitude Adjusted Corrected Geomagnetic Coordinate (AACGM) system [Baker and Wing, 1989]. The reason for choosing this type of coordinate system is that it is the default coordinate system for SuperDARN. Since the data used in this thesis are from 2001 and 2002, the 2000 version of the AACGM model is used. Given the geographic latitude, longitude and altitude, the model output is the AACGM latitude and longitude in degrees. Figure (4.5) shows how to determine the AACGM coordinates of a point. First, start at the point of interest (A) and trace the magnetic field lines using a reference magnetic field model, IGRF (International Geomagnetic Reference Field) to the geomagnetic equator. Then, the pure magnetic dipole model is used to trace the field line back to the surface of the Earth. The angle between the line joining the point on the Earth with the center of the Earth, and the axis which defines the magnetic dipole is then measured. It is the co-latitude of the point in magnetic coordinates. All points connected by a magnetic field line have the same coordinate in this system. The AACGM system is valid from the ground up to 1000 km. The effects of

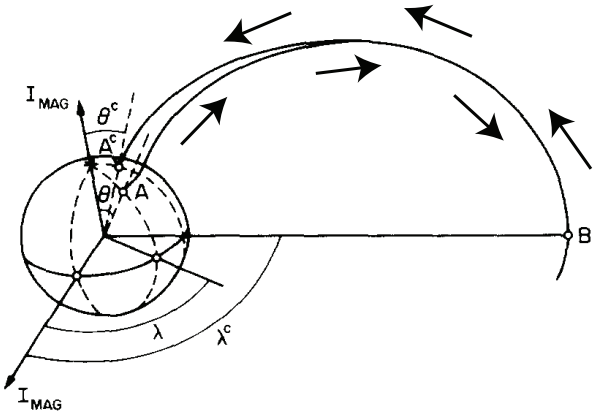

Figure 4.5: Altitude Adjusted Corrected geomagnetic coordinates (AACGM). A is the point of a geomagnetic field line from any point on the Earth's surface, C is the dipole equator plane, A^c is the starting surface, and the magnetic field intensity B is approximately constant along a model field line. λ is the magnetic longitude, I_{mag} is the dipole axis and θ is the angle between the line joining the point on the Earth with the center of the Earth. Figure adapted from Gustafsson et al. [1992].

the seasonal variation in the Sun's declination along with the variation in the Sun's apparent position due to the eccentricity of the Earth's orbit result in a variation of nearly 1 hour of magnetic local time for a fixed UT and geographic location over the course of a year. AACGM uses magnetic latitude, but replaces

the magnetic longitude with magnetic local time, see equation 4.8. That equation ignores the seasonal effect resulting from the Sun's apparent geographic north-south motion and the result of the eccentricity of the Earth's orbit known as the equation of time. For more theory about this coordinate system, see Baker and Wing [1989] and Gustafsson et al. [1992].

The geometry behind the tracing used in the program *trace20021024.m* is shown in figure (4.6(a)), and it is blown up in figure (4.6(b)). Spherical coordinates in degrees are used due to the fact that the colatitude is given in degrees, but it wouldn't be a problem to measure it in km (just divide by 360° and multiply with the Earth's circumference).
The starting point of the tracing is labeled (x_0, y_0) and the endpoint is labeled (x_1, y_1). The distance traveled in the x- and y-direction is respectively Δx and Δy. The speed is measured by SuperDARN in $\frac{m}{s}$ and given by v, while the distance from (x_0, y_0) to (x_1, y_1) is given by the following formula:

$$w = \frac{v \cdot t \cdot 360^\circ}{2\pi \cdot (R_E + h_{F_2})} \tag{4.1}$$

w is a scale factor given in degrees. $t = 120s$ due to the two minutes between each completed SuperDARN measurement. The last part of the expression $(\frac{360^\circ}{2\pi \cdot (R_E + h_{F_2})})$ is the degrees around the world divided by the radius of the earth ($R_E = 6370 \cdot 10^3 m$) plus an additional height up to the F_2-layer ($h_{F_2} = 300 \cdot 10^3 m$). By trigonometry (x_0, y_0) is calculated by the following formulas (see figure (4.6(b))):

$$x_0 = (90 - MLAT) \cdot \sin(MLT) \tag{4.2}$$

$$y_0 = -(90 - MLAT) \cdot \cos(MLT) \tag{4.3}$$

, where MLT is given in radians and $(90 - MLAT)$ is the colatitude. The distance between the starting point and the end point, (x_1, y_1) is given by the following two equations:

$$x_1 = x_0 + \Delta x \tag{4.4}$$

$$y_1 = y_0 + \Delta y \tag{4.5}$$

Δx and Δy can be found by trigonometry (see figure (4.6(b))):

$$\Delta x = -\Delta x_1 + \Delta x_2 = -w \cdot cos(az) sin(MLT) - w \cdot sin(az) sin(90 - MLT) \tag{4.6}$$

$$\Delta y = -\Delta y_1 + \Delta y_2 = w \cdot cos(az) cos(MLT) + w \cdot sin(az) cos(90 - MLT) \tag{4.7}$$

4.3.2 Algorithm tracing

The algorithm involves the following steps:

1. Load the different SuperDARN data needed in the calculations into various arrays.

2. Initialize the ESR position as a starting point (x_0, y_0) for the tracing when the first extreme densities are detected.

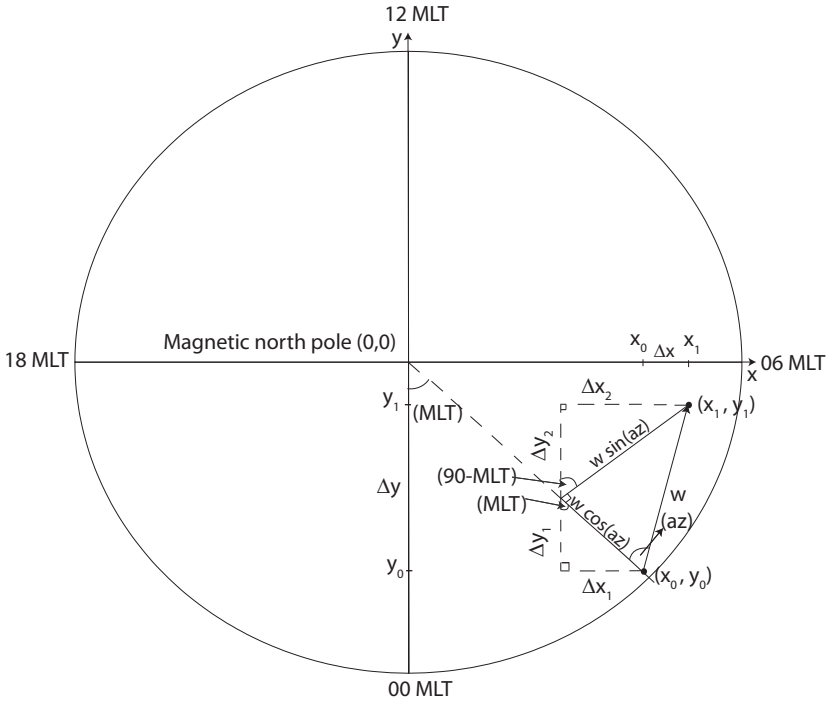

(a) The geometry behind the tracing in magnetic coordinates.

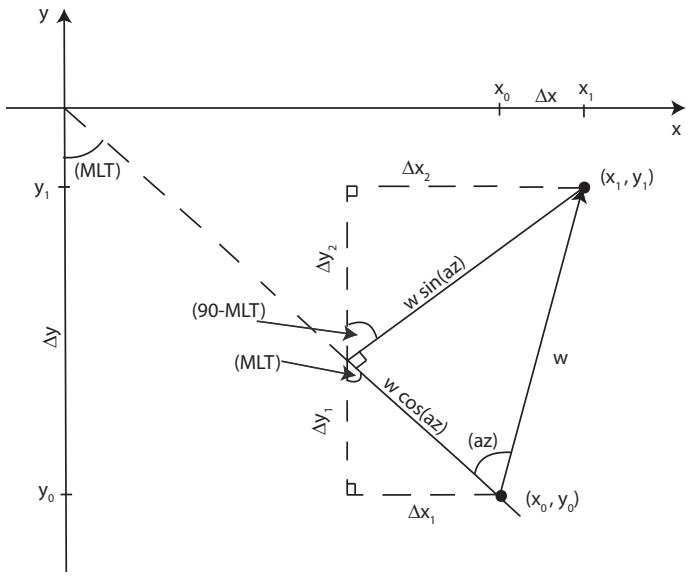

(b) This is a blow up of figure (4.6(a)).

Figure 4.6: The geometry behind the tracing in magnetic coordinates. The maps are centered on the magnetic north pole which is the origin at $(x, y) = (0, 0)$. The y-axis points towards the Sun which is on the top. v is the convection speed, (x_0, y_0) is the starting point for the tracing, while the next point is labeled (x_1, y_1). The distance traveled in the x-direction is Δx, and the distance traveled in the y-direction is Δy. (x_1, y_1) is the new starting point when the tracing continues.

3. Find the nearest data point in the SuperDARN grid by the use of the Pythagorean theorem.

4. Use the measured velocity in that point to calculate a new position (x_1, y_1).

5. Make the new position the next starting point $(x_0, y_0) = (x_1, y_1)$.

6. Repeat steps 2-5 for every 2-min interval the data is traced backward and forward.

The EISCAT Svalbard Radar is located at 75.37° magnetic latitude (MLAT) and 113.94° magnetic longitude (MLON). This location is used as a starting point for the tracing. Since the MLT is used, the magnetic longitude of the ESR needs to be changed into magnetic local time (MLT). A definition of magnetic local time, which is often used is given by the following equation, see Baker and Wing [1989]:

$$MLT = \frac{\Phi}{15} + const + UT \tag{4.8}$$

where Φ is the magnetic longitude of the point of interest, UT is given in hours and the constant is a reference point which here is determined by the MLT of the 0 magnetic longitude at 00 UT. This constant is given in the raw SuperDARN convection data files.

The SuperDARN data is organized in squared grids. Every grid point has its own MLAT and MLON value which is given in the convection data files, and all MLAT and MLON values are saved in separate arrays. The x-coordinate and y-coordinate can be calculated for each data point. Further, the closest point can be found by the Pythagorean theorem:

$$closestpoint = min((x - x_{ESR})^2 + (y - y_{ESR})^2) \tag{4.9}$$

where min is the smallest component. When the closest point is found, it is used in subsequent calculations to locate the new position.

The locations of Tromsø (TRO), Ny-Ålesund (NYA), Bjørnøya (BJN) and the EISCAT Svalbard radar (ESR) are indicated in the tracing. The geographic and magnetic coordinates from the AACGM 2000 model are given in table (4.1).

	Mag. lat.	Mag. lon.	Geo. lat.	Geo. lon.
Ny-Ålesund	76.0	112.2	78.9°N	12.0°E
ESR	75.1	112.9	78.2°N	15.7°E
Bjørnøya	71.3	108.8	74.5°N	19.0°E
Tromsø	66.6	103.6	69.8°N	19.0°E

Table 4.1: Magnetic latitude (MLAT), magnetic longitude (MLON), geographic latitude and geographic longitude for Ny-Ålesund, ESR, Bjørnøya and Tromsø.

Chapter 5

Case Studies

This chapter focuses on the two days selected for further studies. A systematic presentation of the extreme densities found, the IMF conditions, the large-scale ionospheric response seen by SuperDARN, and the final tracing of the extreme density events follows.

5.1 Tracking of extreme electron densities on 06 February 2001

5.1.1 Identification of extreme electron density events by EISCAT

The data set from 06 February 2001 meets the selection criteria described in section (4.2), and therefore contains the extreme density events wanted for further investigations. The ESR data from this day is shown in figure (5.1), with four panels of altitude profiles for the electron density (N_e), the electron- and ion temperature (T_e, T_i), and the ion velocity (V_i) versus time. The ionosphere between 100 km and 800 km altitude is shown on the figure, where the height of particular interest is between 250 km and 600 km. The white vertical lines in the plot are due to data gaps caused by airplane interruption. This outage usually last for approximately 10-minutes. The time-scale used in the plots is Universal Time (UT).

The first panel in figure (5.1) shows the electron density which contains two distinct cold plasma patches indicated by two arrows. The electron temperature shown in the second panel is mostly high (electron heating) during the time interval, with the exception of two periods where the temperature decreases significantly. This temperature drop is indicated by two black arrows. Each of these periods of cold electrons last approximately for half an hour. Low T_e indicates that there is no electron particle precipitation present, and thus there will be no heating caused by precipitation. The cooling rate (C_r) is given by equation (2.26), and for such high densities without any particle heating, the plasma will rapidly cool down. The ion temperature found in the third panel is high before 07:15 UT, and then it decreases until 08:15 UT. The temperature remains low in altitudes below 600 km, and increases above 600 km.

The ion velocity in the lowermost panel is toward the radar at low altitudes, and

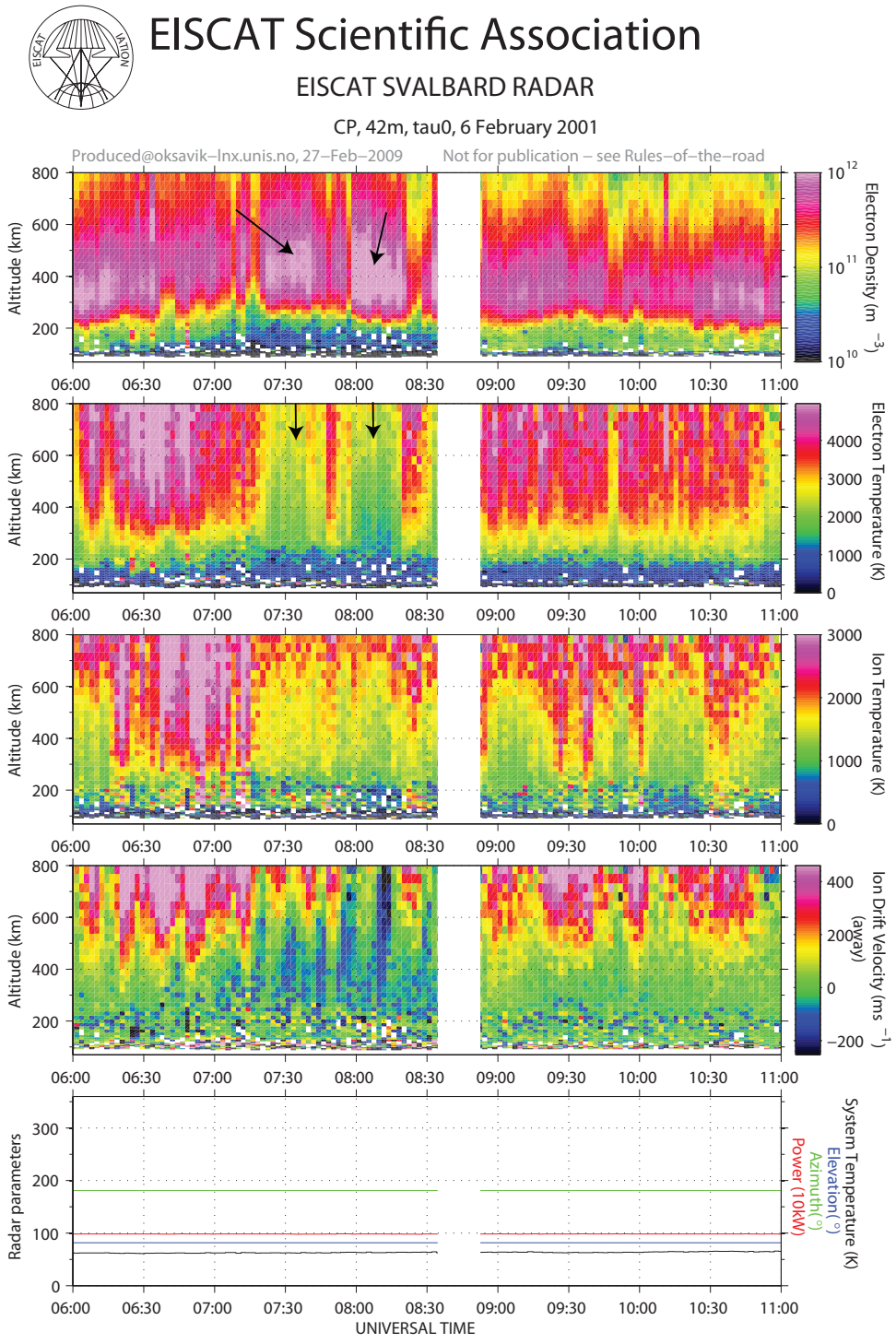

Figure 5.1: Altitude profiles of the electron density (N_E), the electron and ion temperature (T_e, T_i), and the ion velocity (V_i) between 06:00 UT and 11:00 UT on 06 February 2001. The first panel shows the electron density distribution, while the second panel shows the electron temperature, which indicates a temperature drop during the long duration events. The two lowermost panels show the ion temperature and the ion velocity, respectively. The white area shows a data gap due to an airplane interruption which lasts for approximately 10 minutes.

away from the radar at altitudes above 600 km, indicating ion downflow and upflow respectively. Ogawa et al. [2009] have recently investigated the characteristics of ion upflow and downflow observed with the ESR. Their study shows that ion upflow is more frequent on the dayside between 09:00 and 15:00 MLT (06:00 - 12:00 UT). Ion downflow is present in the same time interval, but only when the geomagnetic activity is high. They observed that ion upflow often are accompanied by ion and electron heating, and the occurrence frequency of dayside ion upflow increases with increasing strength of the IMF B_y component. From the second and third panels in figure (5.1) there exist electron heating and ion heating with the exceptions of the period when the two cold plasma patches are observed. The IMF B_y turns from strongly positive to negative, and then back to strongly positive again at approximately 06:30 UT. In this case, ion upflow is observed when the B_y is strongly positive, consistent with the observations of Ogawa et al. [2009].

Figure (5.2) shows the density maxima between 06:00 UT and 11:00 UT. Extreme densities are marked with cyan stars, while lower densities are marked with black stars. A horizontal line indicates the extreme density limit which is set to $10^{12}m^{-3}$. The events are numbered from 1 to 12, where grey color indicates short duration events, blue color indicates long duration events and the black dotted lines indicate single detected events less than two minutes duration.

The lowermost panel shows the height of the density maxima together with the altitude profile for the electron density in the lowermost panel. At bottom right, a color bar is shown, which gives an indication about the electron density. All of the detected events can in the lowermost figure be identified from the indicated events in the uppermost figure. The altitude of the maximum densities varies from approximately 250 km to 600 km. The altitude peak occurs between 07:00 UT and 08:00 UT where the altitude is varying between 450 km and 550 km. The rest of the period usually shows density maxima in the altitude range from 300 km to 400 km.

The occurrences of extreme density events on 06 February 2001 can be found in table (5.1). Two of the events stand out from the rest due to their longer duration. The two events last for 17 minutes and 19 minutes, respectively. It is worth noting that these two events also contain the highest value of electron density that is measured in this time interval. It appears that the longer the duration is, the higher value of the density is measured. This may be due to the strong convection flow that is present during the long duration events. The convection then reaches to lower latitudes, and will bring high density plasma from a sunlit area into the polar cap, see further discussion in section (6.1.1).

5.1.2 The solar wind driver according to ACE

To be able to trace the events from table (5.1), the IMF conditions also need to be examined. The shape of the convection pattern in the ionosphere is known to depend upon the magnetic field in the solar wind (IMF), and the $E \times B$ drift will transport the patch material following the convection pattern across the polar cap. The IMF is investigated for the period between 05:00 UT and 11:00 UT, i.e. in the period when Svalbard is around magnetic noon.

The time shifted IMF for the interval of interest is shown in figure (5.3), where

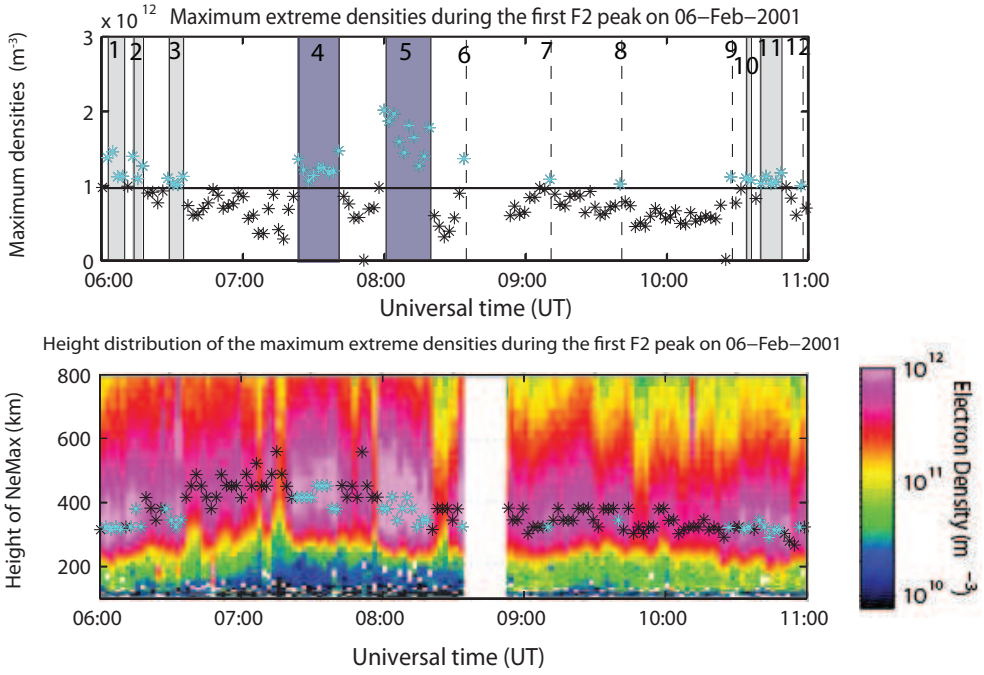

Figure 5.2: The uppermost panel shows the maximum density values (NeMax) between 06:00 UT and 11:00 UT on 06 February 2001. A horizontal line is drawn for $10^{12}m^{-3}$, which indicates the extreme electron density limit. The maximum electron densities above $10^{12}m^{-3}$ are shown as cyan stars, while maximum densities below this limit are shown as black stars. All extreme density events are labeled with the numbers 1 to 12. Grey color indicates short duration events, blue color indicates long duration events and the black dotted lines indicate single detected events, i.e the very brief events. The height of the density maxima are shown together with the corresponding altitude profile for the electron density in the lowermost panel. A color bar is shown at the bottom right, which gives an indication about the electron density.

No.	Start (UT)	End (UT)	Duration (min)	NeMax ($10^{12}m^{-3}$)
1	06:02	06:09	7	1.46
2	06:13	06:17	4	1.39
3	06:28	06:34	6	1.10
4	07:23	07:40	17	1.47
5	08:00	08:19	19	2.01
6	08:34	-	-	1.36
7	09:10	-	-	1.09
8	09:40	-	-	1.02
9	10:27	-	-	1.12
10	10:33	10:35	2	1.10
11	10:39	10:48	9	1.17
12	10:57	-	-	1.00

Table 5.1: Event number 1-12 on 06 February 2001 with start times and end times given in universal time (UT). The duration is given in minutes, and the maximum electron density for the event is given in $10^{12}m^{-3}$.

measurements from the two instruments MAG and SWEPAM are presented, see section (3.2). A time delay of 67 minutes was calculated by the simple approach method, see section (3.4.1).

The behavior of the different IMF components is described in the following way. The B_x component is negative until 06:15 UT, then it starts to fluctuate between positive and negative with 5-10 minutes intervals. At 06:45 UT it turns strongly negative until 09:15 UT, where it starts to fluctuate again. The IMF B_y component is strongly positive, fluctuating between 5-15 nT and stays stable for approximately the whole period. It performs a negative turn at approximately 06:30 UT, but turns positive again after 10 minutes. The IMF B_z component starts out negative before it turns positive for approximately 10 minutes at 05:50 UT. 10 minutes later it turns negative once again until approximately 06:15 UT. It stays positive until 07:00 UT where it turns negative for 10 minutes. Then it fluctuates near 0 before it turns strongly positive at 08:30 UT and remains positive for the rest of the period. See discussion in section (6.1.3).

5.1.3 The large-scale ionospheric response seen by SuperDARN

To be able to trace the extreme density events by SuperDARN convection data, good coverage of HF radar data in the polar cap is needed. A sequence of SuperDARN convection maps for event 4 is shown in figure (5.4). These maps show very good coverage of HF radar data above ESR during the whole extreme density event, which starts 07:23 UT and ends 07:40 UT. The plasma seems to enter from a sunlit area at lower altitudes, but also from the prenoon sector, see discussion below in section (5.1.6). Then it travels with high velocity across the polar cap, and follows the antisunward motion of the convection pattern. High flow velocity is also dominating the period before the extreme density events (not shown in the figure). The convection pattern is dominated by a strong positive IMF B_y component, i.e. the maps are dominated by a large afternoon

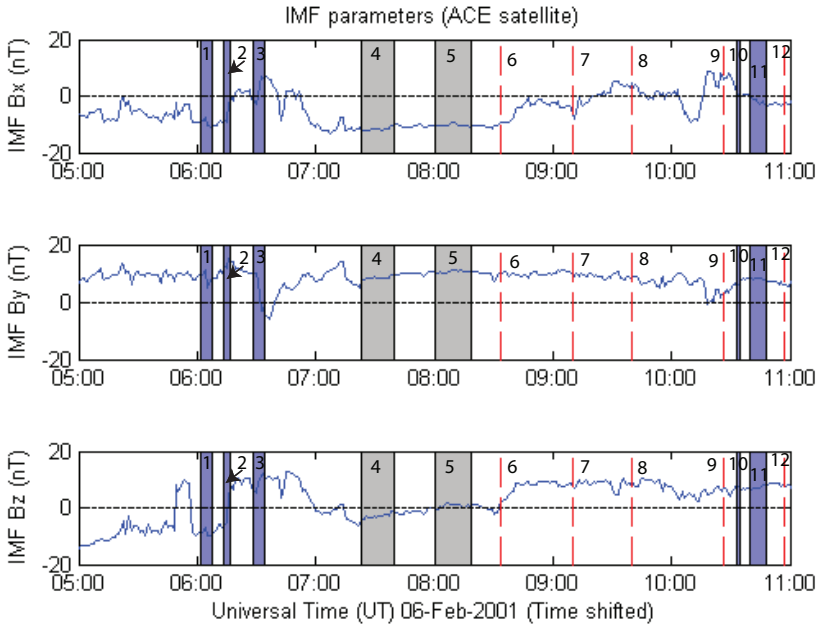

Figure 5.3: The interplanetary magnetic field measured by ACE on 06 February 2001. The uppermost panel shows the IMF B_x component, the middle panel shows the IMF B_y component, while the lowermost panel shows the IMF B_z component. The data in the figure is time shifted by 67 minutes as calculated by the simple approach method, see section (3.4.1). The events are indicated by numbers from 1 to 12, where the long duration events are shown with grey shading, the shorter events are shown in blue, while the single detected events are indicated by red dashed lines.

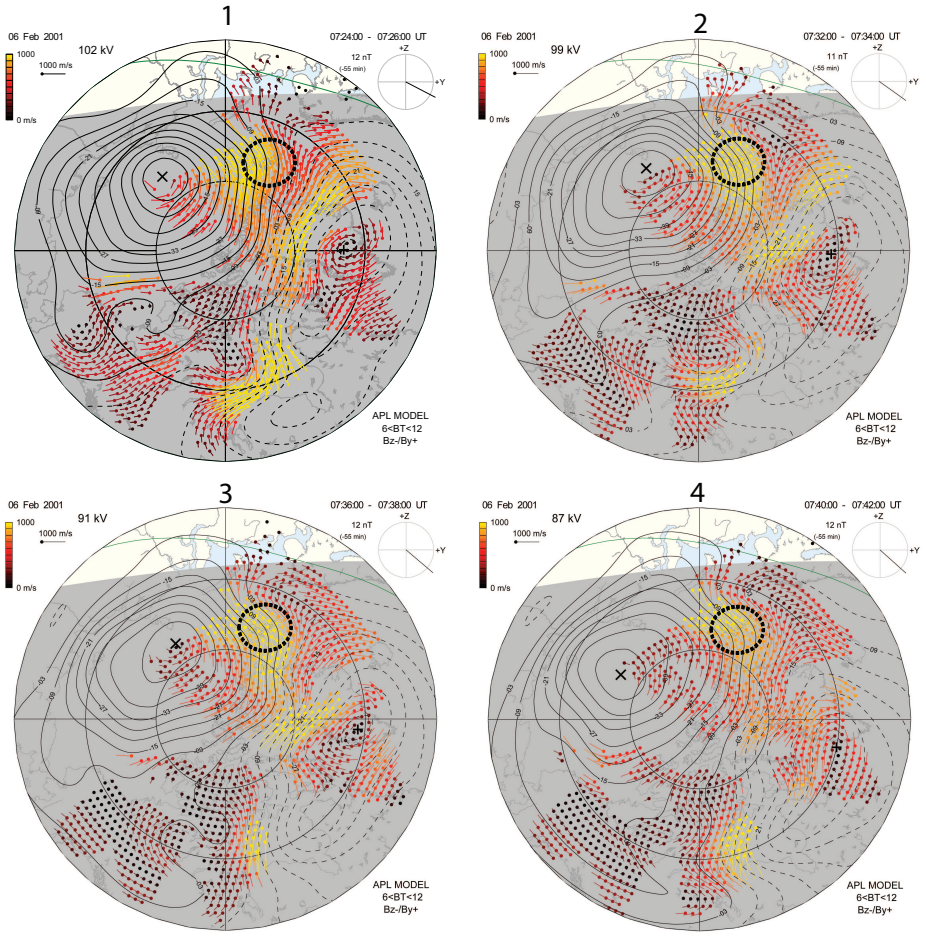

Figure 5.4: Sequence of SuperDARN convection maps during the extreme density event 4 on 06 February 2001. The event starts 07:23 UT and ends 07:40 UT. Svalbard is indicated by a black circle on the maps.

cell and a small morning cell, see section (2.7.3). For further discussion, see section (6.1.3).

Figure (5.5) shows a sequence of convection maps for the extreme density event 5 which starts 08:00 UT and ends 08:19 UT. Good coverage above Svalbard is present during the whole event. This event shows a different result than the previous event, since the region above Svalbard is dominated by high-speed convection only in panel 1 and panel 6. In panel 2, the velocity has decreased and remains so in the middle panels. In panel 5, the velocity increases again and continues to increase in panel 6. The reason for this is probably that the F-region plasma often remains in the sunlit region for an extended period of time due to counteracting co-rotation and convection electric fields. This plasma is then called stagnate plasma, since the Earth and the solar wind driven convection pattern rotate separate ways. Eventually the stagnate plasma is extruded by the convection electric field, through the cusp and across the polar cap. The polar cusp inflow region is thus important because it plays an important role in the entry of solar EUV ionized plasma. From these maps it is clear that the electron enhancements seem to enter from a sunlit area in the postnoon sector, which indicates a plasma source of EUV ionized plasma, rather than local production, see section (6.1.2). There is some backscatter in the upper right corner of the maps, but since this is probably due to groundscatter, it is unlikely that the plasma is coming from this direction. Also for this case, the convection pattern is dominated by strong positive B_y component, and thus the convection follows the pattern described in section (2.7.3).

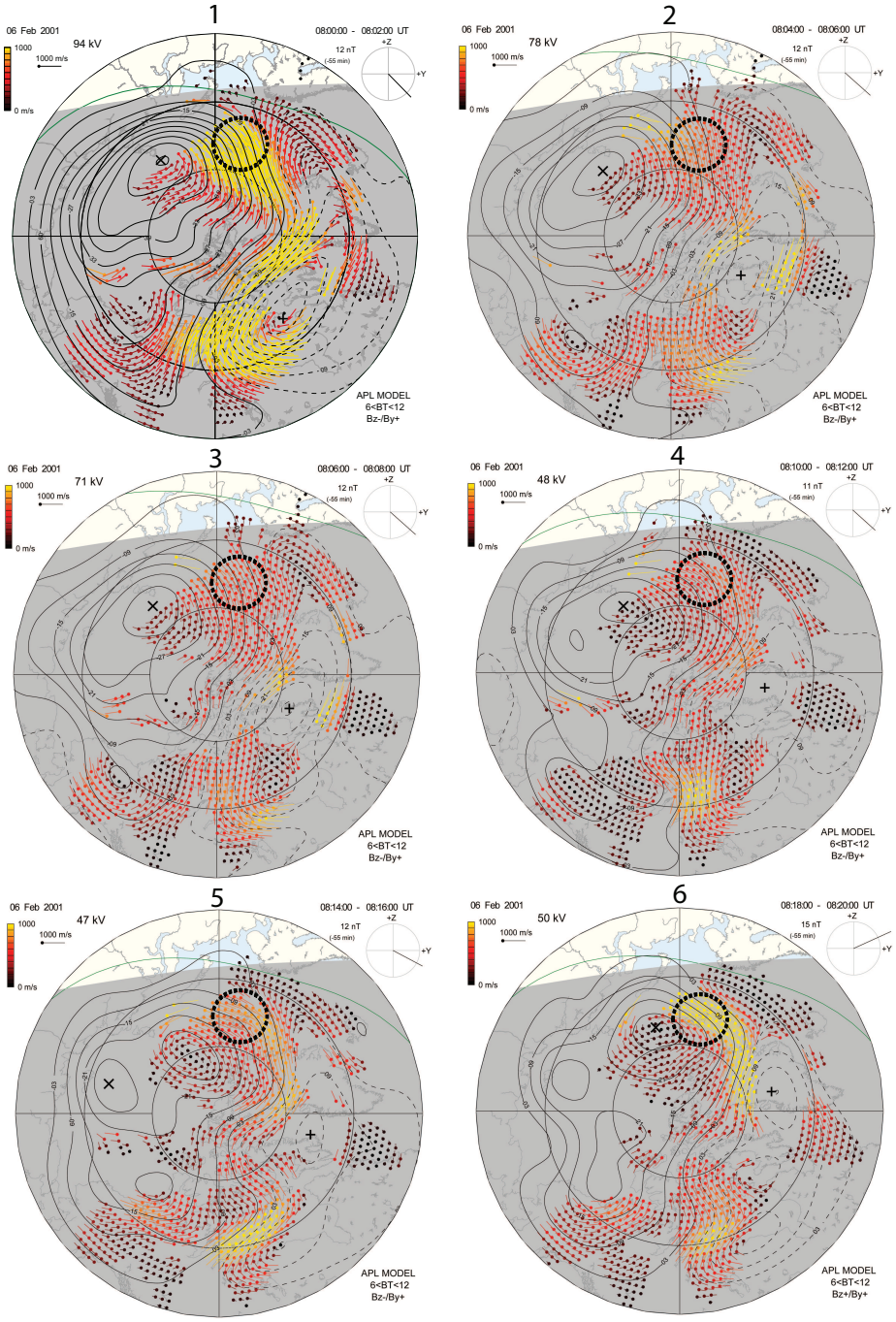

Figure 5.5: Sequence of SuperDARN convection maps during the extreme density event 5 on 06 February 2001. The event starts 08:00 UT and ends 08:19 UT. Svalbard is indicated as a black circle on the maps.

5.1.4 Tracing - where did the extreme densities originate from?

Since the extreme densities ($> 10^{12} m^{-3}$) occur in a more or less regular pattern around magnetic noon, which is consistent with the cusp inflow region near noon, it is meaningful to make an attempt to trace extreme densities backward in time in order to identify the source region. The program *trace20010206.m* performs the tracing procedure described in section (4.3.1), while the program *plot20010206.m* plots the result. The programmes are to be found in appendix B, in section (9.1.4) and in section (9.1.5). All events presented in table (5.1) where traced, except for the very brief events lasting less than two minutes.

Event 4: 07:23 - 07:40 UT

Figure (5.6(a)) shows the tracing of event 4 which starts at 07:23 UT. The extreme density event is traced two hours backward and two hours forward in time, with the ESR location in MLAT/MLT at 07:23 UT as the starting position. Every half hour is displayed on the figure together with the geographic location of the EISCAT Svalbard Radar (ESR), Bjørnøya (BJN), Tromsø (TRO) and Ny-Ålesund (NYA) at 07:23 UT. In the period before 07:00 UT and after 09:00 UT, only model data exist. The forward tracing is thus successful, while the backward tracing seem to stagnate after approximately 30 minutes. The space between the dots indicates the flow velocity across the polar cap. When the distance between the dots is small, the velocity is low, and when the distance increases, the velocity increases. It is therefore clear from the maps that the plasma material travels with the highest speed from ESR toward Greenland between 07:30 UT and 08:00 UT.
The figure shows that plasma is transported from a solar EUV ionized plasma region near noon into the polar cap, which means that there exists a systematic intake of solar EUV ionized plasma in the cusp inflow region, see further discussion in section (6.2).

Figure (5.6(b)) shows the magnetic azimuth direction and the flow velocity at which the polar cap patch material travels across the polar cap. The azimuth seems to be rather stable, indicating that the patch travels in a continuous direction, while the velocity fluctuates between 50 m/s and 1000 m/s. The red color indicates the backward tracing, while the blue color indicates the forward tracing. The velocity starts out rather low at 05:00 UT and then the speed increases until it reaches a peak level around 900 km/s at approximately 07:30 UT when the patch material enters the cusp inflow region. From here, the velocity fluctuates between 500 m/s and 1000 m/s for about an hour. Then the speed decreases, but continue to fluctuate. The varying speed indicates flux transfer events, further discussed in section (6.2). The enhanced density travels across the polar cap for a period of a couple of hours. When the tracing reaches areas with model data only, the tracing starts to stagnate and the result is rather uncertain. Thus, good coverage of radar data over the polar cap is necessary for this tracing method to work properly and to be reliable. The velocity seems to decrease over time for the backward tracing, and reaches very low velocities before 06:00 UT. This is probably also a reason for plasma to stagnate, see discussion below in section (5.1.6).

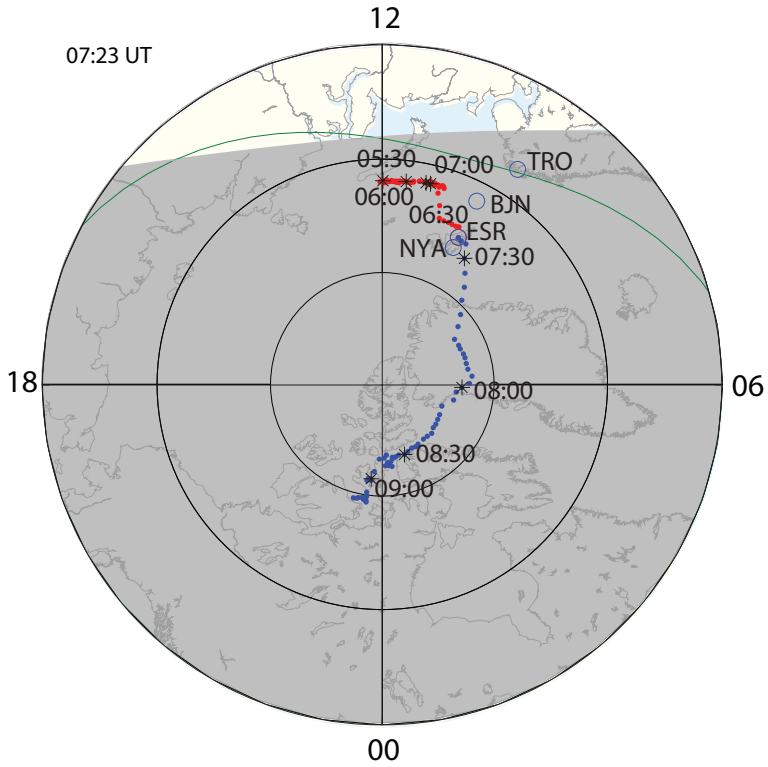

(a) The result of the tracing of event 4 in magnetic coordinates. The map shows the situation at 07:23 UT.

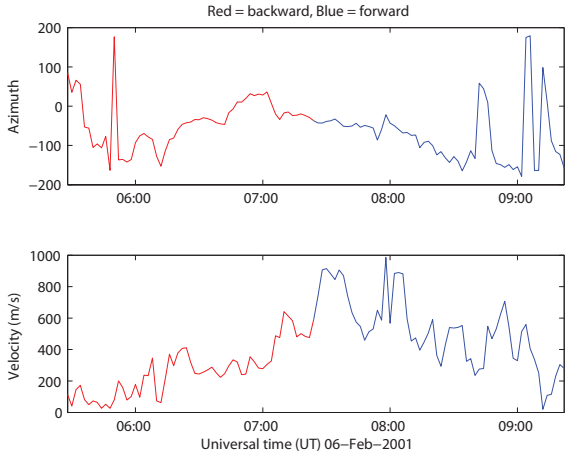

(b) Magnetic azimuth and flow velocity during the tracing. The transition between red color and blue color indicates where the extreme density event is first detected by ESR, that is 07:23 UT.

Figure 5.6: a) The result of the tracing of the extreme density event 4, where magnetic coordinates are used. Two hours forward in time (shown in blue color) and two hours backward in time (shown in red color) have been used for the time of tracing. The locations of the EISCAT Svalbard radar (ESR), Bjørnøya (BJN), Ny-Ålesund (NYA), and Tromsø (TRO) at 07:23 UT are labeled on the figure. Magnetic noon is at the top. The solar terminator is shown with grey shading. b) Magnetic azimuth and flow velocity for the same event. Red color indicates the backward tracing, while the blue color indicates the forward tracing. Note how the flow velocity fluctuates.

Event 5: 08:00 - 08:19 UT

The tracing of event 5 is shown in figure (5.7(a)). The start time of the tracing is 08:00 UT, where the extreme density has been traced two hours forward and two hours backward in time. The tracing for this event is more successful than event 4 due to better coverage of SuperDARN convection data. Model data exists before 07:00 UT and after 09:00 UT, which means the tracing uses reliable data to trace the event one hour forward in time and one hour backward in time. Before and after this time model data is used, and from here the tracing is not reliable. It seems most likely that the tracing is successful until it enters equatorward of which there is no HF backscatter. The distance between the dots, is a measure of the velocity. From figure (5.7(a)), it thus seems that the enhanced densities travel with highest velocity in the period between 08:30 UT and 09:00 UT, and 15 minutes backward in time from the location of ESR at 08:00 UT. The backward tracing shows that the plasma seems to follow a convection streamline, and thus do not originate in sunlit areas. Even if this is the result here, it is only based on model data, and thus the resulting path from before 07:00 UT is not reliable. It is therefore not possible to give any definite conclusion on where the plasma seems to enter from for this case. However, the enhanced density seems to be sweeping through the sunlit area in the postnoon sector, and thus it is most probable that the origin is as proposed in the previous case.

Figure (5.17(b)) shows the magnetic azimuth direction and the flow velocity for event 5. Red color indicates the backward tracing, while blue color indicates the forward tracing. Like the previous event, the azimuth is stable which indicates that the enhanced densities travels along a straight path. The flow velocity is fluctuating a lot, from approximately 250 m/s to 1200 m/s. The velocity starts out at approximately 250 m/s and increases while it fluctuates. In the period when the tracing is reliable (from 07:00 UT to 09:00 UT), the velocity has 3 clear peaks at approximately 30-40 minutes intervals. At the end of the forward tracing, the velocity seems to stabilize around 500 m/s. Since the motion of the patch material is stepwise, this indicates transient magnetic reconnection going on at the magnetopause and thus flux transfer events. See discussion in chapter (6).

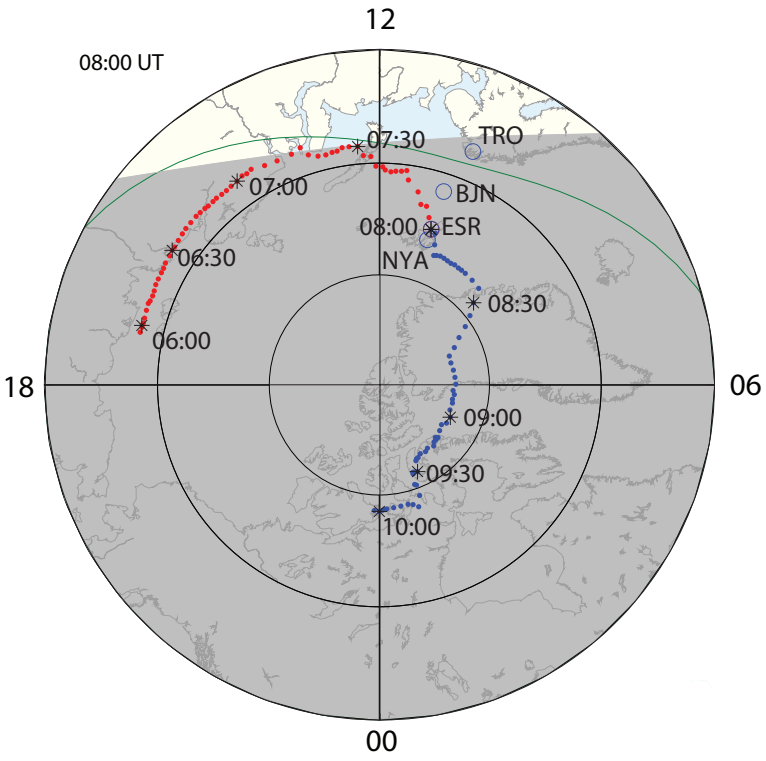

(a) The result of the tracing of event 5 in magnetic coordinates. The map shows the situation at 08:00 UT.

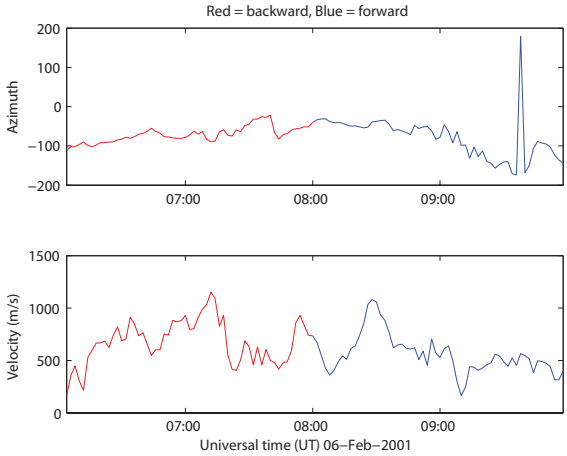

(b) Magnetic azimuth and flow velocity during the tracing. The transition between red color and blue color indicates where the extreme density event is first detected by ESR, that is 08:00 UT.

Figure 5.7: a) The result of the tracing of the extreme density event 5, where magnetic coordinates are used. Two hours forward in time (shown in blue color) and two hours backward in time (shown in red color) from 08:00 UT have been used for the tracing. The locations of the EISCAT Svalbard radar (ESR), Bjørnøya (BJN), Ny-Ålesund (NYA), and Tromsø (TRO) at 0800 UT are labeled on the figure. Magnetic noon is at the top. The solar terminator is shown with grey shading. b) Magnetic azimuth and flow velocity for event 5 on 06 February 2001. Red color indicates the backward tracing, while the blue color is indicating the forward tracing. Note the fluctuating flow velocity.

Unsuccessful attempts

Event number 1, 2, 3 and 11 of the short duration (less than 2 minutes) events are shown in figure (5.8), with their start times 06:02 UT, 06:13 UT, 06:28 UT and 10:39 UT respectively. The only reliable period for the tracing this day is

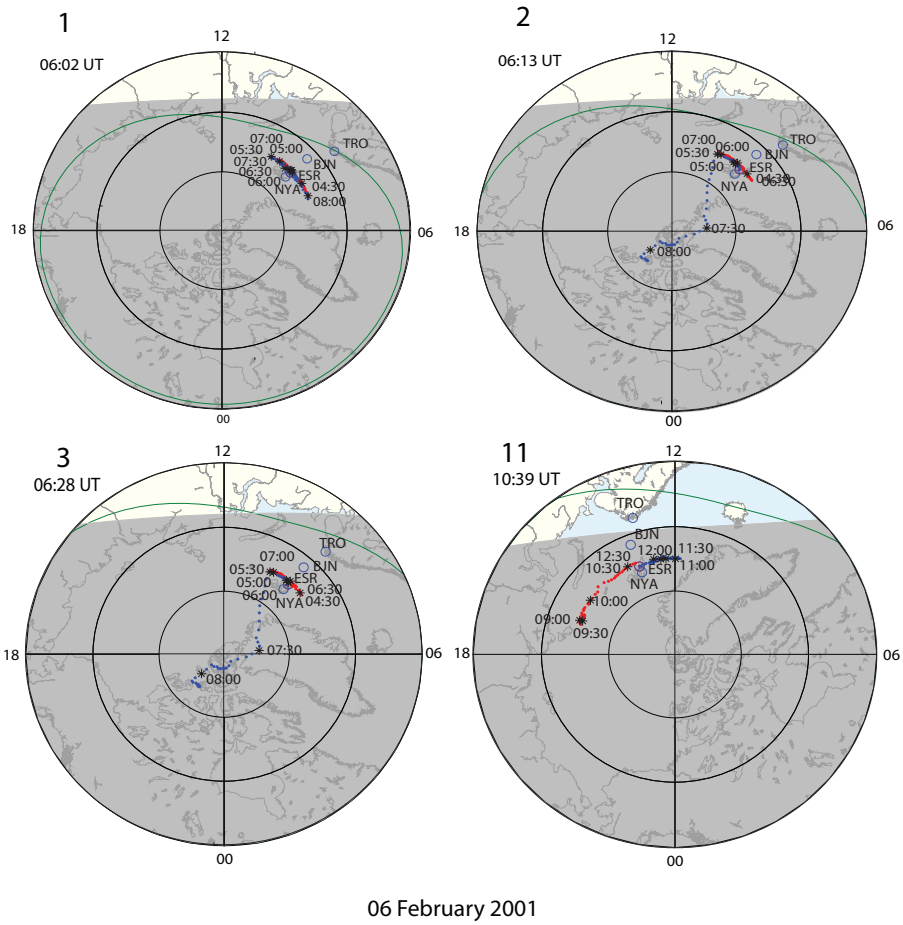

Figure 5.8: Unsuccessful attempts to trace the short duration (less than 2 minutes) events on 06 February 2001. Event number 1, 2, 3 and 11 are shown. Event no. 2 and 3 show two interesting cases of possible stationary patches.

between 07:00 UT and 09:00 UT, and thus these events were all unsuccessful attempts of the tracing due to model data only. A correlation between the IMF and these unsuccessful attempts was examined, but without any particular result. If we ignore that there is no reliable results from these events, the resulting path from event 2 and 3 are after all still interesting. They show stagnation of plasma which starts to drift across the polar cap when the tracing reaches areas with measured SuperDARN convection data, i.e. from 07:00 UT. A possible explanation for this is discussed in section (6.3.1).

5.1.5 Tomography

Ionospheric tomography is a technique for the spatial imaging of ionospheric electron density [Austen et al., 1986; Raymund et al., 1990, 1993], and Austen et al. [1986] was the first to suggest the application of tomographic techniques to image the electron density. The line integral of electron density, known as the total electron content (TEC) is measured over a large number of intersecting paths crossing a region of interest. The resulting tomography plots are two dimensional images of electron density as a function of height and latitude, as shown in figure (5.9) and figure (5.10). The best suitable tomography map for event 4 is shown in figure (5.9) for the time 06:48 UT. The aim is to compare the tomography map with tracing to see if the potential source can be seen in the maps. The highest densities seen in map that matches with event 4 is $5 \cdot 10^{11} m^{-3}$, and thus no extreme densities are observed. Nor figure (5.10) which shows the best suitable tomography pass for event 5 at 08:46 UT observes extreme densities. The highest value in this map is $7 \cdot 10^{11} m^{-3}$. The potential source of extreme densities could thus not be identified from these maps, and the reason for this is probably that the measured extreme density by ESR is observed 24 minutes after the tomography pass for event 4 and 36 minutes before the tomography pass for event 5.

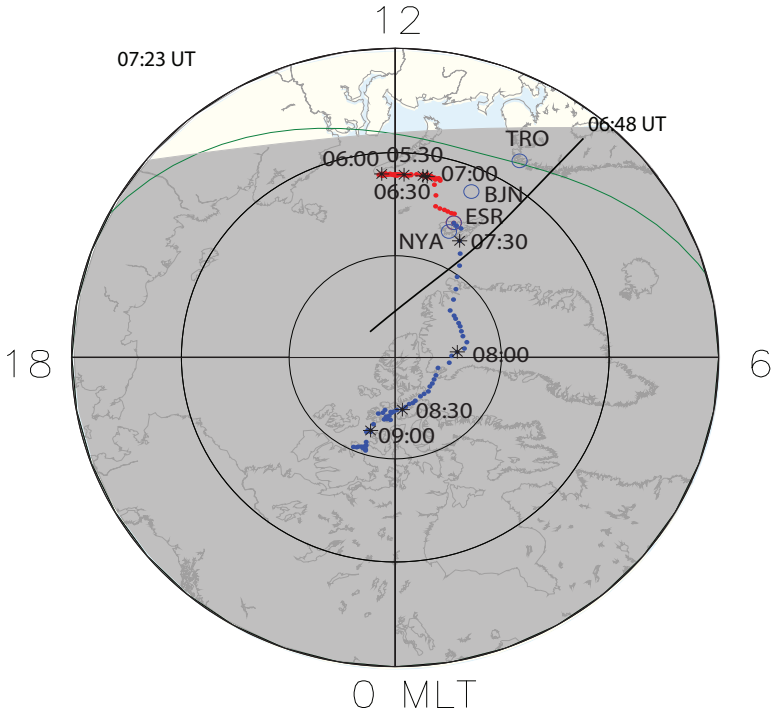

(a) The best suitable tomography pass at 06:48 UT for event 4 on 06 February 2001. The map shows the situation at 07:23 UT, and the tomography pass is drawn with a thick line.

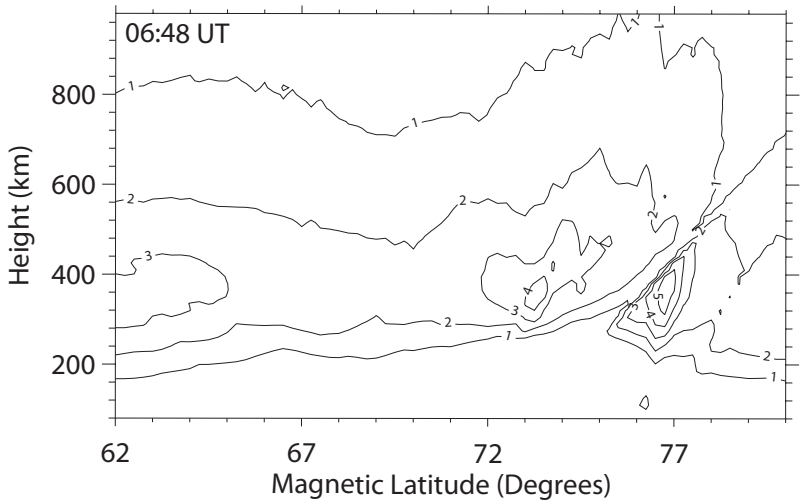

(b) The corresponding tomography map for event 4. The time for this tomography map is 06:48 UT.

Figure 5.9: The best suitable tomography pass for event 4 on 06 February 2001. The tomography maps are provided by Eleri Pryse.

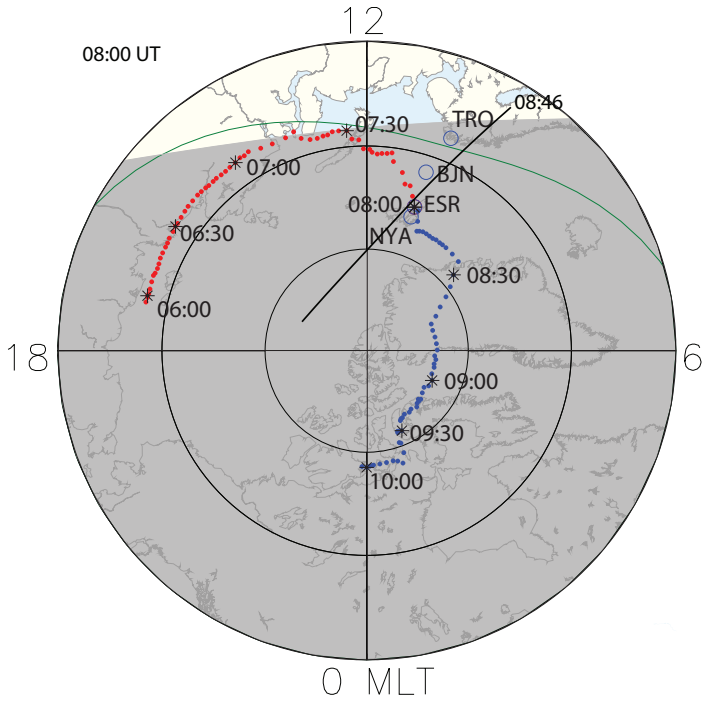

(a) The best suitable tomography pass at 08:46 UT for event 5 at 08:00 UT on 06 February 2001. The map shows the situation at 08:00 UT, and the tomography pass is drawn with a thick line.

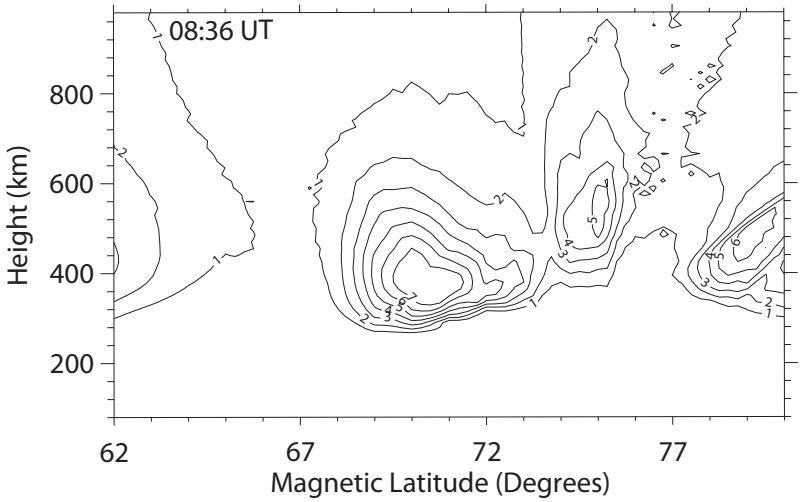

(b) The corresponding tomography map for event 5. The time for this tomography map is 08:36 UT.

Figure 5.10: The best suitable tomography pass for event 5 on 06 February 2001. The tomography maps are provided by Eleri Pryse.

5.1.6 Discussion: How reliable are these results?

Two events from 06 February 2001 where successfully traced backward and forward in time by the tracing method. An attempt to trace the shorter duration events was also made, but the very brief events where not usable for the tracing due to their lack of continuity. From the result its clear that the

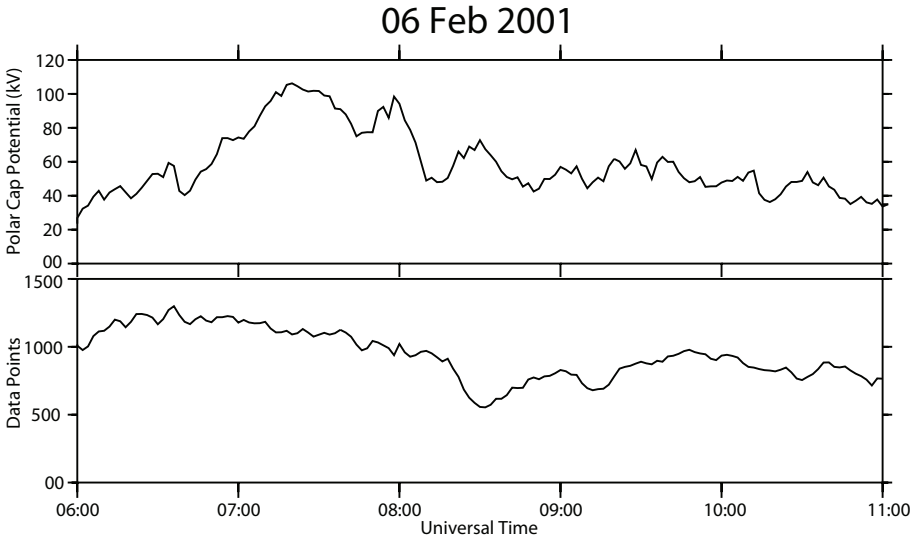

Figure 5.11: The upper panel shows the SuperDARN polar cap potential versus universal time on 06 February 2001, while the second panel shows the number of data points in the SuperDARN maps. The figure is provided by Kjellmar Oksavik.

method works well for areas with good SuperDARN coverage over the polar cap. In areas where only model data exist, the tracing seems to stagnate and this gives a rather uncertain result, for instance event 4, see figure (5.6(a)). The stagnation is probably not totally due to model data alone. The flow velocity shown in figure (5.6(b)) indicates low flow velocity across the polar cap. Before 06:00 UT, the velocity is between 50 and 100 m/s, which is very low. Thus, the patch material will be detached plasma which almost does not move.The SuperDARN convection maps show good coverage above Svalbard, and by comparing these maps with the tracing figures, it turns out that the period before 07:00 UT and after 09:00 UT our tracing is based on model data only. Thus, event 4 consist of approximately 20 minutes of reliable data for the backward tracing and one and a half hour with reliable data for the forward tracing. Event 5 consist of one hour reliable data for both the forward and backward tracing. Event 1, 2, 3 and 11 were all unreliable in the tracing due to only model data. The large-scale ionospheric response seen from the SuperDARN convection maps shows that the plasma seems to enter from a sunlit area at lower altitudes, but also from the prenoon sector. However, the tracing never observes plasma coming from the prenoon sector. The threshold for extreme density are set high ($N_e > 10^{12} m^{-3}$), and thus we exclude particle ionized patches which have been observed by MacDougall and Jayachandran [2007], see

discussion in section (6.1.2). MacDougall and Jayachandran [2007] found that these patches mainly come from the prenoon sector, and the high plasma densities observed is possibly due to the long exposure to precipitation during the return flow. The observed plasma coming from the prenoon sector is in our case probably due to returning plasma traveling with the return flow. The return flow often passes around the dawn convection cell due to the co-rotation effect [MacDougall and Jayachandran, 2007].

The upper panel of figure (5.11) shows the polar cap potential based on the SuperDARN model. It gives an idea of how expanded the polar cap is and how strong the solar wind E-field is over the polar cap. The lowermost panel in figure (5.11) shows the number of data points in the SuperDARN maps. This gives us an indication about the reliability of the tracing, since the more data points, the more accurate result. The y-axis goes from 0 to 1500 data points, where 1500 data points are equivalent to having data in half of the area in the polar cap, north of 60 MLAT. The SuperDARN data are divided into equal area grids of 110 km $\times$ 110km, where 1° latitude = 110 km north-south. Every box covers approximately 12 000 square km. Typically there is not data in the entire field of view of a radar, since only the signal orthogonal to the irregularities in the F-layer will give backscatter [Greenwald et al., 1995], see section (3.1.2). 1500 data points are very high, and this value was close to optimal with the 2001/2002 coverage of SuperDARN radars in the polar cap. Approximately half of the polar cap was without SuperDARN coverage in these years. In Russia, for example, there is little or no SuperDARN coverage. There are over 1000 points in the SuperDARN maps on this day, which is very high and will provide us with quite reliable results. The polar cap potential shows two pulses, one around 07:20 UT and one around 08:00 UT. This corresponds to the two events investigated above, that is event 4 which starts 07:23 UT and event 5 which starts 08:00 UT. These two events are the events with the longest duration this day and both of them can be defined as patches. The convection is rather strong in the period before these two events, which may indicate that high density plasma is brought extremely effective into the polar cap from subauroral latitudes.

The detection of extreme densities above ESR when Svalbard is close to magnetic noon can work as a forecast for communication and navigation users in Greenland, Canada and US. As can be seen from the figures presented of the tracing above, the enhanced density seems to travel across Greenland and can therefore most likely will be detected at a later time by the Sondrestrom incoherent scatter radar ($66.99°N, 309.05°E$) in Greenland. Unfortunately the Sondrestrom incoherent scatter radar was not in operation in the time interval investigated this day [personal communication with Anja Strømme].

5.2 Tracking of extreme electron density events on 24 October 2002

5.2.1 Identification of extreme electron density events by EISCAT

The data set from 24 October 2002 also meets the selection criteria described in section (4.2). The ESR data from this day is shown in figure (5.12). The four panels show the altitude profiles of the electron density (N_e), the electron- and ion temperature (T_e, T_i), and the ion velocity (V_i) versus time. The panels illustrate the ionosphere between 100 km and 800 km, where the height of interest is between 250 km and 600 km. The white vertical lines in the plot are due to data gaps caused by airplane interruption, and the time scale is Universal Time (UT).
As opposed to the electron temperature drop found in the previous case, this day shows high electron density and high electron temperature simultaneously. This is an indication of ongoing precipitation, and that aurora is present in the ESR beam. The lowermost panel shows ion upflow between 08:00 UT and 09:30 UT in the altitude above 400 km. As described in section (5.1.1), Ogawa et al. [2009] found that electron and ion heating often is present during ion upflow, and also that when the strength of the IMF B_y component increases, the occurrence frequency of dayside ion upflow also increases. On this day, there exist both ion heating and electron heating during the period of ion upflow. The IMF B_y is mostly strongly positive, with some fluctuations at the end of the period investigated, but are largely strongly positive, see next section. Figure (5.13) shows the density maxima between 06:00 UT and 11:00 UT. The extreme densities are marked with cyan stars, while lower densities are marked with black stars. The horizontal line indicates the extreme density limit which is set to $10^{12}m^{-3}$. The events are numbered from 1 to 6, where the blue color indicates the two longest events on this day and the black dotted lines indicate single detected events.
The lowermost panel shows the height of the density maxima together with the altitude profile for the electron density in the lowermost panel. The color bar to the bottom right, gives an indication of the electron density. All of the detected events can in the lowermost figure be identified from the indicated events in the uppermost figure. The altitude of the maximum densities varies from approximately 250 km to 600 km. The altitude peak occurs at approximately 06:45 UT where the altitude is varying between 400 km and 600 km. The rest of the period usually shows density maxima in the altitude range from approximately 300 km to 450 km.

Table (5.2) shows the occurrences of extreme density events between 06:00 and 11:00 UT on this day. This day contains one short event with two minutes duration and one longer event of 11 minutes duration. There are also four very brief events on this day. Event 3 was the only event that could be defined as a patch, and this event also contains the highest value of the density measured, see discussion in section (6.1.1.)

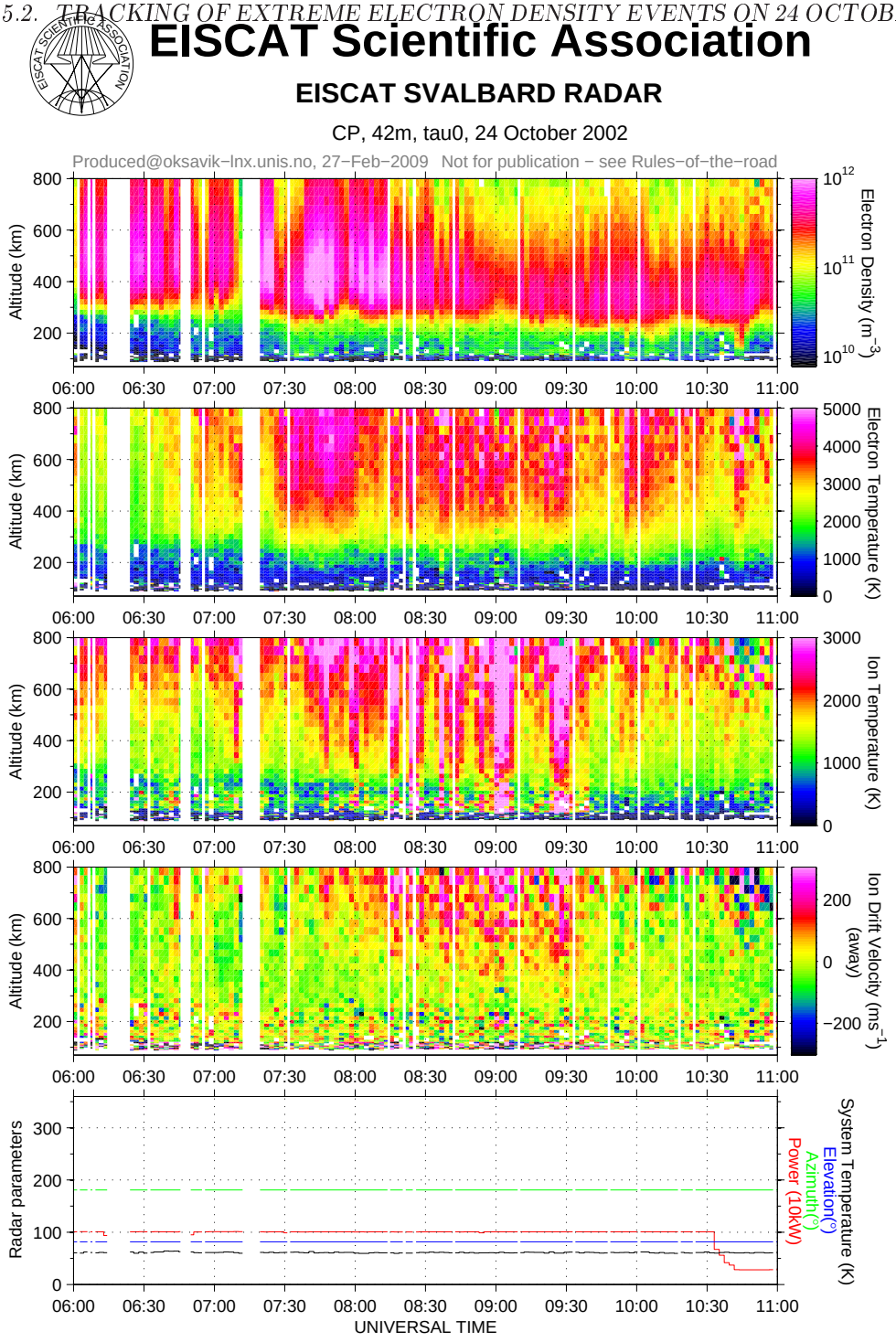

Figure 5.12: Altitude profiles of the electron density (N_e), the electron and ion temperature (T_e, T_i), and the ion velocity (V_i) on 24 October 2002. The first panels show the electron density distribution, while the second panel shows the electron temperature, which shows enhanced electron heating during the events. The two lowermost panels are the ion temperature and the ion velocity, respectively. The white areas indicate data gaps due to for instance airplane interruptions.

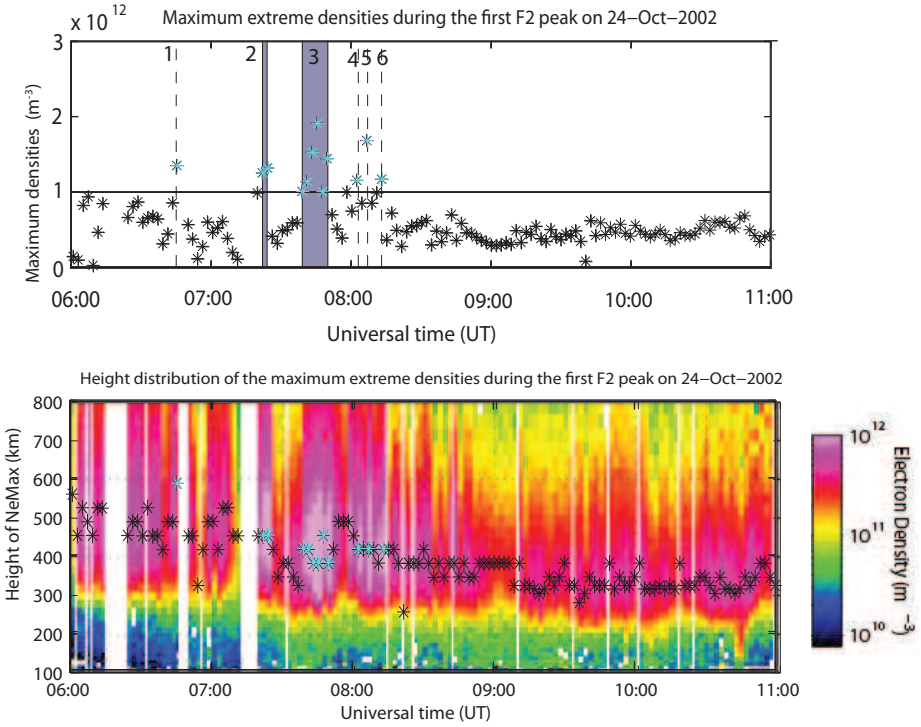

Figure 5.13: Extreme densities on 24 October 2002 from 06:00 UT to 11:00 UT. The uppermost panel shows the maximum density values (NeMax) between 06:00 UT and 11:00 UT. A horizontal line is drawn for $10^{12}m^{-3}$, which indicates the extreme electron density limit. The maximum electron densities above $10^{12}m^{-3}$ are shown as cyan stars, while maximum densities below this limit are shown as black stars. The height of the density maxima are shown together with the corresponding altitude profile for the electron density in the lower most panel. A color bar is shown to the bottom right, indicating the value of the electron density.

No.	Start (UT)	End (UT)	Duration (min)	NeMax ($10^{12}m^{-3}$)
1	06:45	-	-	1.35
2	07:22	07:24	2	1.32
3	07:39	07:50	11	1.91
4	08:03	-	-	1.15
5	08:06	-	-	1.68
6	08:13	-	-	1.17

Table 5.2: Event number 1 to 6 with start times and end times given in universal time (UT). The duration is given in minutes, and the maximum electron density for the event is given in $10^{12}m^{-3}$.

5.2.2 The solar wind driver according to ACE

Figure (5.14) shows the IMF from 05:00 UT to 11:00 UT. The measurements are from the two instruments MAG and SWEPAM on the ACE spacecraft, which are described in section (3.2). The data in the figure is time shifted by 52 minutes as calculated by the simple approach method, see section (3.4.1). The IMF B_x component is shown in the uppermost panel, and is negative and quite stable during the whole period investigated. The panel in the middle shows the IMF B_y component, which is stable and mostly strongly positive until 08:45 UT. Through the rest of the interval it fluctuates between positive and negative. The B_z component is shown in the lowermost panel and this component is mostly negative, but has a few excursions to weakly positive. After 10:30 UT B_z turns significantly positive. See discussion in section (6.1.3).

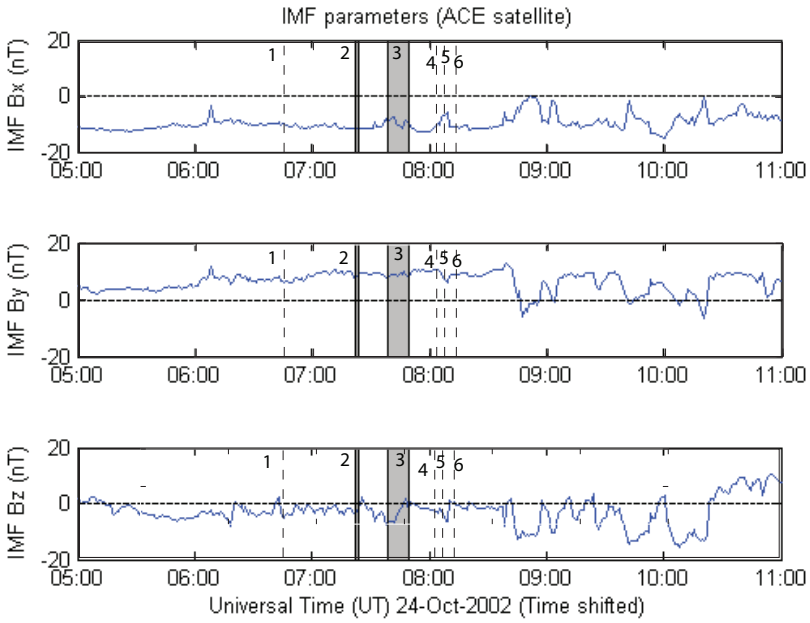

Figure 5.14: The Interplanetary Magnetic field measured by ACE between 05:00 UT and 11:00 UT. The data in the figure is time shifted by 52 minutes as calculated by the simple approach method. The uppermost panel shows the IMF B_x component, the middle panel shows the IMF B_y component, and the lowermost panel shows the IMF B_z component. The events investigated are indicated by numbers from 1 to 6, the two events with longer duration are shown in grey color, while the very brief events are indicated by black dotted lines.

5.2.3 The large-scale ionospheric response seen by SuperDARN

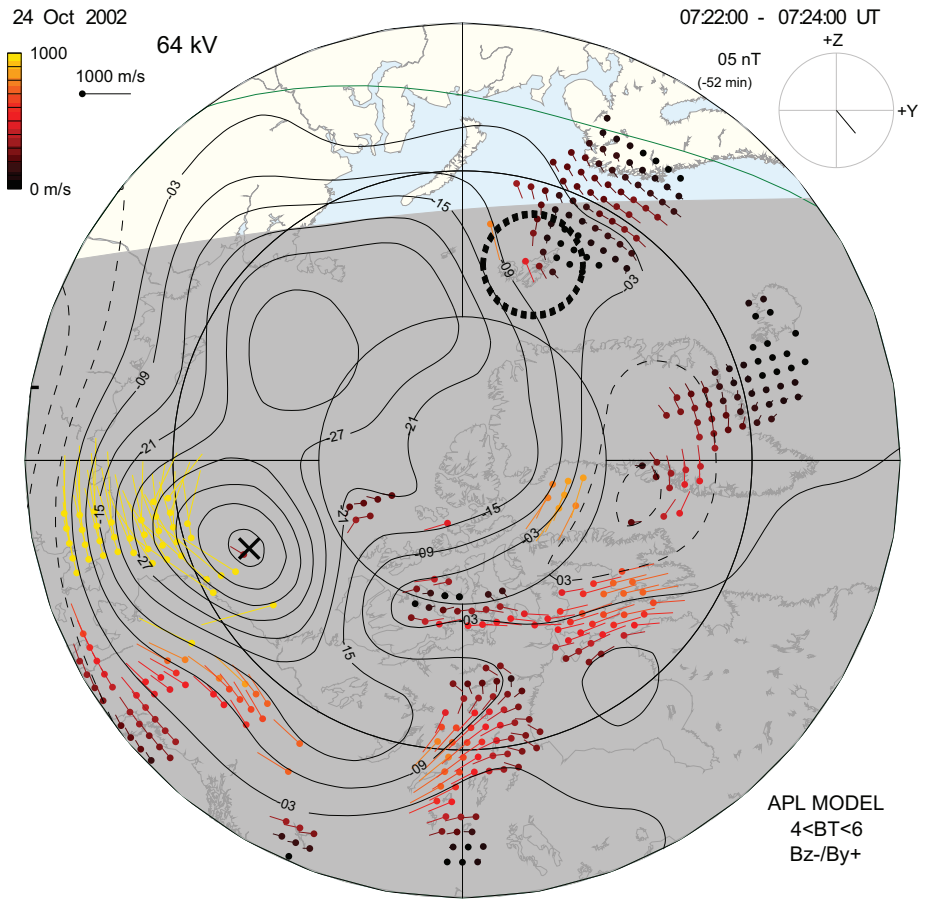

Figure 5.15: SuperDARN coverage above Svalbard during event 2 on 24 October 2002. The event starts at 07:22 UT and ends two minutes later at 07:24 UT. Svalbard is indicated by a black circle on the maps.

Event 2 is shown in figure (5.15). The coverage above Svalbard during this event is good, but only in a limited area to the south. It shows very low velocity and thus, this might be regarded as groundscatter making it less reliable. This is a very brief event, lasting for approximately 2 minutes. From this map, it is not possible to predict from where the plasma material has traveled, and to where it will travel. From the IMF data presented above, see figure (5.14), the IMF B_y component is strongly positive during the event and the convection pattern is therefore dominated by a large afternoon cell and a smaller morning cell, as described in section (2.7.3).

Event number 3, is the only well defined patch on this day, and the SuperDARN coverage from this event is shown in figure (5.16). The figure shows that

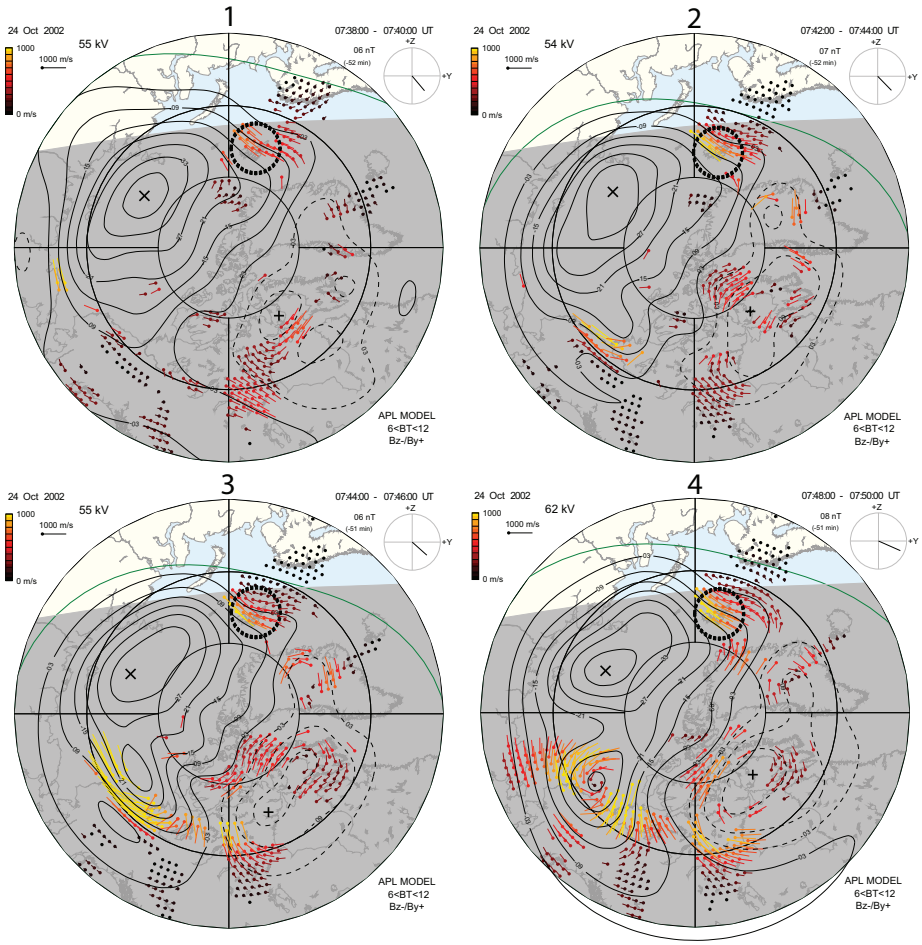

Figure 5.16: SuperDARN coverage above Svalbard during event 3 on 24 October 2002. The event starts at 07:39 UT and ends 11 minutes later at 07:50 UT. Svalbard is indicated by a black circle on the maps.

the coverage has increased from the previous event, but it is still restricted to a limited area above Svalbard. The data can no longer be regarded as ground-scatter, and shows high velocity above Svalbard which increases as the end of the event approaches. The velocity continue to be rather high in a limited area above Svalbard (not shown in this figure) until approximately 11:00 UT. Like the events presented previously, this event is dominated by a strong B_y component, and the flow is dominated by a large afternoon cell and a small morning cell, as described in section (2.7.3). It is difficult to predict where the extreme densities originate from on these convection maps, but it seems that they are coming from the sunlit area, see discussion of the results below.

5.2.4 Tracing - where did the extreme densities originate from?

The program *trace20021024.m* performs the tracing procedure described in section (4.3.1), while the program *plot20021024.m* plots the result. The programmes are to be found in appendix B, in section (9.1.4) and in section (9.1.5). Event 2 and 3 in table (5.2) where traced. The tracing result from this day seems reasonable, see figure (5.17(a)) and figure (5.18(a)), despite that the coverage of SuperDARN convection data is dominated by model data, see figure (5.15) and figure (5.16). The aim with this case study is thus to see if the tracing still works with less SuperDARN coverage in the polar cap, and how the path is affected.

Event 2: 07:22 - 07:24 UT

Figure (5.17(a)) shows the tracing of event 2 which starts at 07:22 UT in a magnetic grid. The extreme density event is traced two hours backward and two hours forward in time, with ESR as the starting position. Every half hour is displayed on the figure together with the locations at 07:22 UT of the EISCAT Svalbard Radar (ESR), Bjørnøya (BJN), Tromsø (TRO), and Ny-Ålesund (NYA). With the exception of a limited area above Svalbard, only model data exists for this day. Though, the result seems after all reasonable. No stagnation is observed and the figure clearly shows that plasma is transported from a solar EUV ionized plasma region into the polar cap. The distance between the dots gives an indication about the flow velocity. Small distance means low velocity, while larger distance means larger velocity. It is thus clear from the maps that the motion is stepwise across the polar cap with the highest velocity between 07:00 and 07:30 UT. The reliability of this tracing is discussed below in section (5.2.6.)

Figure (5.6(b)) shows the magnetic azimuth and the flow velocity at which the enhanced density travels across the polar cap. The magnetic azimuth is fairly constant, which indicates that the enhanced plasma follows a quite straight path. The flow velocity is on the other hand rather fluctuating, and fluctuates from almost zero to 1000 m/s with an average around 250-300 m/s. The patch material will because of the varying velocity, travel across the polar cap in a stepwise motion, which indicates flux transfer events. See discussion in section (6.2).

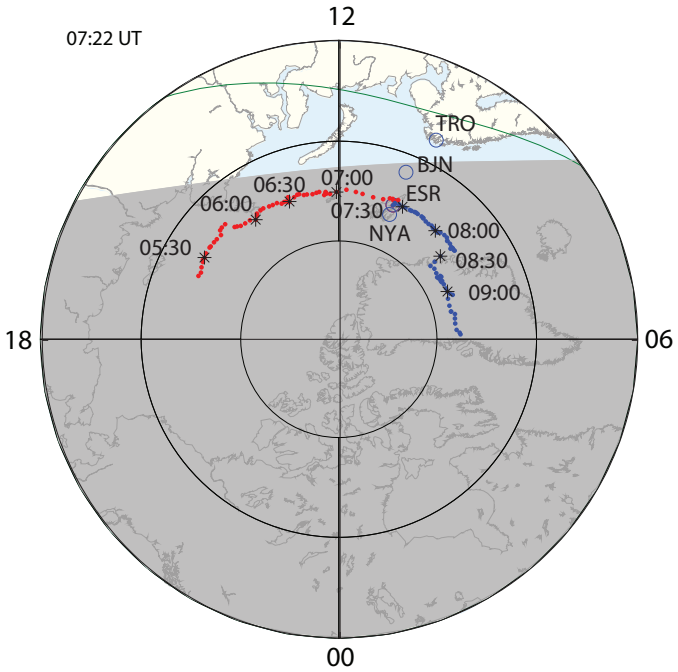

(a) The result of the tracing of event 2 in magnetic coordinates. The map shows the situation at 07:22 UT.

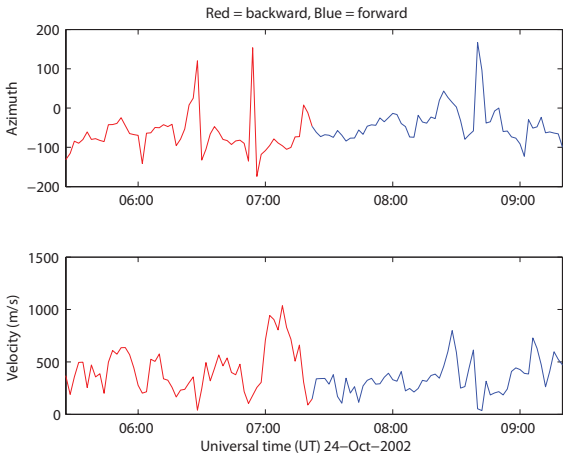

(b) Magnetic azimuth and flow velocity during the tracing. The transition between red color and blue color indicates where the extreme density event is first detected by ESR, that is at 07:22 UT.

Figure 5.17: a) The result of the tracing of the extreme density event 2, where magnetic coordinates are used. Two hours forward in time (shown in blue color) and two hours backward in time (shown in red color) from 07:22 UT have been used for the time of tracing. The locations of the EISCAT Svalbard radar (ESR), Bjørnøya (BJN), Ny-Ålesund (NYA), and Tromsø (TRO) at 07:22 UT are labeled on the figure. Magnetic noon is at the top. The solar terminator is shown with grey shading. b) Magnetic azimuth and flow velocity for event 2 on 24 October 2002. Red color indicates the tracing backward in time, while the blue color is indicating the forward tracing. Note the fluctuating velocity.

Event 3: 07:39 - 07:50 UT

Figure (5.18(a)) shows the tracing of event 3 which starts at 07:39 UT. Also here, two hours is used for the tracing both backward in time, and forward in time. ESR is the starting position. Every half hour is displayed on the figure together with the geographic locations at 07:39 UT of the EISCAT Svalbard Radar (ESR), Bjørnøya (BJN), Tromsø (TRO), and Ny-Ålesund (NYA). With the exception of a limited area above Svalbard, only model data exists for this day, but the result seems reasonable like the previous event. Stagnation is not observed and the figure clearly shows that plasma is transported along a convection streamline into the polar cap. The distance between the dots gives an indication about the flow velocity. Small distance means low velocity, while larger distance means larger velocity. From the maps, the motion seems to be stepwise across the polar cap with the highest velocity between 07:00 and 07:30 UT, and after 09:00 UT. A discussion of the reliability of this tracing is found in section (5.2.6).

Figure (5.6(b)) shows the magnetic azimuth and the flow velocity at which the enhanced density travels across the polar cap. The path doesn't fluctuate much, since the magnetic azimuth is fairly constant. The flow velocity fluctuates from almost zero to 1000 m/s, with an average around 250-300 m/s. The patch material will because of the varying velocity, travel across the polar cap in a stepwise motion, and following a straight path over the polar cap due to the steady magnetic azimuth. The varying velocity is an indication about flux transfer events. For discussion, see section (6.2.)

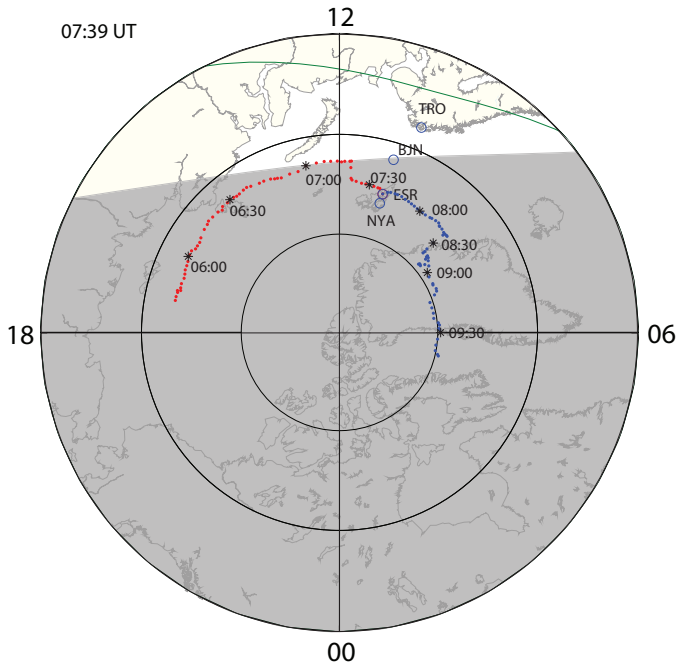

(a) The result of the tracing of event 3 in magnetic coordinates. The map shows the situation at 07:39 UT.

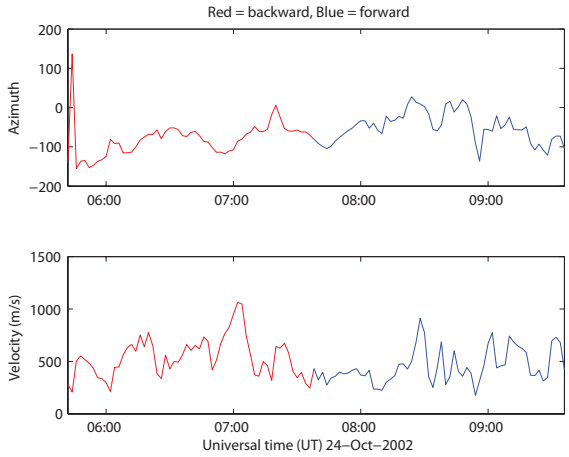

(b) Magnetic azimuth and flow velocity during the tracing. The transition between red color and blue color indicates where the extreme density event is first detected by ESR, that is at 07:39 UT.

Figure 5.18: a) The result of the tracing of the extreme density event 3, where magnetic coordinates are used. Two hours forward in time (shown in blue color) and two hours backward in time (shown in red color) from 07:39 UT have been used for the time of tracing. The locations of the EISCAT Svalbard radar (ESR), Bjørnøya (BJN), Ny-Ålesund (NYA), and Tromsø (TRO) at 07:39 UT are labeled on the figure. Magnetic noon is at the top. The solar terminator is shown with grey shading. b) Magnetic azimuth and flow velocity for event 3 on 24 October 2002. Red color indicates the tracing backward in time, while the blue color is indicating the forward tracing. Note the fluctuating velocity.

5.2.5 Tomography

There were no suitable tomography pass for the period of extreme density events on this particular day. Therefore, the tomography map at 11:23 UT is presented because it reveals the possible source of the plasma material. High densities of $1 \cdot 10^{12} m^{-3}$ is revealed on the map between 62 and 64 MLAT and between 72 and 77 MLAT. This on the other hand, doesn't agree with the results of the backward tracing. This map thus confirm the theory that the enhanced densities originate at sunlit areas where solar EUV ionization occur. From the path of the tracing, the plasma densities seem to follow a convection streamline past the sunlit area, and traveling toward the nightside. This result is questionable due to model data in this area, and due to the possible source region shown on the tomography map. For further discussion, see section (6.2).

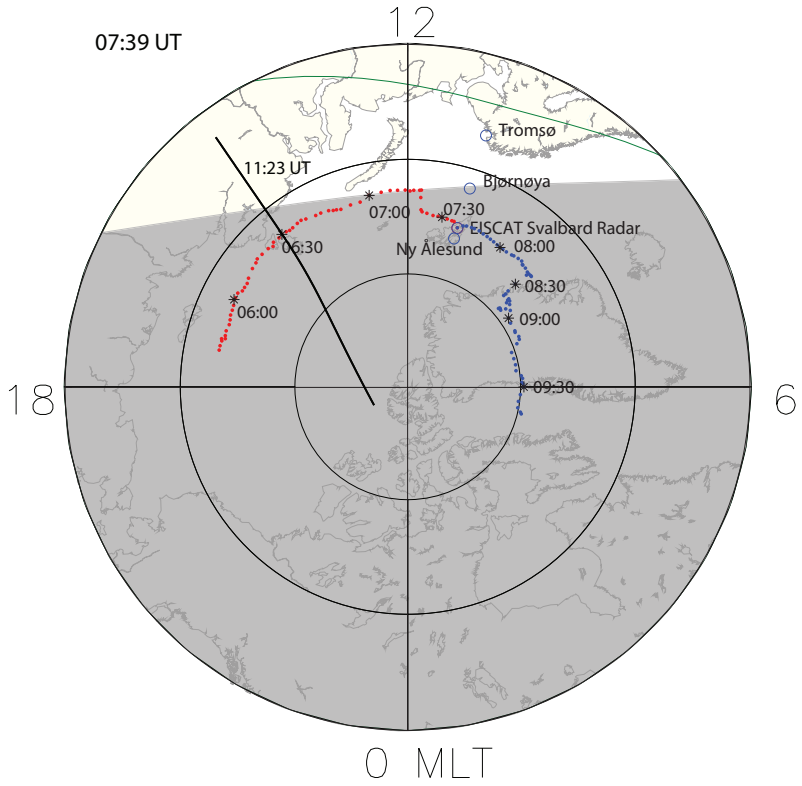

(a) The tomography pass at 08:46 UT on 24 October 2002. The map shows the situation at 07:39 UT.

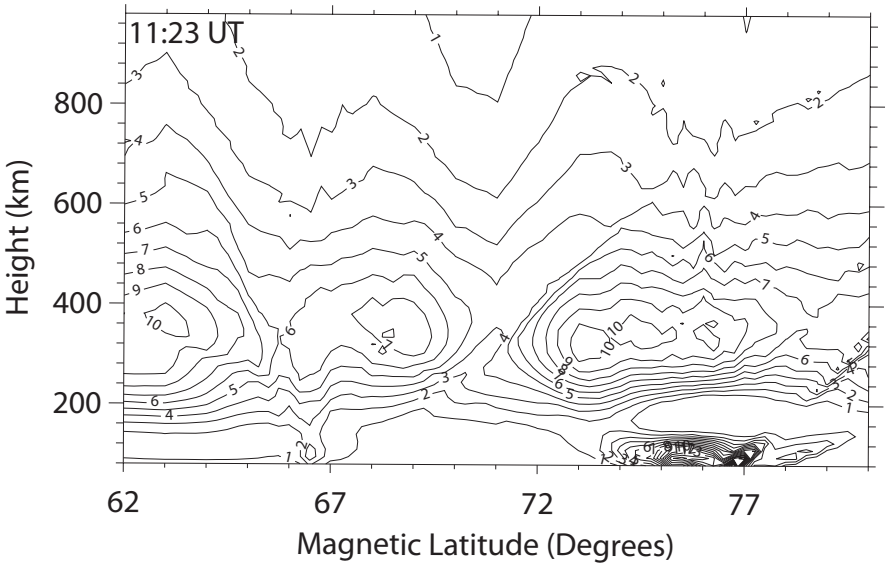

(b) The tomography map at 11:23 UT given in magnetic coordinates. The map is provided by Eleri Pryse.

Figure 5.19: The best suitable tomography pass at 11:23 UT for 24 October 2002.

5.2.6 Discussion: How reliable are these results?

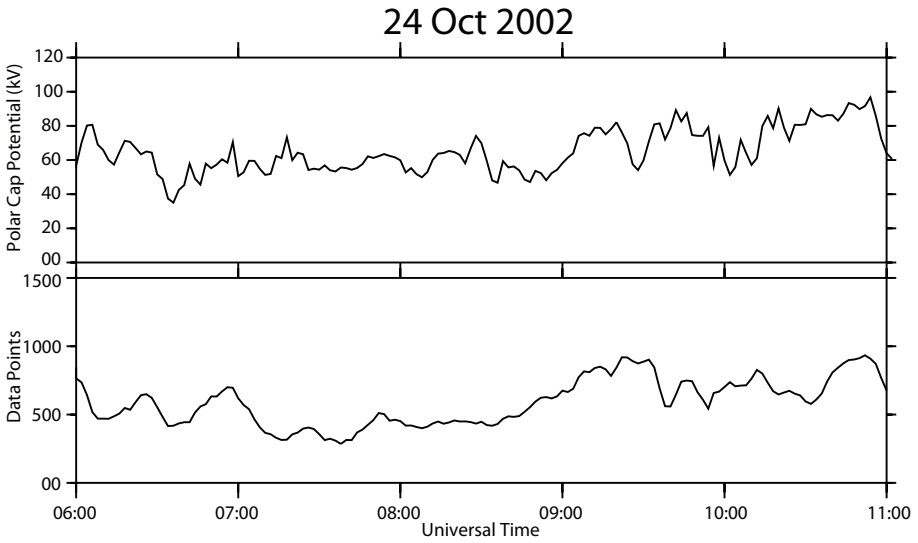

Figure 5.20: The upper panel shows the SuperDARN polar cap potential versus universal time on 24 October 2002, while the second panel shows the number of data points in the SuperDARN maps.

Events 2 and 3 on 24 October 2002 were traced with our tracing method. Event 2 is a relative brief event with approximately 2 minutes duration, while event number 3 last for 11 minutes. The very brief events with only one data dump where not usable for the tracing due to their lack of continuity. Unlike the cases on 06 February 2001, the cases from this day don't seem to stagnate, even though there is almost only model data available on this day. This is most likely due to the models used by SuperDARN, see discussion in section (6.3), and the stable IMF B_y in the whole time interval investigated. The patch material seems to follow a convection streamline backward in time, and due to model data only, the reliability of the tracing from this day is rather uncertain. When comparing with the tomography map at 11:23 UT this day, we find densities around $10^{12}m^{-3}$, which is most likely from the source region in the sunlit ionosphere at subauroral latitudes. The backward tracing before 06:30-07:00 on event 2 is thus questionable. The same applies to event 3. The backward tracing before 07:00 UT is not reliable due to the source region most likely being in the sunlit ionosphere at subauroral latitudes, as can be seen on the tomography map at 11:23 UT in figure (5.19).

The upper panel of figure (5.20) shows the polar cap potential based on the SuperDARN model. It gives an indication about the expansion of the polar cap and how strong the solar wind E-field is, see equation (3.2). The lowermost panel in figure (5.20) shows the number of data points in the SuperDARN maps. This gives us an indication about the reliability of the tracing, since more points lead to a more accurate result. The data coverage on this day is not so good as the previous case, as expected due to about half the number of data points

compared to 06 February 2001, see discussion in section (5.1.6). The polar cap potential is also substantially lower with some fluctuations. This day gives more questionable results than the previous case.

The Sondrestrom incoherent scatter radar was not in operation this day, so no data was available to be compared with the data from this case study [personal communication, Anja Strømme].

Chapter 6

Discussion

Two long runs of the EISCAT Svalbard Radar (ESR), in February 2001 and October 2002, have been analyzed with respect to occurrences of extreme densities in the polar cap. Detailed simultaneous observations of convection and plasma densities were examined to study the possible sources of patch material. High temporal and spatial resolution was needed and also an understanding of how the observations are related. From the two case studies, an understanding of why, when and from where these extreme densities originate was searched for.

The main results from the investigations are briefly summarized below and brought up for discussion in this chapter. Topics to be covered are structures in the high density plasma, the IMF dependency of the extreme density events, Solar EUV ionized plasma, the signature of Flux Transfer Events, the possible source regions of the enhanced plasma densities, and the reliability of the method used to perform the tracing.

- The extreme density events occur in a regular pattern around magnetic noon consistent with solar wind controlled transport of EUV ionized plasma across the polar cap from day to night.
- Plasma is transported from a solar EUV ionized plasma region into the polar cap, which means that there exists systematic intake of solar EUV ionized plasma in the cusp inflow region.
- The extreme density events follow the statistical convection pattern across the polar cap.
- The intake of high density plasma which is drawn into the polar cap through the cusp inflow region is independent of IMF B_y [Moen et al., 2008].
- All events studied were dominated by IMF $B_y > 0$.
- All events investigated seem to enter the polar cap from postnoon.
- The flow speed is highly variable, supporting the transient reconnection mechanism [Lockwood and Carlson Jr., 1992].

6.1 High density dayside plasma structure

The high density plasma structure can be divided into two different regions, that is nightside structures and dayside structures. Only dayside structures are studied in this thesis. The movement of nightside structures has been studied by airglow observations by Njål Guldbrandsen [2006].

6.1.1 Occurrence of extreme densities

February 2001 was in a period of solar sunspot maximum, and all days show extreme densities around magnetic noon. October 2002 shows extreme densities in the magnetic noon region in 60% of the days. Although this thesis investigates too little data to look for seasonal variations, we investigate the occurrence of extreme densities around solar maximum, and it appears that the extreme densities have very high frequency during solar maximum and are therefore most likely to decrease in frequency as we approach solar minimum.

The duration of the extreme density events turned out to be rather varied. Single detected events (the events lasting one data record only) constitute the largest part of the statistics. They occurred approximately 60 times in the data from 2001 and 40-45 times in the data from 2002. A possible reason is the extreme density event moving in and out of the radar beam. In some cases, the electron density value varies very close to the extreme density limit, and thus some densities are registered just below the limit and some just above. This leads to disjointed events, and thus brief events of extreme densities.
Since the brief events are more frequent than the long duration events, it is likely that the brief events lasting < 10 minutes are indications of potential patches. This was however not the case. The long duration events from 06 February 2001 where the only events this day that satisfied the definition of a patch. The definition of a patch is that the density inside a patch must be at least 2 times the density surrounding it, and the area is between 100 and 1000km [Buchau et al., 1983; Weber et al., 1984; Crowley et al., 2000]. The two patches can easily be found in figure (5.1), where they are indicated by two arrows. Since most of the observed events can not be defined as patches, one possibility might be that the radar observes a part of the TOI that has not yet been cut.

For the two cases on 06 February 2001 it seems that the longer the duration of the events are, the higher the detected electron density is. This is however very little data to know if this is the case in general. From the events on 24 October 2002, there is no clear connection between duration and maximum density of the events, but also here the highest densities detected are from the longest duration event. These high densities may be closely linked to the flow speed across the polar cap, since the convection velocity seems to increase in accordance with the observed pulses in the polar cap potential, see figure (5.11). This may be because the very rapid convection might be associated with the expansion of the polar cap, and when the polar cap is expanding, the flow pattern reaches further equatorward. The solar EUV ionization is stronger the more south in latitude we go, since the sun light intersects the ionosphere at a steeper angle, see section (2.6.1). From the backward tracing, a correlation is seen between the density and the tracing. Event 4 on 06 February 2001 could not be compared

with the other events, due to the stagnation in the backward tracing, but event 5 from 06 February 2001, and event 2 and 3 from 24 October 2002 could be compared. If we take into consideration that the tracing is not truly reliable during the entire tracing, see section (5.1.6) and section (5.2.6), it seems that the backward tracing of event 5 from 06 February 2001 reaches further equatorward than the events from 24 October 2002. If we see this in the context of the discussion above, event 5 has the highest detected electron density. It thus seems that there may be a connection between the expansion of the polar cap and the densities observed, further suggesting that the plasma came from a subauroral reservoir [Foster et al., 2002, 2004].
When ESR observes the high plasma densities, the convection velocity can decrease during the event, as can be seen in figure (5.5). In this case, the high density plasma has already entered the polar cap, and will maintain its high F-region density as it convects across the polar cap, as observed by Pedersen et al. [2000]. One way that might explain why the convection velocity decreases is counteracting co-rotation and convection electric fields [Foster, 1993; Pinnock et al., 1995; Rodger, 1998]. The plasma is then called a stagnated plasma, since the Earth and the solar wind driven convection pattern rotate separate ways. Eventually the stagnated plasma is extruded by the convection electric field, through the cusp and across the polar cap.

Foster [1993] investigated the K_p dependency of enhanced electron densities, and found storm-enhanced plasma density (SED) for almost all K_p levels, even for K_p as low as 2, and thus no direct dependence related to enhanced electron density events. This was also investigated and confirmed by Qiu [2006] in his master thesis study. When K_p is low, the oval contracts poleward and Svalbard is located south of the oval, measuring subauroral cusp region. This has however not been investigated in this thesis.

The two patches observed on 06 February 2001 were two cold plasma patches. The electron temperature was low, i.e the ESR was taking measurements outside the oval at that time. Since the temperature is low, electron cooling is present, see section (2.6.3). On 24 October 2002, T_e and N_e were simultaneously high during the observed events, and thus the ESR was inside the auroral oval. The temperature is high due to electron heating which is present due to soft particle precipitation in the oval, see section (2.6.3) and section (2.6.4). The question is therefore whether particle precipitation affected the observed extreme densities.

6.1.2 Solar EUV ionized plasma vs particle precipitation?

All electron density enhancements can basically be caused by two sources; intake of solar EUV ionized plasma, and particle precipitation in the auroral oval. What is the degree of plasma enhancement due to particle precipitation? It is hard to measure the particle precipitation over a large area since satellites and all sky camera's have small fields of view. There was also no optical data for our events in February and October, because the southern horizon over Svalbard was contaminated by scattered sunlight, and optical instruments could not be used. Radars have difficulties to distinguish between the different types of precipitation. However, the effect of particle precipitation has not been investigated here. This thesis focuses on a period of solar maximum, and thus the

extreme density limit is set to $10^{12}m^{-3}$. By using this high threshold we exclude the patches formed exclusively by particle impact ionization as described by MacDougall and Jayachandran [2007] around the morning sector, and by Kelley et al. [1982] in the cusp. It is very unlikely that extreme densities larger than $1 \cdot 10^{12}m^{-3}$ could have been produced locally by particle precipitation e.g. [Oksavik et al., 2006b], so the amount of local precipitation will therefore be fractional compared to the solar EUV ionization. Ionization below $\approx$ 250 km will die away rather quickly due to recombination [Walker et al., 1998]. This means that the source of electron density enhancements in the two months investigated is dominated by intake of solar EUV ionization on the dayside. Earlier studies have also found that the possible source region must include ionization from the sunlit ionosphere, e.g Weber et al. [1984].
For this study, both case studies show plasma coming from the postnoon sector. Foster [1993] showed that the postnoon plasma can co-rotate, stagnate, and then enter the return flow towards the cusp inflow region during disturbed conditions in the rest frame of the Earth. Large ionization will then build up because of this unusually long exposure to solar EUV production (storm enhanced density, see section (2.9)).

6.1.3 IMF dependency

The IMF B_y component is positive and stable for both days investigated, see figure (5.3) and figure (5.14). The exception is a 10-minutes negative turn at approximately 06:30 UT on 06 February 2001. 24 October 2002 have two negative turns at 08:45 UT and at approximately 10:20 UT, and two turns that barely reach a negative value before becoming positive again. For both days, the B_y value was varying around 10 nT. A relation between IMF conditions for the extreme density events was investigated for the two days. The result was that the overall intake of patch material is not sensitive to neither of the IMF components. The location of the ESR is so close to magnetic noon and the dayside terminator that it is insensitive to the sign of IMF B_y regarding intake of high electron density drifting over the radar. This result is consistent with Rodger et al. [1994a] and Moen et al. [2007, 2008]. The trajectory of its motion is however strongly B_y dependent, and the cusp inflow region will be shifted postnoon for positive values of IMF B_y in the northern hemisphere, see section (2.7.3). The uppermost panel in figure (2.15) and the two panels to the right in figure (2.17) show the situation for the convection pattern when IMF B_y is positive. The convection pattern is dominated by a large postnoon cell and a smaller prenoon cell, see section (2.8).

The correlation between the duration of the events versus their corresponding IMF was characterized by stable negative IMF B_x, stable positive IMF B_y and fluctuating IMF B_z component for all of the longer duration events. The IMF B_z component was fluctuating around zero for the longer duration events on 06 February 2001, while it was turning from negative to positive for the long duration event on 24 October 2002.

6.2 Source regions and plasma transport

By locating and investigating the source region of extreme plasma density, a better understanding of the ionospheric structure can be found. The possible source and the transport mechanisms have been studied for several years, and there are probably more than one source region causing F-region plasma enhancements in the polar cap. The potential source regions brought up for discussion here, were presented in section (2.9).

Only two of the events from 06 February 2001 could be defined as isolated patches, see section (6.1.1). According to Sojka et al. [1993], the origin of the patches can be equatorward of the cusp region, within the cusp region, or a combination of both. The most likely source region which can be found from the results presented in chapter (5) and the above discussion, is solar EUV ionization from sunlit subauroral latitudes. This is consistent with several studies that have reported regions of enhanced F-layer plasma convecting from the solar-illuminated dayside into the cusp/throat region, e.g Buchau et al. [1985]; Weber et al. [1984]; Foster and Doupnik [1984]; Kelly and Vickrey [1984]; Pinnock et al. [1995]; Carlson et al. [2006]; Moen et al. [2006].

Structures in the dayside magnetopause which are caused by bursts of transient reconnection will cause variation in for instance the flow velocity. Transient magnetic reconnection takes place in a series of discontinuous events known as Flux Transfer Events (FTEs) at the subsolar magnetopause, see section (2.7.2). Fluctuating flow velocity was observed for all events both days, and the patch material will thus move with a stepwise motion, not a constant speed across the polar cap. Transient magnetic reconnection is probably the dominant mechanism that transport the patch material from the cusp inflow region across the polar cap to the nightside [Lockwood and Carlson Jr., 1992; Carlson et al., 2002, 2004, 2006]. Such magnetopause signatures typically occur with a 2-20 minutes repetition period [Elphic, 1989], which means that the average is about 7 minutes. This is roughly consistent with the observations from this thesis. Here the typical time scale varies in range from approximately 5 minutes to approximately 30 minutes. If the FTEs occur frequently over a period of time, they may be enough to drive the global convection [Cowley and Lockwood, 1992; Moen et al., 1995], as shown in figure (6.1).

Figure (6.1) illustrates the generation of polar cap flow and patch formation by transient reconnection. Snapshot (1) shows the situation for $t = 0$ where the merging gap is ab, and the solid line is the high density contour. (2) At $t = 2.5$ min., the merging gap (ab) starts moving equatorward. At snapshot (3), the flow has increased and near its center the merging gap has moved furthest, and the flow starts to move high density plasma equatorward of the solid line poleward. Then the reconnection burst ends, and the merging gap returns poleward with the local plasma flow. As the flow decays, the distortion of the plasma continues in (4) and (5) resulting in an equilibrium state with the new amount of open flux for the magnetosphere-ionosphere system. By $t = 15$ min. low density plasma has returned sunward of the high density plasma by the flows. In snapshots (9)-(12) a new reconnection burst occurs, producing a second patch. When the flow is driven by this start-stop manner, the convection pattern is

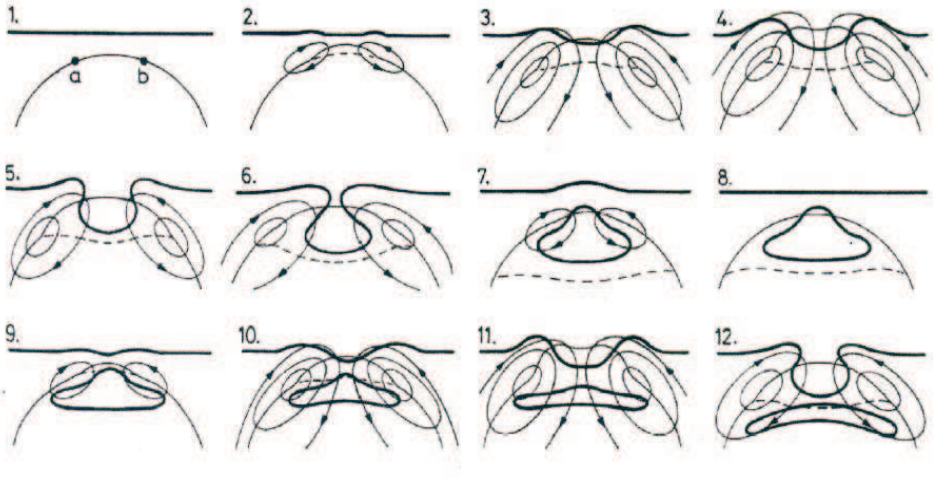

Figure 6.1: Sequence of flow snapshots separated by 2.5 minutes. A high plasma density contour is shown as the solid line, and the merging gap (ab) migrates equatorward from panel 1. Snapshot 1-8 shows one reconnection pulse, see description in the text. Figure from Lockwood and Carlson Jr. [1992].

thought to expand equatorward and then contract [Lockwood and Carlson Jr., 1992]. When the IMF B_y component is stable, the plasma jets associated with these flux transfer events are fastest [Rodger, 1998].

This study thus confirms that extreme electron densities are likely to originate from a solar illuminated area at sub-auroral latitudes. From here the patch material is transported into the polar cap under the influence of the convection pattern, and most likely driven by transient magnetic reconnection events [Carlson et al., 2006].

6.3 The tracing method

This thesis has described a method which traces enhanced electron densities both backward and forward in time. The model uses actual SuperDARN data in areas with good SuperDARN coverage, and model data in areas with no available data (since the SuperDARN network does not cover the entire polar cap). The SuperDARN data structure is described in section (3.1.3). The additional data from the statistical convection model makes the resulting path of the backtracking of the extreme densities more uncertain, and from the result in the previous chapter it is clear that the method works best for areas with good radar coverage. The areas with model data only may destroy the accuracy of the method. Which model is used is indicated at the bottom right in the convection maps, see for instance figure (5.15) where the APL model is $-B_z/+B_y$. SuperDARN uses different models of convection depending on the current IMF conditions. If the solar wind is unavailable, it is taken from a

default pattern characteristic of average convection, i.e. weak two cell convection pattern [Ruohoniemi and Baker, 1998; Shepherd and Ruohoniemi, 2000]. Manual checking whether the result is based on real data or model data is thus needed to verify the accuracy of the path traced. The events on 24 October 2002 are dominated by model data, but since the IMF B_y is stable, the variation is not so large in the convection pattern, and the result seems reasonable. The resulting path is however questionable since there is mostly model data for both the backward and forward tracing. In periods with only model data, we can not know how expanded the polar cap is. The reliability of the method is described in section (5.1.6) and section (5.2.6) in the previous chapter.

Figure (6.2) shows a sequence of HF backscatter power measured by the SuperDARN radar in Finland. The HF backscatter power is created by ionospheric irregularities that seem to be found inside the high density plasma. The time interval from 07:19 UT to 08:39 UT covers the two long duration events investigated on 06 February 2001. The dotted circles indicate what might be the high density events number 4 and 5. Event 4 starts at 07:23 UT and ends at 07:40 UT, while event 5 starts at 08:00 UT and ends at 08:19 UT. The red dotted circles indicates when the extreme densities are detected by the ESR beam.
By comparing the movement of the high density plasma in figure (6.2) with the tracing of high density plasma performed in the previous chapter (see figure (5.7(a)) and figure (5.6(a)), we can see if the measured results are in accordance with each other. Both events 4 and 5 follow a path toward the northern part of Greenland. The panel which shows the situation at 07:49 UT might have registered the movement of event 4 toward Greenland, and this high backscatter power can be seen as indicated by the black arrow. Event 5 can more easily be seen traveling towards Greenland in the three last panels. The movement is indicated by black arrows. This event of enhanced plasma density is expected to meet the Greenland east coast at approximately 08:30 UT according to the tracing path. This corresponds well with the panel at 08:29 UT, where the high backscatter power just reached the coastline. The high density plasma observed with the ESR matches well with the high backscatter power observed with the SuperDARN Finland radar. As discussed in section (5.1.4), the tracing is reliable one hour back in time for event 5. This result thus further support that the resulting path of the tracing is reasonable from 07:00 UT until 09:00 UT for this particular event, and that the high densities observed with the ESR can be found in the SuperDARN data as well as regions of enhanced HF backscatter power.

6.3.1 Stationary patches

The method can not guarantee for the accuracy of the result when there is only model data present. Aside from this, figure (5.8) shows an interesting result. Events number 2 and 3 in the figure show possibilities for stationary patches. That is plasma that remains in the same position over an unknown period of time in an area of ongoing precipitation. After some time, the patch will start drifting again. This indicates that the motion of the convection is not continuously driven. When the patch enters the polar cap, it may stop its movement for a period of time, as shown in the figure. Meanwhile, a new patch enters the polar cap and bypasses the older patch, before it leaves the polar cap

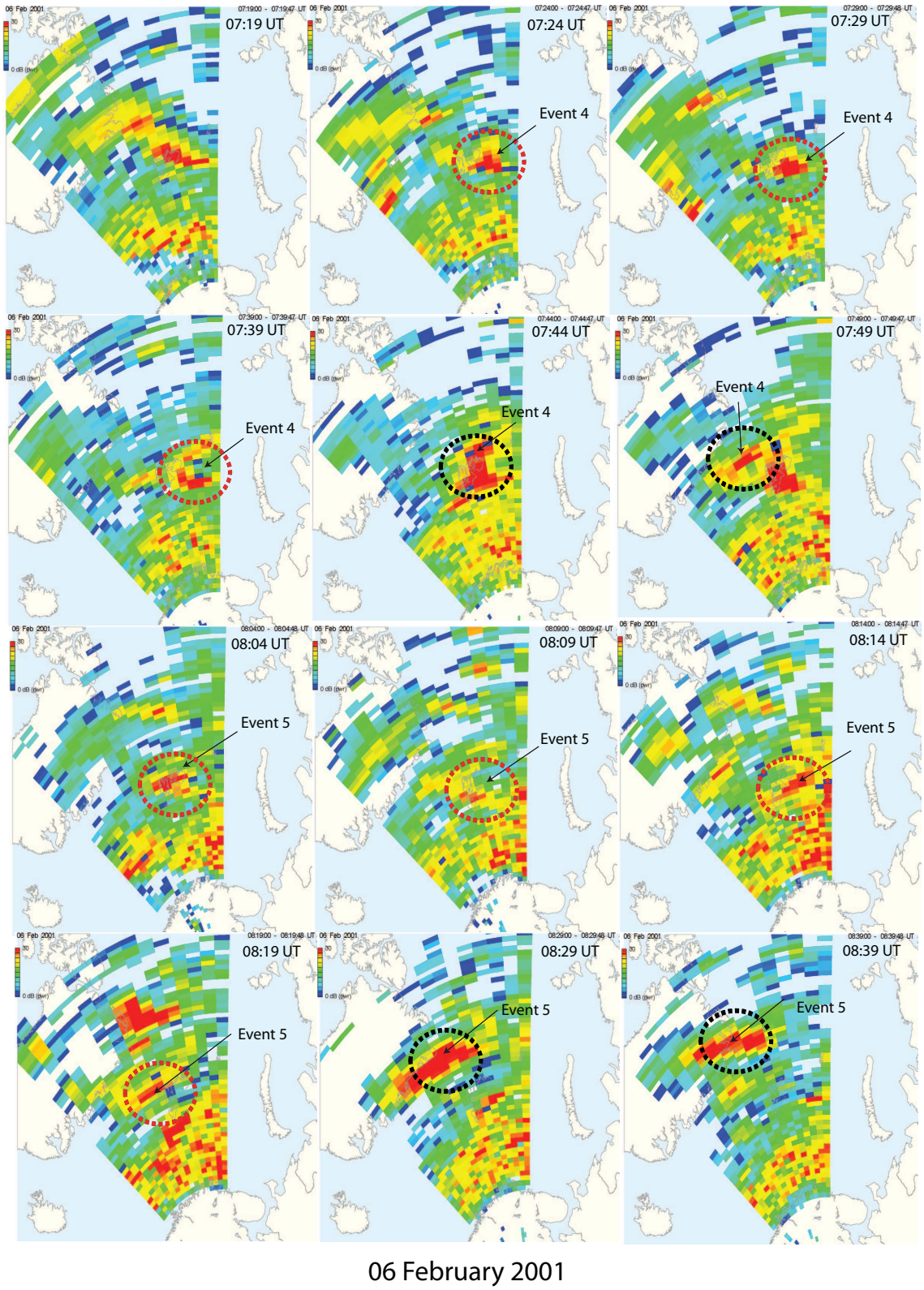

Figure 6.2: HF backscatter power measured by the SuperDARN Finland radar. The dotted circles indicate what might be the high density events on 06 February 2001. The red circles indicates when the high densities events are seen by the ESR radar beam.

at an earlier stage than the first patch. This is a little explored phenomenon in the polar cap, and so we can't know for certain that this is actually the case. There is however a possibility that the first patch that enters the polar cap is not the first one to leave, which is an intriguing idea.
What can make a parked patch to drift again? One possibility is the IMF B_y component. A stable B_y component which suddenly makes an abrupt change from positive to negative, and then turns positive again, can have triggered the effect. Such a change is to be found in the IMF data for 06 February 2001. An abrupt change in the IMF B_y component occurs at approximately 06:30 UT. From the path in the figure, the parked patch seem to drift again just after 07:00 UT. Due to these possible stagnating patches, space weather forecasting becomes a more complex and challenging task.

6.3.2 Comparison with other methods

Few attempts have been made, trying to trace enhanced densities backward in time. Bust and Crowley [2007] made a trajectory analysis based on convection patterns obtained from AMIE (Assimilative Mapping of Ionospheric Electrodynamics), see section 2.10. Bust and Crowley [2007] investigated a sequence of patches observed at the ESR (Svalbard) between 20:00 UT an 22:00 UT on 12 December 2001, and found that the patches originated in several different locations. Due to the uncertainties in the AMIE convection pattern, the uncertainty in the patch trajectory increases the longer we integrate backward or forward in time [Bust and Crowley, 2007]. Figure (6.3(a)) show one of their results where they started the trajectory analysis at ESR. The patch traveled from the morning side and arriving at Svalbard at 21:05 UT.
Figure (6.3(b)) shows the result from event 4 on 06 February 2001 which is observed at 07:23 UT (a different day). It shows the patch material coming from a sunlit area, which is a fairly reasonable result, but the opposite side of noon of the results from Bust and Crowley [2007]. But the data is from different days. The main difference between the methods is that our method is the first study to use actual velocity measurements of the convection to determine the tracing. This should be more reliable than the model used by Bust and Crowley [2007]. The advantage of using the AMIE technique, is that this method ingest huge amounts of high latitude data [Richmond and Kamide, 1988], and will thus be much more complex than the method we have developed. But as we have seen the SuperDARN coverage is the main limiting factor for our tracing method. However, this is expected to improve, as more SuperDARN radars are built.

6.3.3 Space weather

What do these results mean for space weather effects? The HF backscatter power shows that there exist irregularities in the high density plasma which most likely will effect communication and navigation in the polar regions [Weber et al., 1984; Buchau et al., 1985]. In order to predict the rate of irregularities in the polar cap, the electron density distribution needs to be known, and the convection pattern in high latitudes is needed to predict the patch motion. The high density plasma seems to travel with a stepwise motion across the polar cap, which makes space weather forecasting more challenging. Several mechanisms needs to be taken into consideration. First, the extreme densities depend on

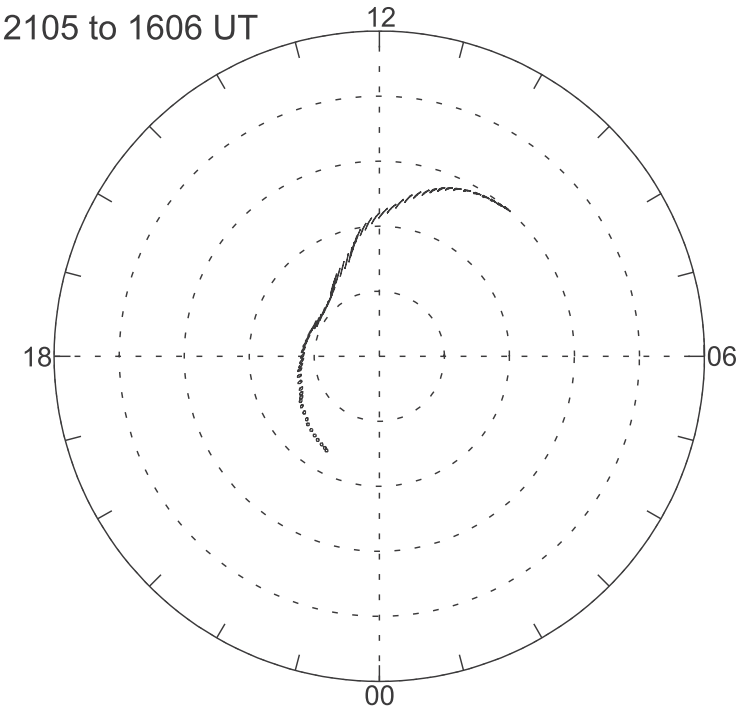

(a) The resulting path from the model developed by Bust and Crowley [2007]. Figure from Bust and Crowley [2007].

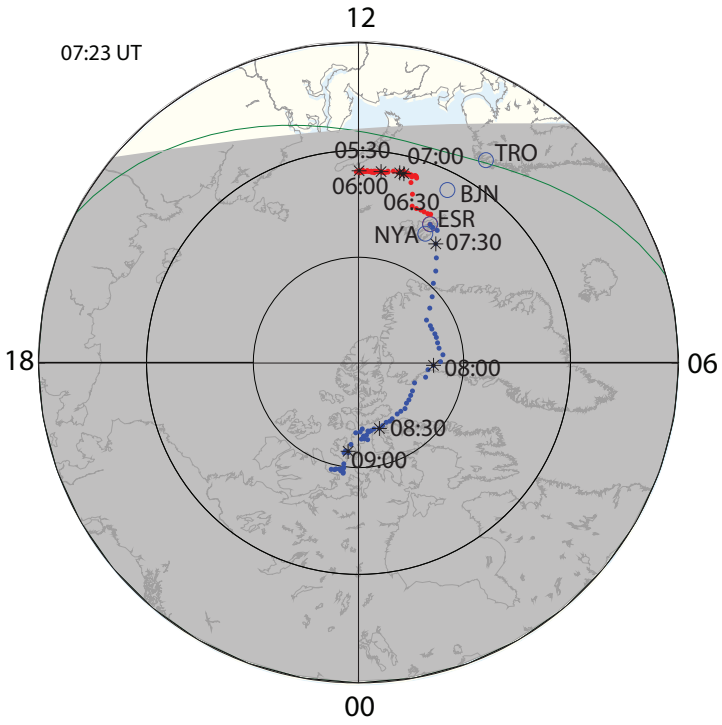

(b) The resulting path from our study.

Figure 6.3: Comparison of two models with the same purpose to track extreme densities in the polar cap. Please note that this is two different events on two different days. The two events are thus not comparable, but serves as an illustration.

the solar cycle and time of day. From this study, we know that they occur in the period around magnetic noon, and very frequently during solar sunspot maximum. Due to their stepwise motion, some of the events will in periods travel with very low velocity across the polar cap, and as suggested here in section (6.3.1), some of the events may even stop their movement for a period of time. This makes it difficult to predict when and for how long the extreme densities will be present in the polar cap. However, the resulting paths from the most reliable tracing show the extreme densities traveling from sunlit latitudes, across Svalbard and towards Greenland. The observations performed by ESR can thus work as a forecast for e.g. GPS users in Greenland, and provide them with a forecast approximately half an hour in advance. From Greenland and toward the US and Canada, the tracing can not be trusted with the available data coverage. But with the better data coverage that has come in the recent years (remember that our dataset is from 2001 and 2002), the ESR can most likely work as a forecast for these areas too, providing the users of navigation and communication equipment a forecast approximately one hour in advance. The result from this thesis will only contribute to a small fraction to the huge challenge of space weather forecasting is [Behnke et al., 1995]. Still our result has made a very important step forward, by combining data from multiple instruments in order to address a very complex problem. For example, our study has been the very first attempt to describe the motion of a polar cap patch in the frame of reference of the patch itself. The successful tracings we did in chapter 5 (see figures in section (5.1.4) and in section (5.2.4)) illustrates for the first time how a patch moves in steps across the polar cap. Previous studies of polar cap convection often look at the global picture, the large-scale convection of the entire polar cap. However, to fully understand the physics of a polar cap patch and its structuring processes, it is also important to study the patch in its own frame of reference, in a small volume that just encloses the patch. Only in this way can one discover the forces that are exerted on this volume, how the small patch moves relative to the surrounding plasma, how its motion changes direction, and whether the patch experiences any changes in its flow speed. In this way this thesis has shed new light at the bumpy ride a plasma parcel is experiencing on its way from subauroral latitudes, through the cusp inflow region, and across the polar cap. The flow speed is pulsed and highly variable both at subauroral latitudes, in the cusp inflow region, and in the polar cap. It is also clear from this study that other mechanisms that need to be included in a space weather forecast are the IMF components. The IMF conditions (strength and orientation) control how the plasma will be transported across the polar cap. In our case, both days where dominated by a strongly positive IMF B_y component. For other cases, the plasma might not travel across Greenland, as it did for our events.

Chapter 7

Summary and future work

In this chapter, all results are summarized in the first part, while the second part presents some ideas for the future work regarding improvements of the method we developed to track the motion of individual regions of high plasma density.

7.1 Summary and conclusion

Extreme density events ($n_e > 10^{12} m^{-3}$) in the polar cap have systematically been investigated using the EISCAT Svalbard Radar (ESR) and the SuperDARN HF radars. The main objective has been to check the extension of extreme electron densities in the polar cap using field aligned ESR observations, reveal their occurrence frequency and duration, and locate their possible origin. The extreme electron densities occurred in a more or less regular pattern around magnetic noon, consistent with the cusp inflow region near noon. The events varied a lot in duration, from less than 2 minutes to over 120 minutes. The brief events were significantly more frequent than the longer duration events, and only a few events could be defined as isolated patches. When the occurrence frequency and duration of the extreme densities were mapped, the IMF components were investigated for the various events. Both events were characterized by stable and strong IMF B_y components. Next, the possible high density plasma origin was investigated for two selected days using our tracing method. Finally, two events from 06 February 2001 and two events from 24 October 2002 where successfully traced two hours backward and two hours forward in time using the technique we developed.

All of the resulting paths from the performed tracing show plasma coming from a sunlit area near the cusp region. It suggest that the extreme density material originates from dayside ionization produced by solar radiation at lower altitudes. The high density material is transported through the convection throat region into the polar cap. It seems likely that the extreme electron densities are entrained in the high-latitude convection pattern and convect in a tongue of ionization (TOI) that extends from subauroral latitudes into the polar cap. Due to the observed pulsed convection events, it is likely that the extreme electron densities are transported across the polar cap by a transport mechanism where transient magnetic reconnection is a driving force, consistent with

Cowley and Lockwood [1992]. The flow speed was observed to be pulsed both in the subauroral zone, in the cusp inflow region, and in the polar cap.

The patch material seems to travel over the Sondrestrom radar in Greenland. The ESR can thus most likely work as a forecast for navigation and communication users in Greenland, Canada and the US. A forecast for when extreme densities occur at the ESR has not been found, other that we now know that the extreme densities occur most frequently around magnetic noon for the dayside. However, the current study shows that the enhanced density regions experience a very bumpy ride across the polar cap, which further complicates the problem of forecasting these events. More research is therefore needed.

7.2 Future work

The two months of ESR data investigated represents a substantial work load for a master thesis. However, larger amounts of continuous data sets will be available in the near future. The EISCAT Svalbard radar was participating in the International Polar Year (IPY) with radars in continuous operation covering a whole year of incoherent scatter radar data. By running these long duration modes, new knowledge can and will be discovered about e.g. the daily- and seasonal variations of the ionosphere. Normally the radar only operates for a few days at a time, and thus there is little historical long duration data to retrieve. The long duration runs used in this thesis are continuous, only disrupted by minor breakdowns caused by aircraft interruptions. The daily ionospheric activity can therefore be found. However, by using longer duration runs the seasonal variations can also be found. The data collected during IPY will indicate how much the data change from month to month, and in the future the year to year variation can also be found.

The data set is not good enough for studying the smallest high density structures, thus only the large scale structures have been studied in this thesis. To study for instance patch-formations in detail, better time resolution is needed. This data set is only able to identify patches, not study them in detail. EISCAT 3D is the next generation European Incoherent Scatter radar system currently being planned, and it will provide high resolution data which can be used to further study fine scale plasma structures, if it is built.

7.2.1 Improvements of the tracing method

There are a number of ways the method can be improved. Firstly, the accuracy of the model is determined by the available SuperDARN radar data in the polar cap. The number of radars in the northern hemisphere have increased significantly since 2001/2002, and the SuperDARN coverage in the polar cap has therefore been improved considerably in the recent years. See figure (3.5) for the coverage of radars in 2007. This development will make it easier to trace the extreme densities backward in time, since the method relies on real measured SuperDARN convection data, not model data.
PolarDARN is a relatively new set of radars in the northern hemisphere consisting of one radar located at Rankin Inlet (operating since May 2006) and

one radar located at Inuvik (operating since November 2007). These radars have overlapping fields of view, and their primary objective is to study the convection, the radio scattering conditions, and the field-aligned currents in the center of the polar cap and at the poleward edge of the auroral oval. At mid-latitudes three new radars have been developed since 2005; that is Wallops Island [Oksavik et al., 2006a], Hokkaido and Blackstone, and eight new radars will be built across the American continent in the next few years.

In addition to ESR, the extreme densities can also be traced from other locations in the polar cap, for instance from Sondrestrom in Greenland, AMISR (Advanced Modular Incoherent Scatter Radar), Millstone Hill and Resolute Bay. Millstone Hill is located at sub-auroral latitudes, and thus the radar might be located in the production area, which can give some very interesting results. Only the daytime patch material has been investigated in this thesis, but it would also be of interest to investigate how the nighttime patch material enters over Svalbard, and how frequently extreme densities occur during the night. Unfortunately the Sondrestrom radar in Greenland was not in operation on 06 February 2001 or 24 October 2002, so the ESR data could not be compared with the Sondrestrom data. The other American radars might have radar data from these days, but this was not investigated here. Although it has not been the focus of this thesis, the DMSP (Defense Meteorological Satellite Program) satellite, ionosondes in the polar cap and all-sky imagers for airglow could also be used for further investigations.

The tracing results have been checked manually against SuperDARN convection maps to know how reliable the resulting path is. This can be done automatically in the future. Also, removal of groundscatter in the data can be improved. The aim is to better distinguish between what is real measurements of ionospheric drifts and what is actually groundscatter, i.e echoes from the ground.

The AMIE technique was used by Bust and Crowley [2007] to track patches observed by ESR backward in time, see section (2.10) and (6.3.2). It would therefore be interesting to use the AMIE technique on the data set used in this thesis to see if the result is the same for the different methods. There is much undone work when it comes to think more globally on ionospheric processes, so there is a lot of interesting discoveries to be made within this field in the years to come. Right now we are in a period of solar minimum, but as we approaches solar maximum, see section (2.1), there will be more data available than in the previous solar maximum in 2001. It will be very exciting to repeat this study after the next solar maximum which is expected to arrive in a couple of years time, since the tracing will then be more reliable due to more datapoints, and less model data due to better coverage.

Chapter 8

Appendix A: Abbreviations

AACGM Altitude Adjusted Corrected Geomagnetic Coordinates

ACE Advanced Composition Explorer

ACF Autocorrelation Function

AMIE Assimilative Mapping of Ionospheric Electrodynamics

AMISR Advanced Modular Incoherent Scatter Radar

ASC Ace Science Center

AU Astronomical Unit

BJN Bjørnøya

BPS Boundary Plasma Sheet

CPS Central Plasma Sheet

DMSP Defense Meteorological Satellite Program

EISCAT European Incoherent Scatter

ESR EISCAT Svalbard Radar

EUV Extreme Ultra Violet

FAC Field-Aligned Current

FOV Field of View

FTE Flux Transfer Event

FWHM Full Width Half Maximum

GPS Global Positioning System

GSM Geocentric Solar Magnetic

GUISDAP Grand Unified Incoherent Scatter Data Analysis Program

HCS Heliospheric Current Sheet

HF High Frequency

HLBL High-Latitude Boundary Layer

IDA3D Ionospheric Data Assimilation Three Dimensional

IGRF International Geomagnetic Reference Field

IMF Interplanetary Magnetic Field

IPY International Polar Year

ISR Incoherent Scatter Radar

ISTP International Solar-Terrestrial Physics

LLBL Low-Latitude Boundary Layer

MAG Magnetic Field Experiment

MHD Magneto Hydrodynamics

MLAT Magnetic Latitude

MLON Magnetic Longitude

MLT Magnetic Local Time

MP Magnetopause

NYA Ny-Ålesund

OCB Open Closed Boundary

PBL Plasma Boundary Layer

PS Plasma Sheet

PSBL Plasma Sheet Boundary Layer

RF Radio Frequency

SAID Sub-Auroral Ion Drifts

SAPS The Subauroral Polarization Stream

SED Storm Enhanced Density

SuperDARN Super Dual Auroral Radar Network

SWE The Solar Wind Experiment

SWEPAM Solar Wind Electron Proton Alpha Monitor

TEC Total Electron Content

TOI The Polar Tongue of Ionization

TRO Tromsø

UHF Ultra High Frequency

UT Universal Time

UVI Ultraviolet Imager

VHF Very High Frequency

Chapter 9

Appendix B: Programme code

9.1 The Matlab programmes

The Matlab programmes used in this thesis are shown in the following subsections, and small comments are given after the % sign within the codes. The programme language for this master thesis is Matlab 7.7.0. The programmes were developed to work for both February 2001 and October 2002, but only one day is shown as an example for each programme since the programmes are identical. The days used as examples are the two case studies presented in chapter (5).
It has not been a priority to make the programs as effective as possible, since this was not necessary for the results of this thesis. If necessary, the code can be rewritten to make it more efficient for eventual further studies.

9.1.1 *ekstremverdi2001.m*

The programme *ekstremverdi2001.m* organizes the extreme densities from February 2001 according to onset time and duration, and the programme only takes in ESR data. The extreme densities are also plotted versus time for the various days, and an example of this is given in figure (4.2) in chapter (4). *ekstremverdi2002.m* is the similar programme which organizes the extreme densities from October 2002. This programme is not included here since the programmes are identical.

Listing 9.1: ekstremverdi2001.m

```
clc;
clear;

%Load files (20 files)
files = dir('*.mat');
for i = 1:length(files)
    a{i} = load(files(i).name);
end

for i = 1:length(files)
    a = load(files(i).name);

    %Data which are greater than 5e12, are replaced with NaN
    [f1, f2] = find(a.NE >= 5e12);
    for j = 1:length(f1)
        a.NE(f1(j),f2(j)) = NaN;
```

```
end

%Since extreme densities are defined to be higher than 1e12, values
%below this limit are not needed in the further analysis, and are
%therefore changed to NaN
[r1, r2] = find(a.NE < 1e12);
for h = 1:length(r1)
    a.NE(r1(h),r2(h)) = NaN;
end

%Finds the altitude of interest (the altitude between 250-600km)
ind_temp = find(a.ALT(:,1) > 250000 & a.ALT(:,1) < 600000);
NE_aktuell_temp = a.NE(ind_temp,:);
h_aktuell_temp = a.ALT(ind_temp,:);

%Finds the time of interest (the time between 05:00 and 11:00 UT)
index = (find(a.hour >05 & a.hour <12)); %Index gives the place in
    the array
NE_aktuell = NE_aktuell_temp(:,index');
h_aktuell = h_aktuell_temp(:,index');
t_aktuell_hour = a.hour(index');
t_aktuell_min = a.minute(index');
t_aktuell_sec = a.second(index');

%Finds the timeaxis for the plotting
ikketom = isempty(NE_aktuell);
if ikketom == 0;
    Dette_er_dag = i;
    time1 = a.hour(index)';
    minutt = a.minute(index)';
    sekund = a.second(index)';

    %matrix must have the same size
    aar = a.date(1).*ones(1,length(index));
    mnd = a.date(2).*ones(1,length(index));
    dag = a.date(3).*ones(1,length(index));

    %Date for the current day
    dato = datenum([aar',mnd',dag',time1',minutt',sekund']);
    dato_tittel = datenum([aar(1),mnd(1),dag(1)]);
    dato_aktuell = datenum([aar',mnd',dag',t_aktuell_hour,
        t_aktuell_min,t_aktuell_sec]);

    % Finds the maximum electrondensity (NeMax) and the
        corresponding height of NeMax
    hoyde = [];
    dato_NeMax = [];

    for f = 1:length(NE_aktuell) %161

        NeMax = max(NE_aktuell);
        %Gives the place in the array where the maximum density is.
        index_max = max(find(NE_aktuell(:,f) == NeMax(f)));
        b = isempty(index_max);

        if b==0;
            hoyde = [hoyde;h_aktuell(index_max',f)];

            dato_NeMax = [dato_NeMax;datestr(dato_aktuell(f))];
            disp(sprintf(['%4i     ',datestr(dato_aktuell(f)),'   
                %4.2E'],f,NeMax(f)))
            %disp(sprintf(['%4i      ',datestr(dato_aktuell(f))],f))
        else if b==1;
                hoyde = [hoyde;NaN];
            end
        end
    end

    %plots the data in two subplots
    figure
    %Plots the max values of NE
    subplot(2,1,1)
    plot(dato,NeMax,'*','color','k')
    title(['Maximum extreme densities during the first F2 peak on ',
```

```
            datestr(dato_tittel)])
        xlabel('Universal time (UT) ')
        ylabel('Maximum densities (NeMax) (1/m^3)')
        set(gca,'xlim',[datenum(aar(1),mnd(1),dag(1),06,00,00),datenum(
            aar(1),mnd(1),dag(1),11,00,00)])
        set(gca,'ylim',[0,3e12])
        datetick('x','keeplimits')

        %Plots the height of the max NE values
        subplot(2,1,2)
        plot(dato,hoyde/1000,'*','color','k')
        set(gca,'ylim',[100,800])
        set(gca,'xlim',[datenum(aar(1),mnd(1),dag(1),06,00,00),datenum(
            aar(1),mnd(1),dag(1),11,00,00)])
        xlabel('Universal time (UT) ')
        ylabel('Height of NeMax (km)')
        datetick('x','keeplimits')
    end
end
```

9.1.2 *Solarwind24102002.m*

The programme *Solarwind24102002.m* performs the calculations of the time delay on 24 October 2002 using ACE data. The calculations are described in section (3.4.1).

Listing 9.2: Solarwind24102002.m

```
clc;
clear;

%'Solarwind24102002.m' plots the timedelay with and without lag. From
    the plots generated by this programme we are able to find a
%suitable timedelay to use for the two events on oct 24 2002.

%Load file 24 October 2002
A=load('ACE021024.txt');

%Give the different columns in the file loaded above a name
year=A(:,1); %Column 1 in file A contains values of the year
day=A(:,2);
hr=A(:,3);
min=A(:,4);
sec=A(:,5);
Np=A(:,6);
vswx = A(:,10);
vswy = A(:,11);
vswz = A(:,12);
Bx = A(:,13);
By = A(:,14);
Bz = A(:,15);
X = A(:,16);
Y = A(:,17);
Z = A(:,18);

%The date is given by DOY (day-of-year), need to write it
%yyyy-mm-dd-hr-min-sec)
dato=datenum(year,1,1,hr,min,sec)+(day-1);
hour1=hr;
min1=min;

%No data is put to NaN
nosw_x = find(vswx <= -9999);
vswx(nosw_x)=NaN;
nosw_y = find(vswy <= -9999);
vswy(nosw_y)=NaN;
nosw_z = find(vswz <= -9999);
vswz(nosw_z)=NaN;
noNp = find(Np<=-9999);
Np(noNp)=NaN;
```

```
%Calculations of the time delay

%Np = particle density, mp = proton mass, Dp = the solar wind dynamic
    pressure given in nanoPascals
mp_temp = 1.672621637 * (10^(-27)); %kg
mp = mp_temp.*ones(length(A),1); %makes a vector of mp
Dp = 1.0E21.*Np.*mp.*vswx.*vswx; %Remember to put constants first, since
     matlab do faster calculations then

%the magnetopause standoff at the sub solar point calculated using the
    empirical model by
%Shue et al. (1998) from the parameters IMF Bz and solar wind dynamic
    pressure.
r0_t = (10.22 + 1.29.*tanh(0.184.*(Bz + 8.14))).*((Dp).^(-1/(6.6)));
r0 = r0_t*6378.137; %change RE to km

%Time delay with the Shue et al. method:
timedelay_t=(X-r0)./abs(vswx); %abs = absolute value
timedelay=(timedelay_t/60)+6; %seconds changed to minutes, with the
    additional 6 min

%Time delay with the simple approach method:
t_temp=X./abs(vswx);
t=(t_temp/60);

dato_medlag = dato - datenum(0,0,0,0,52,0); %time with lag added
%Plot the IMF versus UT
xmin=(datenum(2002,10,24,05,00,00)); %Change the x-axis to universal
    time during the event interval
xmax=(datenum(2002,10,24,11,00,00));

%makes 3 subplots
%IMF Bx
subplot(3,1,1)
plot(dato_medlag,Bx)
hold on;
plot(dato_medlag,0,'k');
set(gca, 'xlim', [xmin xmax]);
ylabel('IMF Bx (nT)');
datetick('x','keeplimits')
title('IMF parameters (ACE satellite)')
% plot([datenum(2002,10,24,07,39,00) datenum(2002,10,24,07,39,00)],[-20
    20],'-','color','k');%uten lag
% plot([datenum(2002,10,24,07,50,00) datenum(2002,10,24,07,50,00)],[-20
    20],'-','color','k');%uten lag
% plot([datenum(2002,10,24,07,22,00) datenum(2002,10,24,07,22,00)],[-20
    20],'-','color','k');%uten lag
% plot([datenum(2002,10,24,07,24,00) datenum(2002,10,24,07,24,00)],[-20
    20],'-','color','k');%uten lag
hold on;
plot([datenum(2002,10,24,06,45,00) datenum(2002,10,24,06,45,00)
    ],[-5.*10^12 5.*10^12],'--','color','k');
hold on;
plot([datenum(2002,10,24,08,03,00) datenum(2002,10,24,08,03,00)
    ],[-5.*10^12 5.*10^12],'--','color','k');
hold on,
plot([datenum(2002,10,24,08,07,00) datenum(2002,10,24,08,07,00)
    ],[-5.*10^12 5.*10^12],'--','color','k');
hold on;
plot([datenum(2002,10,24,08,13,00) datenum(2002,10,24,08,13,00)
    ],[-5.*10^12 5.*10^12],'--','color','k');

%IMF By
subplot(3,1,2)
plot(dato_medlag,By)
hold on;
plot(dato_medlag,0,'k');
set(gca, 'xlim', [xmin xmax]);
ylabel('IMF By (nT)');
datetick('x','keeplimits')
% plot([datenum(2002,10,24,07,39,00) datenum(2002,10,24,07,39,00)],[-20
    20],'-','color','k');%uten lag
% plot([datenum(2002,10,24,07,50,00) datenum(2002,10,24,07,50,00)],[-20
```

```
    20],'-','color','k');%uten lag
% plot([datenum(2002,10,24,07,22,00) datenum(2002,10,24,07,22,00)],[-20
    20],'-','color','k');%uten lag
% plot([datenum(2002,10,24,07,24,00) datenum(2002,10,24,07,24,00)],[-20
    20],'-','color','k');%uten lag
hold on;
plot([datenum(2002,10,24,06,45,00) datenum(2002,10,24,06,45,00)
    ],[-5.*10^12 5.*10^12],'--','color','k');
hold on;
plot([datenum(2002,10,24,08,03,00) datenum(2002,10,24,08,03,00)
    ],[-5.*10^12 5.*10^12],'--','color','k');
hold on,
plot([datenum(2002,10,24,08,07,00) datenum(2002,10,24,08,07,00)
    ],[-5.*10^12 5.*10^12],'--','color','k');
hold on;
plot([datenum(2002,10,24,08,13,00) datenum(2002,10,24,08,13,00)
    ],[-5.*10^12 5.*10^12],'--','color','k');

%IMF Bz
subplot(3,1,3)
plot(dato_medlag,Bz)
hold on;
plot(dato_medlag,0,'k');
set(gca, 'xlim', [xmin xmax]);
ylabel('IMF Bz (nT)');
% plot([datenum(2002,10,24,07,39,00) datenum(2002,10,24,07,39,00)],[-20
    20],'-','color','k');%uten lag
% plot([datenum(2002,10,24,07,50,00) datenum(2002,10,24,07,50,00)],[-20
    20],'-','color','k');%uten lag
% plot([datenum(2002,10,24,07,22,00) datenum(2002,10,24,07,22,00)],[-20
    20],'-','color','k');%uten lag
% plot([datenum(2002,10,24,07,24,00) datenum(2002,10,24,07,24,00)],[-20
    20],'-','color','k');%uten lag
hold on;
plot([datenum(2002,10,24,06,45,00) datenum(2002,10,24,06,45,00)
    ],[-5.*10^12 5.*10^12],'--','color','k');
hold on;
plot([datenum(2002,10,24,08,03,00) datenum(2002,10,24,08,03,00)
    ],[-5.*10^12 5.*10^12],'--','color','k');
hold on,
plot([datenum(2002,10,24,08,07,00) datenum(2002,10,24,08,07,00)
    ],[-5.*10^12 5.*10^12],'--','color','k');
hold on;
plot([datenum(2002,10,24,08,13,00) datenum(2002,10,24,08,13,00)
    ],[-5.*10^12 5.*10^12],'--','color','k');
datetick('x','keeplimits')
%Solar wind (x-component)
%subplot(5,1,4)
%plot(dato_medlag,vswx)
%hold on;
%plot(dato,0,'r');
%set(gca, 'xlim', [xmin xmax]);
%ylabel('Vx (km/s)');
%datetick('x','keeplimits');

%Proton density
%subplot(5,1,5)
%plot(dato_medlag,Np)
%hold on;
%plot(dato,0,'r');
%set(gca, 'xlim', [xmin xmax]);
%ylabel('Np (1/cm^3)');
%datetick('x','keeplimits')
xlabel(['Universal Time (UT) ', datestr(((xmin+xmax)/2),1),' (Time
    shifted)'])
%title('IMF parameters (ACE satellite)')
%Plots both events from 06:00 to 11:00 UT
xmin=(datenum(2002,10,24,06,00,00)); %Change the x-axis to universal
    time
xmax=(datenum(2002,10,24,11,00,00));
figure
plot(dato,timedelay);
hold on;
plot(dato,t,'g');
```

```
hold on;
% %Plots vertical lines to indicate the events
plot([datenum(2002,10,24,07,39,00) datenum(2002,10,24,07,39,00)],[35
    60],'-','color','k');%uten lag
plot([datenum(2002,10,24,07,50,00) datenum(2002,10,24,07,50,00)],[35
    60],'-','color','k');%uten lag
%plot([datenum(2002,10,24,07,39,00) datenum(2002,10,24,07,39,00)],[35
    60],'-','color','k');%-57minutt delay
%plot([datenum(2002,10,24,07,50,00) datenum(2002,10,24,07,50,00)],[35
    60],'-','color','k');%-57minutt delay
% %plot([datenum(2002,10,24,10,14,00) datenum(2002,10,24,10,14,00)],[36
    54],'--','color','r');%uten lag
% %plot([datenum(2002,10,24,10,46,00) datenum(2002,10,24,10,46,00)],[36
    54],'--','color','r');%uten lag
% plot([datenum(2002,10,24,09,27,00) datenum(2002,10,24,09,27,00)],[35
    60],'-','color','k');%-47minutt delay
% plot([datenum(2002,10,24,09,59,00) datenum(2002,10,24,09,59,00)],[35
    60],'-','color','k');%-47minutt delay
set(gca, 'xlim', [xmin xmax]);
title(['Two events of extreme densities on ', datestr(((xmin+xmax)/2),1)
    ]);
ylabel('Time delay [min]');
xlabel('Universal Time [UT] (not timeshifted)');
datetick('x','keeplimits');
%
% %Plots the timedelay without time lag divided in two plots. One for
    each
% %event.
% %first event (50min lag used)
% xmin=(datenum(2002,10,24,06,30,00)); %Change the x-axis to universal
    time
% xmax=(datenum(2002,10,24,09,00,00));
% figure
% plot(dato,timedelay);
% hold on;
% plot(dato,t,'g');
% hold on;
% %Plots vertical lines
% plot([datenum(2002,10,24,08,04,00) datenum(2002,10,24,08,04,00)],[36
    52],'--','color','r');%red
% plot([datenum(2002,10,24,08,38,00) datenum(2002,10,24,08,38,00)],[36
    52],'--','color','r');
% plot([datenum(2002,10,24,07,14,00) datenum(2002,10,24,07,14,00)],[36
    52],'-','color','k');%-50minutt delay
% plot([datenum(2002,10,24,07,48,00) datenum(2002,10,24,07,48,00)],[36
    52],'-','color','k');%black
% set(gca, 'xlim', [xmin xmax]);
% title(['The first event on ', datestr(((xmin+xmax)/2),1), ' (no lag)
    ']);
% ylabel('Time delay (min)');
% xlabel('Universal Time (UT)');
% datetick('x','keeplimits');
%
% %second event (39min lag used)
% xmin=(datenum(2002,10,24,09,00,00)); %Change the x-axis to universal
    time
% xmax=(datenum(2002,10,24,11,00,00));
% figure
% plot(dato,t,'g');
% hold on;
% plot(dato,timedelay);
% hold on
%
% %Plots vertical lines
% plot([datenum(2002,10,24,10,14,00) datenum(2002,10,24,10,14,00)],[36
    52],'--','color','r');
% plot([datenum(2002,10,24,10,46,00) datenum(2002,10,24,10,46,00)],[36
    52],'--','color','r');
% plot([datenum(2002,10,24,09,35,00) datenum(2002,10,24,09,35,00)],[36
    52],'-','color','k');%-39minutt delay
% plot([datenum(2002,10,24,10,07,00) datenum(2002,10,24,10,07,00)],[36
    52],'-','color','k');
% set(gca, 'xlim', [xmin xmax]);
% title(['The second event on ', datestr(((xmin+xmax)/2),1), ' (no lag)
```

```
    ']);
% ylabel('Time delay (min)');
% xlabel('Universal Time (UT)');
% datetick('x','keeplimits');
```

9.1.3 *Solarwind06022001.m*

Solarwind06022001.m performs the calculations for the special case on 06 February 2001 using ACE and WIND data. The calculations are described in section (3.4.1).

Listing 9.3: Solarwind06022001.m

```
clc;
clear;

%Load files 06 February 2001
A=load('ACE010206_2.txt');
B=load('ACE010206_1.txt');

[dag,mnd,aar,time,minutt,sekund,Np,Vx,Vy,Vz] = textread('ACE010206_2.txt
    ','%d-%d-%d %d:%d:%f %f %f %f');
[dag1,mnd1,aar1,time1,minutt1,sekund1,Bx,By,Bz,X,Y,Z] = textread('
    ACE010206_1.txt','%d-%d-%d %d:%d:%f %*f %f %f %f %f %f %f');

dato = (datenum(aar,mnd,dag,time,minutt,sekund));
dato_1 = (datenum(aar1,mnd1,dag1,time1,minutt1,sekund1));

%Useless data are set to NaN
noNp = find (Np <= -1.00000E+31);
Np(noNp) = NaN;

noVx = find (Vx <= -1.00000E+31);
Vx(noVx) = NaN;

noVy = find (Vy <= -1.00000E+31);
Vy(noVy) = NaN;

noVz = find (Vz <= -1.00000E+31);
Vz(noVz) = NaN;

noBx = find (Bx <= -1.00000E+31);
Bx(noBx) = NaN;

noBy = find (By <= -1.00000E+31);
By(noBy) = NaN;

noBz = find (Bz <= -1.00000E+31);
Bz(noBz) = NaN;

%We want the solar wind velocity data with the same time as the magnetic
%field data and the position data
Vx_new = interp1(dato,Vx,dato_1,'linear');
Vy_new = interp1(dato,Vy,dato_1,'linear');
Vz_new = interp1(dato,Vz,dato_1,'linear');
Np_new = interp1(dato,Np,dato_1,'linear');
X_new = X.*6378.137; %From Re to Km
Y_new = Y.*6378.137; %From Re to Km


%Timedelay (the simple approach method):
t_temp=(X_new)./abs(Vx_new);
t=(t_temp/60);

f = (find(time1 >=03 & time1 <=11));
Vx_A = Vx_new(f);
max = max(Vx_A);
min = min(Vx_A);
i = isnan(Vx_A);
```

```
q = find(i==0)
Vx_med = Vx_A(q)
med = median(Vx_med) %Median


%Plot of the IMF versus UT
xmin=(datenum(2001,02,06,04,00,00)); %Change the x-axis to universal
    time
xmax=(datenum(2001,02,06,11,00,00));

%New velocity
subplot(3,1,1)
plot(dato_1,Vx_new)
hold on;
plot(dato,0,'k');
set(gca, 'xlim', [xmin xmax]);
ylabel('V(x) (km/s)');
datetick('x','keeplimits')
title('Solar wind velocity (WIND satellite)')

subplot(3,1,2)
plot(dato_1,Vy_new)
hold on;
plot(dato,0,'k');
set(gca, 'xlim', [xmin xmax]);
ylabel('V(y) (km/s)');
datetick('x','keeplimits')

subplot(3,1,3)
plot(dato_1,Vz_new)
hold on;
plot(dato,0,'k');
set(gca, 'xlim', [xmin xmax]);
ylabel('V(z) (km/s)');
xlabel('Unviversal time (UT) on 06 February 2001');
datetick('x','keeplimits')

figure;
%Magnetic field
subplot(3,1,1)
plot(dato_1,Bx,'r')
hold on;
plot(dato,0,'k');
set(gca, 'xlim', [xmin xmax]);
ylabel('IMF Bx (nT)');
datetick('x','keeplimits')
title('Wind parameters')

subplot(3,1,2)
plot(dato_1,By,'r')
hold on;
plot(dato,0,'k');
set(gca, 'xlim', [xmin xmax]);
ylabel('IMF By (nT)');
datetick('x','keeplimits')

subplot(3,1,3)
plot(dato_1,Bz,'r')
hold on;
plot(dato,0,'k');
set(gca, 'xlim', [xmin xmax]);
ylabel('IMF Bz (nT)');
datetick('x','keeplimits')

% subplot(4,1,4)
% plot(dato_1,t,'g')
% set(gca, 'xlim', [xmin xmax]);
% set(gca, 'ylim', [-200 100]);
% ylabel('IMF Bz (nT)');
% datetick('x','keeplimits')
% %Plot events from 06:00 to 11:00 UT
% xmin=(datenum(2001,02,06,06,00,00)); %Change the x-axis to universal
    time
% xmax=(datenum(2001,02,06,11,00,00));
```

```
% figure
% plot(dato_1,t,'g');
% set(gca, 'xlim', [xmin xmax]);
% title(['Time delay on', datestr(((xmin+xmax)/2),1)]);
% ylabel('Time delay [min]');
% xlabel('Universal Time [UT] (not time shifted)');
% datetick('x','keeplimits');

%Wind position
figure;
subplot(3,1,1)
plot(dato_1,X)
hold on;
plot(dato,0,'k');
set(gca, 'xlim', [xmin xmax]);
ylabel('X position (Re)');
datetick('x','keeplimits')
title('Wind parameters')

subplot(3,1,2)
plot(dato_1,Y)
hold on;
plot(dato,0,'k');
set(gca, 'xlim', [xmin xmax]);
ylabel('y position (Re)');
datetick('x','keeplimits')

subplot(3,1,3)
plot(dato_1,Z)
hold on;
plot(dato,0,'k');
set(gca, 'xlim', [xmin xmax]);
ylabel('z position (Re)');
datetick('x','keeplimits')
```

9.1.4 *trace20021024.m*

trace20021024.m performs the tracing of extreme density events measured on 24 October 2002, while *trace20010206.m* performs the tracing of extreme density events measured on 06 February 2001. The latter programme is not included here, since the two programmes are identical. The programms use SuperDARN data to perform the tracing.
P in the programme works as a counter for the files. Each data file contains two minutes of data. Steps of -1 are used when tracing backwards, and +1 to go forward. The step size is two minutes the time resolution of SuperDARN. It turned out that an appropriate time for the tracing is 2 hours back and forth, i.e $P = 60$ is used. The reason for this choice is that only SuperDARN model data exists if one tries to go further in time and the results are more uncertain the more back or forth in time the analysis is carried.

Listing 9.4: trace20021024.m

```
clc;
clear;

%Load txt-files from directory the directory containing the txt-files.
files = dir('D:\Vigdis (Master)\Masteroppgave\Patch\20021024\*.txt')
filename = '';
for j = 1:length(files);
    filename = strvcat(filename,files(j).name); %forms the matrix
        filename containing the text strings as rows.
end

%sort files
filename = sortrows(filename); %Sorts the rows of the matrix filename in
     ascending order as a group.
```

```
%filedate get information from the name of the files
%(efield_20010206_0002.txt for instance). Variables picked out is year,
    month, date, hour and minute.
filedate = datenum(str2num(filename(:,8:11)),str2num(filename(:,12:13)),
    str2num(filename(:,14:15)),str2num(filename(:,17:18)),str2num(
    filename(:,19:20)),0);
%start time
start_time = datenum(2002,10,24,10,17,00),0
%finds the file that contains the start-time.
t = find (filedate >= (start_time-(60/86400)) & filedate <= (start_time
    +(60/86400)))

%Defines arrays
ESRpos0_x_back = []; %ESR position
ESRpos0_y_back = [];
ESRpos0_x_for = [];
ESRpos0_y_for = [];
Tromsopos0_x_back = []; %Tromso position
Tromsopos0_y_back = [];
Tromsopos0_x_for = [];
Tromsopos0_y_for = [];
Bjornoyapos0_x_back = []; %Bjornoya position
Bjornoyapos0_y_back = [];
Bjornoyapos0_x_for = [];
Bjornoyapos0_y_for = [];
NyAApos0_x_back = []; %Ny Ålesund position
NyAApos0_y_back = [];
NyAApos0_x_for = [];
NyAApos0_y_for = [];
xfor = []; %Array for the positions the programme traces
yfor = [];
xback = [];
yback = [];
xfor_NyAA = []; %Array for the positions the programme traces
yfor_NyAA = [];
xback_NyAA = [];
yback_NyAA = [];
xfor_Tromso = []; %Array for the positions the programme traces
yfor_Tromso = [];
xback_Tromso = [];
yback_Tromso = [];
xfor_Bjornoya = []; %Array for the positions the programme traces
yfor_Bjornoya = [];
xback_Bjornoya = [];
yback_Bjornoya = [];
datestart_back = []; %Arrays to check for datagaps
dateslutt_back = [];
datestart_for = [];
dateslutt_for = [];
azim_for = [];
azim_back = [];
v_for = [];
v_back = [];
Bx_back = [];
By_back = [];
Bz_back = [];
Bx_for = [];
By_for = [];
Bz_for = [];
MLat_for = [];
MLat_back = [];
MLT_for = [];
MLT_back = [];

%Latitude distance: heigth is set to 300 km and the earth's radius is
    6371 km
lat_dist = (300+6371)*((2*pi)/360);

%Location of ESR, Tromsø, Bjørnøy and Ny Ålesund in magnetic latitude
    and mangnetic longitude
MLat_ESR = 75.3726; %latitude
MLon_ESR = 113.936; %longitude
MLat_NyAA = 76.367; %latitude
MLon_NyAA = 113.167; %longitude
```

```
MLat_Tromso = 66.9149; %latitude
MLon_Tromso = 104.219; %longitude
MLat_Bjornoya = 71.775; %latitude
MLon_Bjornoya = 109.587; %longitude

%How far we trace
p=60;

disp('Bakover i tid')
%Traces BACKWARD (t:-1:t-15 f.eks)
for i = t:-1:t-p
    disp(['D:\Vigdis (Master)\Masteroppgave\Patch\20021024\',filename(i
        ,:)]) %displays the filename
    fid = fopen(['D:\Vigdis (Master)\Masteroppgave\Patch\20021024\',
        filename(i,:)],'r');
    firstline = fgets(fid);%reads the first line
    fline = [];
    fline = [str2num(firstline)]; %puts the first line into an array
    data = [];
    while feof(fid) == 0 %if not end of file, it performs the following
        tline = fgets(fid); %reads first line in the file
        data = [data;str2num(tline)]; %adds the lines into an array
    end
    fclose(fid);

    %MLT rotation
    MLT_rot = fline(:,13);
    %Gets the date information from the files
    year1 = fline(:,1);
    month1 = fline(:,2);
    day1 = fline(:,3);
    hour1 = fline(:,4);
    min1 = fline(:,5);
    sec1 = fline(:,6);
    year2 = fline(:,7);
    month2 = fline(:,8);
    day2 = fline(:,9);
    hour2 = fline(:,10);
    min2 = fline(:,11);
    sec2 = fline(:,12);
    Bx = fline(:,16);
    By = fline(:,17);
    Bz = fline(:,18);
    %Date and time of the file when it STARTS, read from first line
    date_start = datenum(year1,month1,day1,hour1,min1,sec1);
    datestart_back = [datestart_back;date_start];%makes array of the
        date and time for each file
    %Date and time of the file when it ENDS, read from first line
    date_slutt = datenum(year2,month2,day2,hour2,min2,sec2);
    dateslutt_back = [dateslutt_back;date_slutt];%makes array of the
        date and time for each file

    %Picks out the variables used for further analysis
    MLat = data(:,2); %magnetic latitude
    Mlon = data(:,3); %magnetic longitude
    Pot = data(:,4); %Potential
    Enorth = data(:,5); %E-field north
    Eeast = data(:,6); %E-field east
    v = data(:,7); %velocity (m/s)
    az = data(:,8); %azimuth on the velocity (positive towards right)

    %time for each file
    tid1 = (date_start-date_slutt).*24.*3600;
    tid1 = tid1;

    %Calculate the angle mlt from hours to radian for ESR, Bjørnøya, Ny
    %Ålesund and Tromsø. Please observe that only ESR is used for the
    %tracing. The other locations are only used for plotting.
    mlt = mod(((MLon_ESR/15)+MLT_rot),24); %hr (MLT)
    mlt_rad = 15.*mlt.*(pi/180); %from MLT to radians
    mlt_Bjornoya = mod(((MLon_Bjornoya/15)+MLT_rot),24); %hr (MLT)
    mlt_rad_Bjornoya = 15.*mlt.*(pi/180); %from MLT to radians
    mlt_NyAA = mod(((MLon_NyAA/15)+MLT_rot),24); %hr (MLT)
    mlt_rad_NyAA = 15.*mlt.*(pi/180); %from MLT to radians
```

```
mlt_Tromso = mod(((MLon_Tromso/15)+MLT_rot),24); %hr (MLT)
mlt_rad_Tromso = 15.*mlt.*(pi/180); %from MLT to radians

%Here the tracing starts

%ESR position is here calculated if there is no previous position (
    needed only once, so if the position
%is already calculated, the programme skips this step).
if length(ESRpos0_x_back) == 0 & length(ESRpos0_y_back) == 0

    ESRpos0_x_back = (90-MLat_ESR).*sin(mlt_rad);
    ESRpos0_y_back = -(90-MLat_ESR).*cos(mlt_rad);
    xback = [xback;ESRpos0_x_back];
    yback = [yback;ESRpos0_y_back];

end

if length(Tromsopos0_x_back) == 0 & length(Tromsopos0_y_back) == 0
    Tromsopos0_x_back = (90-MLat_Tromso).*sin(mlt_rad_Tromso);
    Tromsopos0_y_back = -(90-MLat_Tromso).*cos(mlt_rad_Tromso);
    xback_Tromso = [xback_Tromso;Tromsopos0_x_back];
    yback_Tromso = [yback_Tromso;Tromsopos0_y_back];
end
if length(Bjornoyapos0_x_back) == 0 & length(Bjornoyapos0_y_back) ==
     0
    Bjornoyapos0_x_back = (90-MLat_Bjornoya).*sin(mlt_rad_Bjornoya);
    Bjornoyapos0_y_back = -(90-MLat_Bjornoya).*cos(mlt_rad_Bjornoya)
        ;
    xback_Bjornoya = [xback_Bjornoya;Bjornoyapos0_x_back];
    yback_Bjornoya = [yback_Bjornoya;Bjornoyapos0_y_back];
end
if length(NyAApos0_x_back) == 0 & length(NyAApos0_y_back) == 0
    NyAApos0_x_back = (90-MLat_NyAA).*sin(mlt_rad_NyAA);
    NyAApos0_y_back = -(90-MLat_NyAA).*cos(mlt_rad_NyAA);
    xback_NyAA = [xback_NyAA;NyAApos0_x_back];
    yback_NyAA = [yback_NyAA;NyAApos0_y_back];
end

%MLT for the data in the files
mltdata = mod(((Mlon/15)+MLT_rot),24);
mltdata_rad = mltdata.*15.*(pi./180); %radians

%position for where we start tracing
data_x = (90-MLat).*sin(mltdata_rad); %position x_0
data_y = -(90-MLat).*cos(mltdata_rad); %position y_0

%Startposition Tromsø, Bjørnøya, Ny Ålesund
Tromsopos0_x_back = (90-MLat_Tromso).*sin(mlt_rad_Tromso);
Tromsopos0_y_back = -(90-MLat_Tromso).*cos(mlt_rad_Tromso);
Bjornoyapos0_x_back = (90-MLat_Bjornoya).*sin(mlt_rad_Bjornoya);
Bjornoyapos0_y_back = -(90-MLat_Bjornoya).*cos(mlt_rad_Bjornoya);
NyAApos0_x_back = (90-MLat_NyAA).*sin(mlt_rad_NyAA);
NyAApos0_y_back = -(90-MLat_NyAA).*cos(mlt_rad_NyAA);

%When we have start-position we try to find the closest point to
    this
%position which we use as our next position.
closest_point = find(((data_x-ESRpos0_x_back).^2+(data_y-
    ESRpos0_y_back).^2) == min((data_x-ESRpos0_x_back).^2+(data_y-
    ESRpos0_y_back).^2));

%new location is then trace_x and trace_y
trace_x = data_x(closest_point);
trace_y = data_y(closest_point);
sprintf('Closest point: %6.1f mlat %6.1f mlon',[MLat(closest_point),
     Mlon(closest_point)]); %the closest point in longitude and
    latitude

%before the for-loop starts over again, the new position is no
    longer
%at ESR, but the closest point

% %Farten ganget med tid og faktor
w = (v.*tid1.*360)/(2.*pi.*(6370+300).*10.^3);
```

```
    %Calculating the new position
    dx = -w.*cos(az/180.*pi).*sin(mltdata_rad)-w.*sin(az/180.*pi).*sin(
        mltdata_rad-(pi./2)); %sjekk om pluss her
    dy = w.*cos(az/180.*pi).*cos(mltdata_rad)+w.*sin(az/180.*pi).*cos((
        pi./2)-mltdata_rad);
    [v(closest_point),w(closest_point),az(closest_point),mltdata_rad(
        closest_point)];
    ESRpos0_x_back = trace_x+dx(closest_point);
    ESRpos0_y_back = trace_y+dy(closest_point);

    %saves the values into arrays
    xback = [xback;ESRpos0_x_back];
    yback = [yback;ESRpos0_y_back];
    xback_NyAA = [xback_NyAA;NyAApos0_x_back];
    yback_NyAA = [yback_NyAA;NyAApos0_y_back];
    xback_Tromso = [xback_Tromso;Tromsopos0_x_back];
    yback_Tromso = [yback_Tromso;Tromsopos0_y_back];
    xback_Bjornoya = [xback_Bjornoya;Bjornoyapos0_x_back];
    yback_Bjornoya = [yback_Bjornoya;Bjornoyapos0_y_back];
    azim_back = [azim_back;az(closest_point)];
    v_back = [v_back;v(closest_point)];
    Bx_back = [Bx_back;Bx];
    By_back = [By_back;By];
    Bz_back = [Bz_back;Bz];
    MLat_back = [MLat_back;MLat(closest_point)];
    MLT_back = [MLT_back;mltdata_rad(closest_point)];
end

%Checking for datagaps
for g=1:p
    if datestart_back(g)~= dateslutt_back(g+1)
        disp(['Datagap between ',datestr(datestart_back(g),13),' and ',
            datestr(datestart_back(g+1),13)])
    end
end
%kan evt bruke save-funksjon her som lagrer det over og så kan man
    plotte
%det som er lagret for å unngå å måtte kjøre programmet igjen og igjen
    ...
%time for each file

disp('Forover i tid')
%Traces forward (t:1:t+15 f.eks)
for j = t:1:t+p
    disp(['D:\Vigdis (Master)\Masteroppgave\Patch\20021024\',filename(j
        ,:)]) %displays the filename
    fid = fopen(['D:\Vigdis (Master)\Masteroppgave\Patch\20021024\',
        filename(j,:)],'r');
    firstline = fgets(fid);%reads the first line
    fline = [];
    fline = [str2num(firstline)]; %puts the first line into an array
    data = [];
    while feof(fid) == 0 %if not end of file, it performs the following
        tline = fgets(fid); %reads first line in the file
        data = [data;str2num(tline)]; %adds the lines into an array
    end
    fclose(fid);

    %MLT rotation
    MLT_rot = fline(:,13);
    %Gets the date information from the files
    year1 = fline(:,1);
    month1 = fline(:,2);
    day1 = fline(:,3);
    hour1 = fline(:,4);
    min1 = fline(:,5);
    sec1 = fline(:,6);
    year2 = fline(:,7);
    month2 = fline(:,8);
    day2 = fline(:,9);
    hour2 = fline(:,10);
    min2 = fline(:,11);
    sec2 = fline(:,12);
```

```
Bx = fline(:,16);
By = fline(:,17);
Bz = fline(:,18);
%Date and time of the file when it STARTS, read from first line
date_start = datenum(year1,month1,day1,hour1,min1,sec1);
datestart_for = [datestart_for;date_start];
%Date and time of the file when it ENDS, read from first line
date_slutt = datenum(year2,month2,day2,hour2,min2,sec2);
dateslutt_for = [dateslutt_for;date_slutt];

%Picks out the variables used for further analysis
MLat = data(:,2); %magnetic latitude
Mlon = data(:,3); %magnetic longitude
Pot = data(:,4); %Potential
Enorth = data(:,5); %E-field north
Eeast = data(:,6); %E-field east
v = data(:,7); %velocity (m/s)
az = data(:,8); %azimuth on the velocity (positive towards right)

%time for each file
tid2 = (date_start-date_slutt).*24.*3600;
tid2 = -tid2;

%Calculate the angle mlt from hours to radian for ESR, Bjørnøya, Ny
%Ålesund and Tromsø
mlt = mod(((MLon_ESR/15)+MLT_rot),24); %hr (MLT)
mlt_rad = 15.*mlt.*(pi/180); %from MLT to radians
mlt_Bjornoya = mod(((MLon_Bjornoya/15)+MLT_rot),24); %hr (MLT)
mlt_rad_Bjornoya = 15.*mlt.*(pi/180); %from MLT to radians
mlt_NyAA = mod(((MLon_NyAA/15)+MLT_rot),24); %hr (MLT)
mlt_rad_NyAA = 15.*mlt.*(pi/180); %from MLT to radians
mlt_Tromso = mod(((MLon_Tromso/15)+MLT_rot),24); %hr (MLT)
mlt_rad_Tromso = 15.*mlt.*(pi/180); %from MLT to radians

%Calculate the angle mlt from hours to radian for ESR
mlt = mod(((MLon_ESR/15)+MLT_rot),24); %hr (MLT)
mlt_rad = 15.*mlt.*(pi/180); %from MLT to radians

%Here the tracing starts

%ESR position is here calculated if there is no previous position (
    needed only once, so if the position
%is already calculated, the programme skips this step).
if length(ESRpos0_x_for) == 0 & length(ESRpos0_y_for) == 0

    ESRpos0_x_for = (90-MLat_ESR).*sin(mlt_rad);
    ESRpos0_y_for = -(90-MLat_ESR).*cos(mlt_rad);
    xfor = [xfor;ESRpos0_x_for];
    yfor = [yfor;ESRpos0_y_for];

end

if length(Tromsopos0_x_for) == 0 & length(Tromsopos0_y_for) == 0
    Tromsopos0_x_for = (90-MLat_Tromso).*sin(mlt_rad_Tromso);
    Tromsopos0_y_for = -(90-MLat_Tromso).*cos(mlt_rad_Tromso);
    xfor_Tromso = [xfor_Tromso;Tromsopos0_x_for];
    yfor_Tromso = [yfor_Tromso;Tromsopos0_y_for];
end

if length(Bjornoyapos0_x_for) == 0 & length(Bjornoyapos0_y_for) == 0
    Bjornoyapos0_x_for = (90-MLat_Bjornoya).*sin(mlt_rad_Bjornoya);
    Bjornoyapos0_y_for = -(90-MLat_Bjornoya).*cos(mlt_rad_Bjornoya);
    xfor_Bjornoya = [xfor_Bjornoya;Bjornoyapos0_x_for];
    yfor_Bjornoya = [yfor_Bjornoya;Bjornoyapos0_y_for];
end

if length(NyAApos0_x_for) == 0 & length(NyAApos0_y_for) == 0
    NyAApos0_x_for = (90-MLat_NyAA).*sin(mlt_rad_NyAA);
    NyAApos0_y_for = -(90-MLat_NyAA).*cos(mlt_rad_NyAA);
    xfor_NyAA = [xfor_NyAA;NyAApos0_x_for];
    yfor_NyAA = [yfor_NyAA;NyAApos0_y_for];
end

%MLT for the data in the files
```

```
    mltdata = mod(((Mlon/15)+MLT_rot),24);
    mltdata_rad = mltdata.*15.*(pi./180); %radians

    %position for where we start tracing
    data_x = (90-MLat).*sin(mltdata_rad); %position x_0
    data_y = -(90-MLat).*cos(mltdata_rad); %position y_0

    %Startposition Tromsø, Bjørnøya, Ny Ålesund
    Tromsopos0_x_for = (90-MLat_Tromso).*sin(mlt_rad_Tromso);
    Tromsopos0_y_for = -(90-MLat_Tromso).*cos(mlt_rad_Tromso);
    Bjornoyapos0_x_for = (90-MLat_Bjornoya).*sin(mlt_rad_Bjornoya);
    Bjornoyapos0_y_for = -(90-MLat_Bjornoya).*cos(mlt_rad_Bjornoya);
    NyAApos0_x_for = (90-MLat_NyAA).*sin(mlt_rad_NyAA);
    NyAApos0_y_for = -(90-MLat_NyAA).*cos(mlt_rad_NyAA);

    %When we have start-position we try to find the closest point to
        this
    %position which we use as our next position.
    closest_point = find(((data_x-ESRpos0_x_for).^2+(data_y-
        ESRpos0_y_for).^2) == min((data_x-ESRpos0_x_for).^2+(data_y-
        ESRpos0_y_for).^2));

    %new location is then trace_x and trace_y
    trace_x = data_x(closest_point);
    trace_y = data_y(closest_point);
    sprintf('Closest point: %6.1f mlat %6.1f mlon',[MLat(closest_point),
         Mlon(closest_point)]); %the closest point in longitude and
        latitude

    %before the for-loop starts over again, the new position is no
        longer
    %at ESR, but the closest point

    % %Farten ganget med tid og faktor
    w = (v.*tid2.*360)/(2.*pi.*(6370+300).*10.^3);

    %Calculating the new position
    dx = -w.*cos(az/180.*pi).*sin(mltdata_rad)-w.*sin(az/180.*pi).*sin(
        mltdata_rad-(pi./2)); %sjekk om pluss her
    dy = w.*cos(az/180.*pi).*cos(mltdata_rad)+w.*sin(az/180.*pi).*cos((
        pi./2)-mltdata_rad);
    [v(closest_point),w(closest_point),az(closest_point),mltdata_rad(
        closest_point)];
    ESRpos0_x_for = trace_x+dx(closest_point);
    ESRpos0_y_for = trace_y+dy(closest_point);

    %saves the values into arrays
    xfor = [xfor;ESRpos0_x_for];
    yfor = [yfor;ESRpos0_y_for];
    xfor_NyAA = [xfor_NyAA;NyAApos0_x_for];
    yfor_NyAA = [yfor_NyAA;NyAApos0_y_for];
    xfor_Tromso = [xfor_Tromso;Tromsopos0_x_for];
    yfor_Tromso = [yfor_Tromso;Tromsopos0_y_for];
    xfor_Bjornoya = [xfor_Bjornoya;Bjornoyapos0_x_for];
    yfor_Bjornoya = [yfor_Bjornoya;Bjornoyapos0_y_for];
    azim_for = [azim_for;az(closest_point)];
    v_for = [v_for;v(closest_point)];
    Bx_for = [Bx_for;Bx];
    By_for = [By_for;By];
    Bz_for = [Bz_for;Bz];
    MLat_for = [MLat_for;MLat(closest_point)];
    MLT_for = [MLT_for;mltdata_rad(closest_point)];
end
%checking for datagaps
for g=1:p
    if datestart_for(g+1)~= dateslutt_for(g)
        disp(['Datagap between ',datestr(datestart_for(g),13),' and ',
            datestr(datestart_for(g+1),13)])
    end
end

save 24oct2002_1017_p60.mat
```

9.1.5 *plot20021024.m*

plot20021024.m plots the results of the tracing obtained from *trace20021024.m*.

Listing 9.5: plot20021024.m

```
%Load file saved from "trace20021024.m"
load 24oct2002_0722_p60

%PLOTS THE TRACING ON 24 OCTOBER 2002
angle = [(0:360).*(pi/180)]; %defines the angle (a whole circle in
    radians)
m = 1*cos(angle); %circle with radius 1
n = 1*sin(angle);

%plots a circle at 10, 20 and 30 (corresponding to latitude 80, 70 and
    60)
plot(10.*m,10.*n,'k')
hold on;
plot(20.*m,20.*n,'k');
hold on;
plot(30.*m,30.*n,'k')
hold on;

%Makes the axis
plot([0 0],[-30 30],'k');
hold on;
plot([-30 30],[0 0],'k')
hold on;

%Plots start position for the backward tracing as a little circle
plot(xback(1),yback(1),'o','color','r')
text(xfor(1),yfor(1),'ESR')
hold on;

%Plots the location of Ny Ålesund, Tromsø and Bjørnøya on the map
plot(xfor_NyAA(1),yfor_NyAA(1),'o','color','b')
text(xfor_NyAA(1),yfor_NyAA(1),'NYA')
hold on;
plot(xfor_Tromso(1),yfor_Tromso(1),'o','color','b')
text(xfor_Tromso(1),yfor_Tromso(1),'TRO')
hold on;
plot(xfor_Bjornoya(1),yfor_Bjornoya(1),'o','color','b')
text(xfor_Bjornoya(1),yfor_Bjornoya(1),'BJN')
hold on;

%Plots start position for the forward tracing as a little circle
plot(xfor(1),yfor(1),'o','color','b')
hold on;

%Plots the path from start to end of the trace BACKWARD
plot(xback,yback,'.','color','r','linewidth',2.5)
hold on;

%Plots the path from start to end of the trace FORWARD
plot(xfor,yfor,'.','color','b','linewidth',2.5)
title([datestr(start_time)]);
axis square;
hold on;

%Find time in the plots
ix_back = find (abs((2*24.*datestart_back - round(2*24.*datestart_back))
    ) < (1/60));
if length(ix_back) > 0
    plot(xback(ix_back),yback(ix_back),'k*')
    for i =1:length(ix_back)
        text(xback(ix_back(i)),yback(ix_back(i)),datestr(datestart_back(
            ix_back(i)),15))
    end
end
ix_for = find (abs((2*24.*datestart_for - round(2*24.*datestart_for))) <
     (1/60));
if length(ix_for) > 0
    plot(xfor(ix_for),yfor(ix_for),'k*')
```

```
    for i =1:length(ix_for)
        text(xfor(ix_for(i)),yfor(ix_for(i)),datestr(datestart_for(
            ix_for(i)),15))
    end
end

%axis limits
set(gca,'Xlim',[-30 30],'Ylim',[-30 30])
%Plots the magnetic azimuth and flow velocity versus time
xmin = datenum(flipud(datestart_back(p-1)),13)
xmax = datenum(datestart_for(p),13)

figure;
subplot(2,1,1)
plot(flipud(datestart_back),flipud(azim_back),'color','r')
hold on;
plot(datestart_for,azim_for,'color','b')
set(gca, 'xlim', [xmin xmax])
datetick('x','keeplimits')
ylabel('Azimuth')
title('Red = backward, Blue = forward')

subplot(2,1,2)
plot(flipud(datestart_back),flipud(v_back),'color','r')
hold on;
plot(datestart_for,v_for,'color','b')
set(gca, 'xlim', [xmin xmax])
datetick('x','keeplimits')
ylabel('Velocity (m/s)')
xlabel(['Universal time (UT) ',datestr(datestart_for(1),1)])

% subplot(4,1,3)
% plot(flipud(datestart_back),flipud(MLat_back),'color','r')
% hold on;
% plot(datestart_for,MLat_for,'color','b')
% set(gca, 'xlim', [xmin xmax])
% datetick('x','keeplimits')
% ylabel('MLat')
%
% subplot(4,1,4)
% plot(flipud(datestart_back),flipud(MLT_back),'color','r')
% hold on;
% plot(datestart_for,MLT_for,'color','b')
% set(gca, 'xlim', [xmin xmax])
% datetick('x','keeplimits')
% xlabel(['Universal time (UT) ',datestr(datestart_for(1),1)])
% ylabel('MLT')

%Plots the IMF components
figure;
subplot(3,1,1)
plot(flipud(datestart_back),flipud(Bx_back),'color','r')
hold on;
plot(datestart_for,Bx_for,'color','b')
hold on;
plot(flipud(datestart_back),0,'-','color','k')
hold on;
plot(datestart_for,0,'-','color','k')
set(gca, 'xlim', [xmin xmax])
datetick('x','keeplimits')
ylabel('Bx')
title('Interplanetary Magnetic Field (IMF)')

subplot(3,1,2)
plot(flipud(datestart_back),flipud(By_back),'color','r')
hold on;
plot(datestart_for,By_for,'color','b')
hold on;
plot(flipud(datestart_back),0,'k-')
hold on;
plot(datestart_for,0,'k-')
set(gca, 'xlim', [xmin xmax])
datetick('x','keeplimits')
ylabel('By')
```

```
subplot(3,1,3)
plot(flipud(datestart_back),flipud(Bz_back),'color','r')
hold on;
plot(datestart_for,Bz_for,'color','b')
hold on;
plot(flipud(datestart_back),0,'k-')
hold on;
plot(datestart_for,0,'k-')
set(gca, 'xlim', [xmin xmax])
datetick('x','keeplimits')
ylabel('Bz')
xlabel(['Universal time (UT) ',datestr(datestart_for(1),1)])
```

Bibliography

Anderson, D., Buchau, J., and Heelis, R. (1988). Origin of density enhancements in the winter polar cap ionosphere. *Radio Science*, 23(4).

Austen, J., Franke, S., Liu, C., and Yeh, K. (1986). Application of computerized tomography techniques to ionospheric research. In *IN: International Beacon Satellite Symposium on Radio Beacon Contribution to the Study of Ionization and Dynamics of the Ionosphere and to Corrections to Geodesy and Technical Workshop, Oulu, Finland, June 9-14, 1986, Proceedings.*

Axford, W., Dessler, A., and Gottlieb, B. (1963). Termination of Solar Wind and Solar Magnetic Field. *The Astrophysical Journal*, 137:1268.

Baker, D. (1998). What is space weather? *Advances in Space Research*, 22(1):7–16.

Baker, D. (2005). Introduction to Space Weather. *Space Weather: The Physics Behind a Slogan*, page 3.

Baker, J., Greenwald, R., Ruohoniemi, J., Oksavik, K., Gjerloev, J., Paxton, L., and Hairston, M. (2007). Observations of ionospheric convection from the Wallops SuperDARN radar at middle latitudes. *Journal of Geophysical Research*, 112.

Baker, K. and Wing, S. (1989). A new magnetic coordinate system for conjugate studies at high latitudes. *Journal of Geophysical Research*, 94(A7):9139–9143.

Basu, S., Groves, K., Basu, S., and Sultan, P. (2002). Specification and forecasting of scintillations in communication/navigation links: current status and future plans. *Journal of Atmospheric and Solar-Terrestrial Physics*, 64(16):1745–1754.

Basu, S., MacKenzie, E., Basu, S., Coley, W., Sharber, J., and Hoegy, W. (1990). Plasma structuring by the gradient drift instability at high latitudes and comparison with velocity shear driven processes. *Journal of Geophysical Research*, 95(A6).

Behnke, R., Tascione, T., Hildner, E., Cliffswallow, W., Robinson, R., Cobb, N., Green, A., Basu, S., de la Beaujardiere, O., and Carovillano, R. (1995). The National Space Weather Program: The Strategic Plan. *Rep. FCM-P30-1995.*

Beynon, W. and Williams, P., editors (1978). *Incoherent scatter of radio waves from the ionosphere.* Reports on Progress in Physics 41: 909-947, California.

Brekke, A. (1997). *Physics of the Upper Polar Atmosphere*. Wiley-Praxis series in atmospheric physics.

Buchau, J., Reinisch, B., Weber, E., and Moore, J. (1983). Structure and dynamics of the winter polar cap F region. *Radio Science*, 18(6):995–1010.

Buchau, J., Weber, E., Anderson, D., and Carlson, H. (1985). Ionospheric structures in the polar cap- Their origin and relation to 250-MHz scintillation. *Radio Science(ISSN 0048-6604)*, 20:325–338.

Bust, G. and Crowley, G. (2007). Tracking of polar cap ionospheric patches using data assimilation. *Journal of Geophysical Research*, 112.

Carlson, H. (1998). Response of the polar cap ionosphere to changes in (solar wind) IMF. In *Polar Cap Boundary Phenomena*, pages 255–270. Kluwer Academic Publishers.

Carlson, H., Moen, J., Oksavik, K., Nielsen, C., McCrea, W., Pedersen, T., and Gallop, P. (2006). Direct observations of injection events of subauroral plasma into the polar cap. *Geophys.Res.Lett.*

Carlson, H., Oksavik, K., Moen, J., and Pedersen, T. (2004). Ionospheric patch formation: Direct measurements of the origin of a polar cap patch. *Geophys. Res. Lett*, 31.

Carlson, H., Oksavik, K., Moen, J., Van Eyken, A., and Guio, P. (2002). ESR mapping of polar-cap patches in the dark cusp. *Geophysical Research Letters*, 29(10):24–1.

Chapman, S. and Bartels, J. (1940). *Geomagnetism*. Clarendon press Oxford.

Chisham, G., Lester, M., Milan, S., Freeman, M., Bristow, W., Grocott, A., McWilliams, K., Ruohoniemi, J., Yeoman, T., Dyson, P., Greenwald, R., Kikuchi, T., Pinnock, M., Rash, J., Sato, N., Sofko, G., Villain, J.-P., and Walker, A. (2007). A decade of the super dual auroral radar network (superdarn): scientific achievements, new techniques and future directions. *Surveys in Geophysics*, 28(1).

Cowley, S. (1976). Comments on the Merging of Nonantiparallel Magnetic Fields. *Journal of Geophysical Research*.

Cowley, S. and Lockwood, M. (1992). Excitation and decay of solar wind-driven flows in the magnetosphere-ionosphere system. *Ann. Geophysicae*, 10:103–115.

Cowley, S., Morelli, J., and Lockwood, M. (1991). Dependence of convective flows and particle precipitation in the high-latitude dayside ionosphere on the x and y components of the interplanetary magnetic field. *Journal of Geophysical Research*, 96(A4):5557–5564.

Crooker, N. (1979). Dayside Merging and Cusp Geometry. *Journal of Geophysical Research*, 84(A3):951–959.

Crowley, G. (1996). Critical Review of Ionospheric Patches and Blobs. *The Review of Radio Science 1993-1996*, pages 619–649.

Crowley, G., Ridley, A., Deist, D., Wing, S., Knipp, D., Emery, B., Foster, J., Heelis, R., Hairston, M., and Reinisch, B. (2000). Transformation of high-latitude ionospheric F-region patches into blobs during the March 21, 1990, storm. *Journal of Geophysical Research*.

Dandekar, B. and Bullett, T. (1999). Morphology of polar cap patch activity. *Radio Science*, 34(5):1187–1205.

Doe, R., Kelly, J., and Sanchez, E. (2001). Observations of persistent dayside F region electron temperature enhancements associated with soft magnetosheathlike precipitation. *Journal of Geophysical Research-Space Physics*, 106(A3).

Dungey, J. (1961). Interplanetary magnetic field and the auroral zones. *Physical Review Letters*, 6(2):47–48.

Dungey, J. (1963). The structure of the exosphere or adventures in velocity space. *Geophysics, The Earth's Environment*, pages 503–550.

Elphic, R. (1989). Observations of flux transfer events: Are FTEs flux ropes, islands, or surface waves. In *Chapman conference on the physics of magnetic flux ropes*, volume 27, page 31.

Evans, J. (1969). Theory and practice of ionosphere study by Thomson scatter radar. *Proceedings of the IEEE*, 57(4):496–530.

Fairfield, D. and Cahill Jr, L. (1966). Transition region magnetic field and polar magnetic disturbances. *Journal of Geophysical Research*, 71(1).

Fejer, B. and Kelley, M. (1980). Ionospheric irregularities. *Reviews of Geophysics*, 18(2).

Fejer, B. and Providakes, J. (1987). High-latitude E-region irregularities: new results. *Phys. Scripta*, 18:167–178.

Feldstein, Y. (1967). Distribution of aurora and magnetic disturbances at high latitude in connection with the asymmetric form of the magnetosphere. *Aurora and Airglow*, 13:98–118.

Foster, J. (1993). Storm Time Plasma Transport at Middle and High Latitudes. *Journal of Geophysical Research*, 98(A2):1675–1689.

Foster, J. and Burke, W. (2002). SAPS: A new characterization for sub-auroral electric fields. *EOS*, 83:393–394.

Foster, J., Coster, A., Erickson, P., Holt, J., Lind, F., Rideout, W., McCready, M., van Eyken, A., Barnes, R., Greenwald, R., and Rich, F. (2005). Multiradar observations of the polar tongue of ionization. *Journal of geophysical research*.

Foster, J. and Doupnik, J. (1984). Plasma convection in the vicinity of the dayside cleft. *Journal of Geophysical Research (ISSN 0148-0227)*, 89.

Foster, J., Erickson, P., Coster, A., Goldstein, J., and Rich, F. (2002). Ionospheric signatures of plasmaspheric tails. *Geophysical Research Letters*, 29(13).

Foster, J., Erickson, P., Lind, F., and Rideout, W. (2004). Millstone Hill coherent-scatter radar observations of the electric field variability in the sub-auroral polarization stream. *Geophysical Research Letters*.

Glatzmaier, G. and Roberts, P. (1995). A three-dimensional convective dynamo solution with rotating and finitely conducting inner core and mantle. *Physics of the Earth and Planetary Interiors*, 91:63–75.

Goldston, R. and Rutherford, P. (1995). *Introduction to Plasma Physics*. Institute of Physics Press.

Gosling, J., Thomsen, M., Bame, S., Elphic, R., and Russel, C. (1990). Plasma flow reversals at the dayside magnetopause and the origin of asymmetric polar cap convection. *Journal of Geophysical Research*, 95(A6):8073–8084.

Greenwald, R., Baker, K., Dudeney, J., Pinnock, M., Jones, T., Thomas, E., Villain, J.-P., Cerisier, J.-C., Senior, C., Hanuise, C., Hunsucker, R., Sofko, G., Koehler, J., Nielsen, E., Pellinen, R., Walker, A., Sato, N., and Yanmagishi, H. (1995). DARN/SuperDARN A global view of the dynamics of high-latitude convection. *Space Science Reviews*, 71.

Gustafsson, G., Papitashvili, N., and Papitashvili, V. (1992). A revised corrected geomagnetic coordinate system for epochs 1985 and 1990. *Journal of Atmospheric and Terrestrial Physics*, 54(11/12):1609–1631.

Haerendel, G., Paschmann, G., Sckopke, N., and Rosenbauer, H. (1978). The frontside boundary layer of the magnetosphere and the problem of reconnection. *Journal of Geophysical Research*.

Hapgood, M. (1992). Space Physics Coordinate Transformations: A user guide. *Planet. Space Sci.*, 40.

Hargreaves, J. (1992). *The solar-terrestrial enviroment*. Cambridge atmospheric and space science series.

Heelis, R. and Lowell, J. (1982). A model of the high-latitude ionospheric convection pattern. *Journal of Geophysical Research*, 87(A8):6339–6345.

Heppner, J. (1977). Empirical high-latitude electric field models. *Journal of Geophysical Research*.

Heppner, J. and Maynard, N. (1987). Empirical high-latitude electric field models. *Journal of Geophysical Research*.

Hosokawa, K., Shiokawa, K., Otsuka, Y., Nakajima, A., Ogawa, T., and Kelly, J. (2006). Estimating drift velocity of polar cap patches with all-sky airglow imager at Resolute Bay, Canada. *Geophysical Research Letters*, 33.

Hundhausen, A. (1995). The solar wind. In Kivelson, M. and Russell, C., editors, *Introduction to space physics*, chapter 4, pages 91–128. Cambridge University Press.

Øieroset, M., Phan, T., Fujimoto, M., Lin, R., and Lepping, R. (2001). In situ detection of collisionless reconnection in the earth's magnetotail. *Letters to nature*, 412:414–417.

Jackson, J. (1962). *Classical Electrodynamics*. John Wiley.

Jørgensen, T., Friis-Christensen, E., and Wilhjelm, J. (1972). Interplanetary magnetic-field direction and high-latitude ionospheric currents. *Journal of Geophysical Research*, 77(10).

Kelley, M., Vickrey, J., Carlson, C., and Torbert, R. (1982). On the origin and spatial extent of high-latitude F region irregularities. *Journal of Geophysical Research*, 87:4469–4475.

Kelly, J. and Vickrey, J. (1984). F-region ionospheric structure associated with antisunward flow near the dayside polar cusp. *Geophysical Research Letters (ISSN 0094-8276)*, 11.

Kivelson, M. and Russel, C. (1995). *Introduction to Space Physics*. Cambridge University Press.

Knudsen, W. (1974). Magnetospheric convection and the high-latitude F_2 ionosphere. *Journal of geophysical research*, 79(7):1046–1055.

Lepping, R., Berdichevsky, D., and Wu, C.-C. (2003). Sun-Earth electrodynamics: The solar wind connection. *Recent Res. Astrophys.*

Lockwood, M. (1991). Modelling the high-latitude-ionosphere. *National Propagation Programme*.

Lockwood, M. and Carlson Jr., H. (1992). Production of polar cap electron density patches by transient magnetopause reconnection. *Geophysical Research Letters*.

Lockwood, M., Cowley, S., Smith, M., Rijnbeek, R., and Elphic, R. (1995). The contribution of flux transfer events to convection. *Geophysical Research Letters*, 22(10):1185–1188.

Lockwood, M., Denig, W., Farmer, A., Davda, V., Cowley, S., and Lühr (1993). Ionospheric signatures of pulsed reconnection at the Earth's magnetopause. *Letters to nature*, 361:424–428.

Lockwood, M. and Moen, J. (1999). Reconfiguration and closure of lobe flux by reconnection during northward IMF: possible evidence for signatures in cusp/cleft auroral emissions. *Annales Geophysicae*, 17:996–1011.

Lockwood, M., Sandholt, P., and Cowley, S. (1989). Interplanetary magnetic field control of dayside auroral activity and the transfer of momentum across the dayside magnetopause. *Planetary Space Science*.

Luhmann, J. (1995). Ionospheres. In Kivelson, M. and Russell, C., editors, *Introduction to space physics*, pages 183–202. Cambridge University Press.

MacDougall, J. and Jayachandran, P. (2007). Polar patches: Auroral zone precipitation effects. *Journal of Geophysical Research-Space Physics*, 112(A5):A05312.

Maezawa, K. (1976). Magnetosphere convection induced by the positive and negative z components of the interplanetary magnetic field: quantitative analysis using polar cap magnetic records. *J. Geophys. Res.*

Maynard, N., Weber, E., Weimer, D., Moen, J., Onsager, T., Heelis, R., and Egeland, A. (1997). How wide in magnetic local time is the cusp? An event study. *Journal of Geophysical Research*, 102(A3).

McComas, D., Bame, S., Barker, P., Feldman, W., Phillips, J., Riley, P., and Griffee, J. (1998). Solarwind Electron Proton Alpha Monitor (SWEPAM) For The Advanced Composition Explorer. *Space Science Reviews*, pages 563–612.

McCrea, I., Lockwood, M., Moen, J., Pitout, F., Eglitis, P., Aylward, A., Cerisier, J., Thorolfssen, A., and Milan, S. (2000). ESR and EISCAT observations of the response of the cusp and cleft to IMF orientation changes. In *Annales Geophysicae*, volume 18, pages 1009–1026. Springer.

McEwen, D. and Harris, D. (1996). Occurrence patterns of F layer patches over the north magnetic pole. *Radio Science*, 31(3):619–628.

Mead, G. and Beard, D. (1964). Shape of the geomagnetic field solar wind boundary. *J. Geophys. Res*, 69(7):1169–1179.

Milan, S., Yeoman, T., and Lester, M. (1998). The dayside auroral zone as a hard target for coherent HF radars. *Geophysical Research Letters*, 25(19):3717–3720.

Moen, J., Carlson, H., Oksavik, K., Nielsen, C., Pryse, S., Middleton, H., McCrea, I., and Gallop, P. (2006). EISCAT observations of plasma patches at sub-auroral cusp latitudes. *Annales Geophysicae*.

Moen, J., Carlson, H., and Sandholt, P. (1999). Continuous observation of cusp auroral dynamics in response to an imf by polarity change. *Geophysical research letters*, 26(9):1243–1246.

Moen, J., Gulbrandsen, N., Lorentzen, D., and Carlson, H. (2007). On the MLT distribution of F region polar cap patches at night. *Geophysical Research Letters*.

Moen, J., Lockwood, M., Oksavik, K., Carlson, H., Denig, W., van Eyken, A., and McCrea, I. (2004). The dynamics and relationships of precipitation, temperature and convection boundaries in the dayside auroral ionosphere. *Annales Geophysicae*, 22:1973–1987.

Moen, J., Qiu, X., Carlson, H., Fujii, R., and McCrea, I. (2008). On the diurnal variability in F2-region plasma density above the EISCAT Svalbard radar. *Annales Geophysicae*.

Moen, J., Sandholt, P., Lockwood, M., Denig, W., Løvhaug, U., Lybekk, B., Egeland, A., Opsvik, D., and Friis-Christensen, E. (1995). Events of enhanced convection and related dayside auroral activity. *Journal of Geophysical Research-Space Physics*, 100(A12).

Ness, N., Hundhaus, A., and Bame, S. (1971). Observations of Interplanetary Medium-VELA 3 and IMP 3, 1965–1967. *J. Geophys. Res*, 76(28):6643.

Newell, P., Burke, W., Meng, C., Sanchez, E., and Greenspan, M. (1991a). Identification and observations of the plasma mantle at low altitude. *Journal of Geophysical Research-Space Physics*, 96(A1).

Newell, P., Burke, W., Sanchez, E., Meng, C., Greenspan, M., and Clauer, C. (1991b). The low-latitude boundary layer and the boundary plasma sheet at low altitude: Prenoon precipitation regions and convection reversal boundaries. *J. Geophys. Res.*, 96(A12):21013–21023.

Newell, P. and Meng, C. (1992). Mapping the dayside ionosphere to the magnetosphere according to particle precipitation characteristics. *Geophysical research letters*, 19(6):609–612.

Newell, P., Ruohoniemi, J., and Meng, C.-I. (2004). Maps of precipitation by source region, binned by IMF, with inertial convection streamlines. *Journal of Geophysical Research*, 109.

Njål Guldbrandsen (2006). Polar cap patch occurrence rate over Svalbard and it's dependence on IMF By. Master's thesis, Universitetet i Oslo.

Ogawa, Y., Buchert, S., Fujii, R., Nozawa, S., and van Eyken, A. (2009). Characteristics of ion upflow and downflow observed with the european incoherent scatter svalbard radar. *Journal of Geophysical Research*, 114(A05305).

Ogilvie, K., Chornay, D., Fritzenreiter, R., Hunsaker, F., Keller, J., Lobell, J., Miller, G., Scudder, J., Sittler Jr, E., Torbert, R., Bodet, D., Needell, G., Lazarus, A., Steinberg, J., Tappan, J., Mavretic, A., and Gergin, E. (1995). Swe, a comprehensive plasma instrument for the wind spacecraft. *Space Science Reviews*, 71:55–77.

Oksavik, K., Greenwald, R., Ruohoniemi, J., Hairston, M., Paxton, L., Baker, J., Gjerloev, J., and Barnes, R. (2006a). First observations of the temporal/spatial variation of the sub-auroral polarization stream from the SuperDARN Wallops HF radar. *Geophys. Res. Lett*, 33.

Oksavik, K., Ruohoniemi, J., Greenwald, R., Baker, J., Moen, J., Carlson, H., Yeoman, T., and Lester, M. (2006b). Observations of isolated polar cap patches by the European Incoherent Scatter (EISCAT) Svalbard and Super Dual Auroral Radar Network (SuperDARN) Finland radars. *Journal of Geophysical Research*.

Parker, E. (1957). Sweet's mechanism for merging magnetic fields in conducting fluids. *Journal of Geophysical Research*.

Pedersen, T., Fejer, B., Doe, R., and Weber, E. (2000). An incoherent scatter radar technique for determining two-dimensional horizontal ionization structure in polar cap F region patches. *Journal of Geophysical Research*, 105(A5):10.637–10.655.

Pinnock, M., Rodger, A., and Berkey, F. (1995). High-latitude F region electron concentration measurements near noon: a case study. *Journal of Geophysical Research-Space Physics*, 100(A5).

Priest, E. (1995). *Introduction to space physics: The Sun and its magnetohydrodynamics*, chapter 3, pages 58–90. Cambridge University Press.

Pudovkin, M. and Semenov, V. (1985). Magnetic field reconnection theory and the solar wind-Magnetosphere interaction: A review. *Space Science Reviews*, 41(1):1–89.

Qiu, X. C. (2006). Eiscat observations of the diurnal variations in the f2-peak density above svalbard. Master's thesis, Universitetet i Oslo.

Raymund, T., Franke, S., Liu, C., Austen, J., and Klobuchar, J. (1990). Application of computerized tomography to the investigation of ionospheric structures. *Radio Science (ISSN 0048-6604)*, 25.

Raymund, T., Pryse, S., Kersley, L., and Heaton, J. (1993). Tomographic reconstruction of ionospheric electron density with European incoherent scatter radar verification. *Radio Science*, 28(5).

Richmond, A. and Kamide, Y. (1988). Mapping electrodynamic features of the high-latitude ionosphere from localized observations- Technique. *Journal of Geophysical Research*, 93(A6):5741–5759.

Rinne, Y. (2006). EISCAT Observations of Reversed Flow Events in the Cusp Ionosphere. Master's thesis, Universitetet i Oslo.

Rodger, A. (1998). Polar patches - outstanding issues. In *Polar Cap Boundary Phenomena*, pages 281–288. Kluwer Academic Publishers.

Rodger, A., Pinnock, M., and Dudeney, J. (1994a). A new mechanism for polar patch formation. *Journal of Geophysical Research*, 99(A4):6425–6436.

Rodger, A., Pinnock, M., Dudeney, J., Watermarn, J., de la Beaujardiere, O., and Baker, K. (1994b). Simultaneous two hemisphere observations of the presence of polar patches in the nightside ionosphere. *Ann. Geophysicae*, 12:642–648.

Ruohoniemi, J. and Baker, K. (1998). Large-scale imaging of high-latitude convection with super dual auroral radar network hf radar observations. *Journal of Geophysical Research*, 103(A9):20,797–20,811.

Ruohoniemi, J., Greenwald, R., Baker, K., Villain, J.-P., and McCready, M. (1987). Drift motions of small-scale irregularities in the high-latitude f region: An experimental comparison with plasma drift motions. *Journal of Geophysical Research*, 92:4553–4564.

Russel, C. and Elphic, R. (1978). Initial isee magnetometer results: magnetopause observations. *Space Sci. Rev.*, 22.

Russell, C. (1971). Geophysical coordinate transformations. *Cosmic Electrodynamics*, pages 184–196.

Russell, C. (2001). Solar wind and interplanetary magnetic field: A tutorial. *Geophysical Monograph-American Geophysical Union*.

Russell, C. and Elphic, R. (1979). ISEE observations of flux transfer events at the dayside magnetopause. *Geophysical Research Letters*, 6:33–36.

Sandholt, P., Farrugia, C., Moen, J., Noraberg, Ø., Lybekk, B., Sten, T., and Hansen, T. (1998). A classification of dayside auroral forms and activities as a function of interplanetary magnetic field orientation. *Journal of Geophysical Research-Space Physics*, 103(A10).

Sato, T. (1959). Morphology of ionospheric F2 disturbances in the polar regions. *Rep. Ionos. Space Res. JPN*, 13(91).

Schunk, R. and Sojka, J. (1996). Ionosphere-thermosphere space weather issues. *Journal of Atmospheric and Terrestrial Physics*, 58(14):1527–1574.

Schunk, R., Zhu, L., and Sojka, J. (1994). Ionospheric response to traveling convection twin vortices. *Geophysical Research Letters*, 21(17).

Shepherd, S. and Ruohoniemi, J. (2000). Electrostatic potential patterns in the high-latitude ionosphere constrained by superdarn measurements. *Journal of Geophysical Research*, 105(A10).

Shue, J.-H., Song, P., Russel, C., Steinberg, J., Chaoa, J., Zastenke, G., Vaisberg, O., Kokubun, S., Singer, H., Detman, T., and Kawano, H. (1998). Magnetopause location under extreme solar wind conditions. *Journal of Geophysical Research*, 103(A8):17,691–17,700.

Siscoe, G., Lotko, W., and Sonnerup, B. (1991). A high-latitude, low-latitude boundary layer model of the convection current system. *Journal of Geophysical Research*, 96(A3):3487–3495.

Smith, C., L'Heureux, J., Ness, N., Acuña, M., Burlaga, L., and Scheifele, J. (1998). The ace magnetic field experiment. *Space Science Reviews*, pages 613–632.

Smith, E. (2001). The heliospheric current sheet. *Journal of Geophysical Research*, 106(A8):15,819–15,831.

Sojka, J., Bowline, M., and Schunck, R. (1994). Patches in the polar cap ionosphere: Ut and seasonal dependence. *Journal of Geophysical Research*, 99.

Sojka, J., Bowline, M., Schunck, R., Decker, D., Valladares, C., Sheehan, R., Anderson, D., and Heelis, R. (1993). Modeling polar cap f region patches using time varying convection. *Geophysical research letters*, 20(1783-1786).

Stone, E., Frandsen, A., Mewaldt, R., Christian, E., Margolies, D., JF, O., and Snow, F. (1998). The advanced composition explorer. *Space Science Reviews*.

Thomson, J. (1906). *Conduction of electricity through gases*. University press.

Valladares, C., Basu, S., Buchau, J., and Friis-Christensen, E. (1994). Experimental evidence for the formation and entry of patches into the polar cap. *Radio Science*, 29.

Valladares, C., Decker, D., Sheehan, R., and Anderson, D. (1996). Modeling the formation of polar cap patches using large plasma flows. *Radio Science*, 31(3):573–593.

Valladares, C., Decker, D., Sheehan, R., Anderson, D., Bullett, T., and Reinisch, B. (1998). Formation of polar cap patches associated with north-to-south transitions of the interplanetary magnetic field. *Journal of Geophysical Research*, 103(A7):14,657–14,670.

Walker, I., Moen, J., Kersley, L., and Lorentzen, D. (1999). On the possible role of cusp/cleft precipitation in the formation of polar-cap patches. In *Annales Geophysicae*, volume 17, pages 1298–1305. Springer.

Walker, I., Moen, J., Mitchell, C., Kersley, L., and Sandholt, P. (1998). Ionospheric effects of magnetopause reconnection observed using ionospheric tomography. *Geophysical Research Letters*, 25(3).

Wannberg, G., Wolf, I., Vanhainen, L.-G., Koskenniemi, K., Röttger, J., Postila, M., Markkanen, J., Jacobsen, R., Stenberg, A., Larsen, R., Eliassen, S., Heck, S., and Huuskonen, A. (1997). The elscat svalbard radar: A case study in modern incoherent scatter radar system design. *Radio Science*, 32(6).

Watermann, J., Lummerzheim, D., de La Beaujardiere, O., Newell, P., and Rich, F. (1994). Ionospheric footprint of magnetosheathlike particle precipitation observed by an incoherent scatter radar. *Journal of Geophysical Research-Space Physics*, 99(A3).

Weber, E., Buchau, J., Moore, J., Sharber, J., and Livingston, R. (1984). F-layer ionization patches in the polar cap. *Environmental research papers*.

Weimer, D. (1999). Substorm influence on the ionospheric electric potentials and currents. *Journal of geophysical research*, 104(A1):185–197.

Wickwar, V. and Kofman, W. (1984). Dayside red auroras at very high latitudes: the importance of thermal excitation. *Geophysical research letters*, 11(9):923–926.

Winningham, J. and Heikkila, W. (1974). Polar cap auroral electron fluxes observed with ISIS 1. *J. Geophys. Res*, 79(7).

Yeh, H., Foster, J., Rich, F., and Swider, W. (1991). Storm time electric field penetration observed at mid-latitude. *Journal of Geophysical Research-Space Physics*, 96(A4).